Direct Frequency Comb Spectroscopy for Optical Frequency Metrology and Coherent Interactions

by

Adela Marian

B.A., University of Bucharest, 1998

A thesis submitted to the
Faculty of the Graduate School of the
University of Colorado in partial fulfillment
of the requirements for the degree of
Doctor of Philosophy
Department of Physics
2005

This thesis entitled:
Direct Frequency Comb Spectroscopy for Optical Frequency Metrology and Coherent Interactions
written by Adela Marian
has been approved for the Department of Physics

Dr. Jun Ye

Dr. John L. Hall

Date

The final copy of this thesis has been examined by the signatories, and we find that both the content and the form meet acceptable presentation standards of scholarly work in the above mentioned discipline.

Marian, Adela (Ph.D., Physics)

Direct Frequency Comb Spectroscopy for Optical Frequency Metrology and Coherent Interactions

Thesis directed by Dr. Jun Ye

We take advantage of a phase-stable, wide-bandwidth femtosecond laser to bridge the fields of high-resolution spectroscopy and ultrafast science. This approach, which we call Direct Frequency Comb Spectroscopy (DFCS), involves using light from a comb of appropriate structure to directly interrogate atomic levels and to study time-dependent quantum coherence. In fact, DFCS may be effectively applied to determine absolute frequencies for atomic transitions anywhere within the comb bandwidth, obviating the need for broadly tunable and absolutely referenced continuous-wave (cw) lasers.

In this work, we apply DFCS to determine absolute atomic transition frequencies for one- and two-photon processes in laser-cooled ^{87}Rb atoms. In addition, DFCS enables studies of coherent pulse accumulation and multipulse interference, permitted by the relatively long-lived excited states. These effects are well modeled by our density matrix theory describing the interaction of the femtosecond comb with the cold atoms.

As in the case of precision spectroscopy performed with cw lasers, the use of the femtosecond comb as a probe requires a careful understanding of all systematic effects. We isolate and then mitigate the effects of the dominant sources of systematic errors, which include the mechanical effect of the optical comb on the atomic motion, Stark shifts by the probe laser, and Zeeman frequency shifts. The absolute frequency measurement results are comparable to the highest resolution measurements made with cw lasers. In addition, by determining the previously unmeasured absolute frequency of the 5S-7S two-photon transitions in ^{87}Rb, we show that prior knowledge of atomic transition frequencies is not essential for DFCS.

Dedication

To my family.

Acknowledgements

I would like to offer my gratitude to the people who have made my time here at JILA profitable and interesting. There are many people who have helped along the way and I hope I have included all of them below.

Special thanks are due to my advisor Jun Ye who gave me the opportunity to work on a very new and challenging experiment. Under his guidance I have learned about cold Rb, laser stabilization, mode-locked lasers and integrating cutting edge techniques to probe new physics.

I would especially like to thank the people who worked closely with me on the Rb project within the last two years: Matt Stowe, John Lawall and Daniel Felinto. This thesis would not have been possible but for their help. I have gained a lot from our numerous discussions, particularly during John's three-month visit. In the early stages of the experiment, I benefited from the involvement and helpful suggestions of Xinye Xu, Tai Hyun Yoon and Long-Sheng Ma.

My experience here has been made more interesting and fun by the people who were working on various other experiments in the lab and with me at times, in particular Joe Berry, Kevin Holman, Seth Foreman, Jason Jones, Tara Fortier, Mark Notcutt and David Jones. I also enjoyed interacting with and learning interesting things from members of the fs stabilization group, Kevin Moll, Darren Hudson and Mike Thorpe, the cold strontium group, Tom Loftus, Andrew Ludlow, Marty Boyd and Tetsuya Ido, and the cold molecule group, Eric Hudson and Heather Lewandowski.

Thanks are also due to the support staff at JILA, their help over the years was invaluable. Terry Brown and James Fung-A-Fat deserve double-thanks for the patience they showed in guiding me through the art of electronics, while Alan Pattee and Hans Green have always been very helpful in the machine shop.

I wish to thank all of my committee members, Chris Greene, Jan Hall, David Jonas, Henry Kapteyn and Jun Ye, for their comments. I especially thank Jan for all of his suggestions and kind encouragement. I greatly appreciate Qudsia Quraishi's help in proofreading the final copy of this thesis, as well.

Much thanks to my dear friends Susan Duncan, Peter Schwindt, Anne Curtis, Phil Kiefer and Malcolm Rickard for making my stay in Boulder both enjoyable and entertaining.

Finally, I wish to thank my family. My parents, my two sisters and Mike were always there for me; I thank them for their constant support, love and patience.

Contents

Chapter

Tables

Table

Figures

Figure

Chapter 1

Introduction

1.1 Overview

The recent introduction [1,2] of phase-stabilized, wide-bandwidth frequency combs based on mode-locked femtosecond (fs) lasers has provided optical frequency markers that may be directly linked to optical or microwave standards. Many laboratories have since constructed frequency combs for a variety of exciting applications. These include: measurements of absolute optical frequencies and precision laser spectroscopy [3], development of optical atomic clocks [4, 5], optical frequency synthesis [6] and broadband, phase-coherent spectral generation [7, 8], along with coherent synthesis of optical pulses [9], phase-sensitive extreme nonlinear optics [10] and pulse timing stabilization.

Ultrashort pulses may also be applied to study coherent evolution in atomic and molecular systems. In particular, coherent wave packet motion has been observed and even actively controlled [11]. In addition, current work involves the use of fs lasers to achieve quantum coherent control in semiconductors [12] and in studying the temporal dynamics of biological physics [13]. These studies may require pulses which are tailored to probe or indeed selectively drive the dynamical process. This necessitates precise control over the amplitude- and phase of the ultrashort pulses, otherwise known as optical pulse synthesis [14].

On the road to tailoring optical pulses, one powerful demonstration was the phase-coherence established between two independent femtosecond lasers. Coherent optical pulse synthesis from two fs lasers has been reported in 2001 [9], where light pulses were generated with durations shorter than those obtainable from the individual lasers. This leads to an extended coherent bandwidth to be used in ultrafast experiments.

Before the advent of phase-stabilization, research showed [15] that the longitudinal modes of a 73-fs Kerr-lens mode-locked Ti:S laser [16] are uniformly distributed in frequency space within an experimental resolution of better than 10^{-16} and that the mode spacing differs from the pulse repetition frequency by less than 10^{-15}. Thus, passively mode-locked Ti:S lasers can possess an inherent stability and that is one of their most powerful features.

On an apparently independent path, precise spectroscopic studies of atoms and molecules have always been performed with continuous wave (cw) lasers, refined over the years to be very narrow spectrally, in order to enable probing of very narrow features [17]. Precision atomic and molecular spectroscopy, enabled by the progress in cw laser stabilization, has been one of the most important fields of modern scientific research, providing the experimental underpinning of quantum mechanics and quantum electrodynamics (e.g. detailed investigations of atomic and molecular structure, determination of fundamental constants, realization of time, frequency and length standards, tests of special relativity, progress in optical communications etc.).

In the first experiments using mode-locked femtosecond lasers, they served only as rulers for studying atomic systems and did not directly interrogate the atoms. Hänsch and coworkers used the comb spectrum of a fs laser to span an optical interval of 50 nm, and improved the measurement accuracy of the D_1 resonance line in cesium by almost three orders of magnitude [18], providing a new value for the fine structure constant. To measure the D_1 line, its frequency was compared against the fourth harmonic of a CH_4-stabilized laser employed as the absolute frequency reference. The fs comb was used as a frequency ruler to measure the resulting frequency difference of 18.39 THz (this frequency interval contained roughly 244 000 comb lines). To uniquely determine the exact number of comb lines involved and therefore the unknown frequency, an optical cavity was employed to select every 20th mode, thus increasing the pulse repetition rate by a factor of 20.

Diddams and colleagues at JILA later bridged a frequency gap of 104 THz [19], yielding an improved frequency measurement of the 1064 nm Nd:YAG laser by using a 778-nm two-photon transition in ^{85}Rb as an absolute reference. In a following experiment, the output of the laser was spectrally broadened to an optical octave in a microstructure fiber, permitting a direct measurement of an iodine-stabilized Nd:YAG, and then measurements of 'known' frequencies within the laser spectrum, such as the well established transitions at 633 nm and 778 nm [20].

Phase-stabilization of mode-locked lasers was enabled by the implementation of self-referencing techniques [21] by means of highly nonlinear microstructure fibers [22]. A self-referencing technique, that will be discussed in Chapter 3, was first demonstrated at JILA by Jones and coworkers [1]. They also made absolute frequency measurements using a phase-stabilized frequency comb referenced to the primary Cs standard. The stabilized frequency combs, providing a dense grid of reference frequencies that span substantial parts of the visible to near-infrared, have rapidly become extremely powerful tools for optical frequency metrology, opening the door to a new exciting era of remarkable progress. This is because atomic and molecular structural information can now be probed over a broad spectral range, with vastly improved measurement precision and accuracy enabled by this absolute frequency-based approach.

To date, however, these applications of fs lasers in frequency metrology used the frequency comb only as a reference ruler, while still employing the traditional cw laser-based spectroscopic approaches [23].

1.2 What about using the femtosecond comb directly for spectroscopy?

The main problem with using a pulsed laser for spectroscopy is the broad frequency bandwidth associated with a short pulse. The broad spectrum prevents high-precision measurements of state energies. This problem can be avoided by using a train of phase-coherent pulses, which permits frequency resolution orders of magnitude better than that associated with a single pulse.

T. Hänsch first introduced the idea of using coherent pulse trains from mode-locked lasers for the measurement of optical frequency intervals and high-resolution spectroscopy in 1976 [24]. A stable train of pulses forms a regular and discrete set of modes separated by the pulse repetition rate in the frequency domain. Hänsch showed that a sequence of pulses results in signal enhancement over single-pulse excitation for the atomic transition amplitude. In particular, he pointed out the resonant excitation probability is proportional to the squared number of pulses arriving within the atomic lifetime (for small incident light intensities).

The spectroscopic applications of this multi-pulse interference were experimentally demonstrated within the following two years. First, a train of phase-coherent pulses produced externally to the laser, by multiple reflections of a single pulse injected into an optical resonator, was utilized for Doppler-free two-photon excitation in Na [25]. Then, in 1978, the comb of a mode-locked picosecond dye laser [26] was used to measure the Na 4d fine-structure splitting, i.e. frequency intervals of $\sim$ 1 GHz, via Doppler-free two-photon spectroscopy [27]. In this experiment, the axial mode separation was actively controlled in the frequency domain (equivalent to stabilizing the repetition frequency of a train of pulses). As the laser spectrum is scanned, resonant excitation occurs whenever the sum of two frequencies is equal to the two-photon transition frequency. The comb of lines was used as a ruler in frequency space to measure optical frequency differences.

The limitation of this technique was the small bandwidth of the available mode-locked dye lasers, preventing measurements of large optical frequency differences.

The powerful combination of cw stabilization, passively mode-locked lasers and microstructure fibers, culminating with the phase-stabilization of femtosecond lasers, has made it possible to meet some of the conditions necessary to probe atomic structure directly with a frequency comb for precise frequency measurements: (i) short pulses, i.e. wide bandwidth (ii) pulse-to-pulse coherence and (iii) absolute referencing of the frequency comb.

Many new technologies have been enabled by the phase-stabilization of femtosecond lasers. In order to be able to phase-stabilize a femtosecond laser, one needs to understand its pulse characteristics. The connection between the short pulses emitted from the laser and the powerful frequency comb generated is described in the following section.

1.3 Time- and frequency-domain description of mode-locked lasers

The output of a mode-locked laser is a very regular train of ultrashort pulses, with the interval between pulses τ usually ~ 6 orders of magnitude higher than the pulse duration. These short pulses are produced when a fixed phase relationship is established among all the lasing longitudinal modes of the laser cavity (i.e. mode-locking), resulting in their coherent addition and the formation of a light pulse. An isolated light pulse can be represented as a sinusoidal optical carrier of angular frequency ω_c, amplitude-modulated by an envelope function $\mathcal{E}(t)$, with the electric field thus given by $E(t) = \mathcal{E}(t)\, exp\left[\, i\,(\omega_c\, t + \phi_0)\right]$. When traveling through a medium, the carrier propagates at the phase velocity, while the envelope advances at the group velocity. In general, the two velocities are different for a dispersive medium: $v_p = c\,/n$ and $v_g = c\,/\left(n + \omega\frac{\partial n}{\partial \omega}\right)$. For instance, traversing a distance l in a dispersive material gives a phase shift of $\omega_c\left(\frac{l}{v_g} - \frac{l}{v_p}\right) = \frac{l\,\omega_c{}^2}{c}\frac{\partial n}{\partial \omega} = -2\pi\, l\frac{\partial n}{\partial \lambda}$. This difference in the phase and group velocities inside the laser cavity causes the phase between the optical carrier and the peak of the envelope to evolve between successive pulses in the train. Let $\delta\phi$ denote the amount by which the carrier-envelope phase changes from pulse to pulse. After including this pulse-to-pulse phase-shift, the electric field of a train of pulses for a fixed spatial coordinate is

$$E(t) = \sum_n \mathcal{E}_n(t - n\tau)\, exp\, [\, i\, (\omega_c\, t + \phi_0 - n\, \omega_c\, \tau + n\, \delta\phi)]. \tag{1.1}$$

By taking its Fourier Transform [28] we obtain the following expression for the angular frequencies

$$\omega_N = \frac{N\, 2\pi}{\tau} - \frac{\delta\phi}{\tau}. \tag{1.2}$$

Thus, the spectrum of the mode-locked femtosecond laser consists of a wide comb of discrete optical frequencies, offset from the exact harmonics of the repetition rate by a frequency proportional to the pulse-to-pulse carrier-envelope phase shift [Fig. 1.1]. The spectrum is described by the simple relation $\nu_N = N f_r + f_0$, where N is a large integer on the order of 10^6, $f_r = \frac{1}{\tau}$ is the pulse repetition rate and $f_0 = -\frac{1}{2\pi}\, \delta\phi\, f_r$ is the carrier-envelope offset frequency. Note that the relevant quantity here is $\delta\phi$ modulo 2π, i.e. f_0 is bounded by f_r.

The two laser parameters are dynamic quantities, sensitive to environmental perturbations affecting the laser cavity. Not surprisingly, there are no locking mechanisms between the pulse envelope and the optical carrier inside an unstabilized laser, so their relative phase $\delta\phi$ experiences fluctuations between successive pulses. Consequently, for spectroscopic studies with a femtosecond laser, both comb parameters f_r and f_0 need to be actively stabilized.

As a reminder, absolute optical frequency measurements are made with respect to the ground state hyperfine splitting in ^{133}Cs at 9.192631770 GHz, which provides the current definition for the second. This leap from the optical to the radio-frequency domain has been a daunting task in frequency metrology for the last 30 years, before

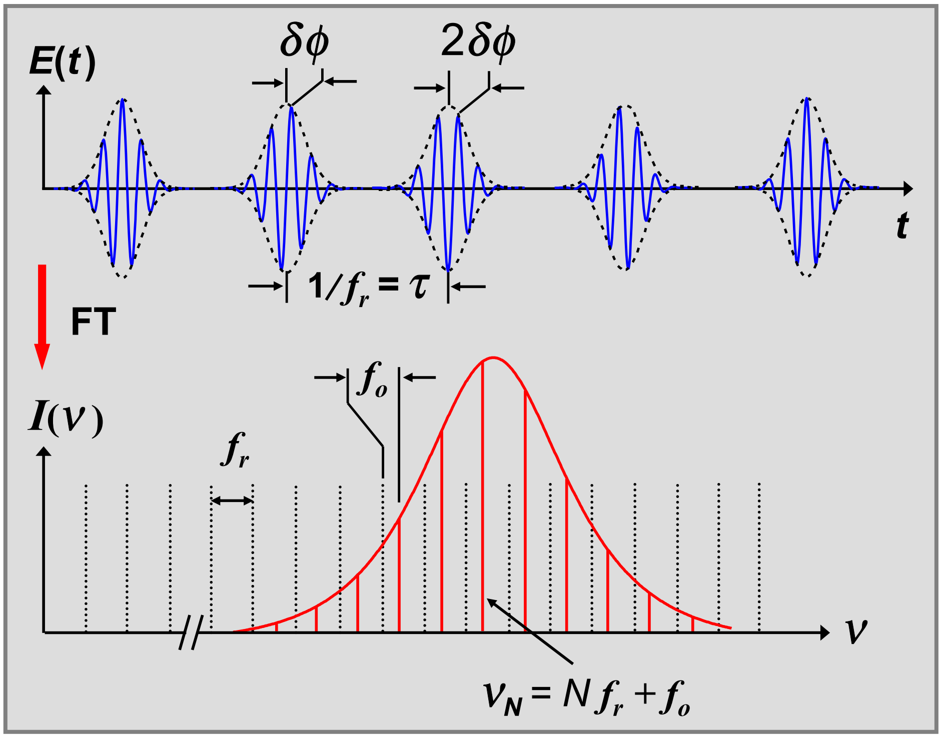

Figure 1.1: Correspondence between the time and frequency domains for a Ti:S mode-locked laser. In the time domain, the carrier-envelope phase changes at a defined rate between successive pulses in the train. In the frequency domain, the comb lines are spaced by the laser repetition rate f_r and the comb is shifted from integer multiples of f_r by an offset frequency f_0. The Ti:S laser used in the experiment is centered at 778 nm and has a FWHM bandwidth of $\sim$ 55 nm.

the introduction of the mode-locked approach. Because of the complexity involved, only a few harmonic frequency chains were ever implemented, for very specific optical frequency measurements. A few examples are: the 88 THz transition in CH_4 [29] (which led to the speed of light measurement [30]), the I_2-stabilized He-Ne transition at 473 THz [31], the 455 THz intercombination transition in ^{40}Ca [32], the $5s\ ^2S_{1/2} \rightarrow 4d\ ^2D_{5/2}$ transition at 445 THz in $^{88}Sr^+$ [33], the 2S-12D transitions in hydrogen and deuterium at 799 THz [34]. Stabilized frequency combs allow one to phase-coherently link any unknown optical frequency within the comb spectrum directly to a primary microwave standard.

1.4 Direct Frequency Comb Spectroscopy

Following our own theoretical studies [35], we take advantage of the phase-stable, wide-bandwidth femtosecond pulse train to bridge the fields of high-resolution spectroscopy and ultrafast science, in a spectroscopic study of laser-cooled ^{87}Rb atoms. This approach, which we call Direct Frequency Comb Spectroscopy (DFCS), involves using light from a comb of appropriate structure to directly interrogate atomic levels and to study time-dependent quantum coherence.

By utilizing a stabilized fs comb, multiple atomic states may be simultaneously and directly excited, by tuning the appropriate comb lines into resonance, and the subsequent dynamics may be probed. Furthermore, given that the comb has two independent degrees of freedom, it is always possible to simultaneously satisfy two-photon as well as one-photon resonance conditions.

In fact, DFCS may be applied to determine absolute frequencies for atomic transitions anywhere within the comb bandwidth. The entire transition spectrum can be efficiently retrieved by a quick scan of the laser repetition frequency. This obviates the need for a broadly tunable and absolutely referenced cw laser and is especially useful in the study of multi-photon processes where several laser sources may be required. Thus, optical frequency combs are a highly efficient tool for precise studies of atomic structure.

In this work, we apply DFCS to determine absolute atomic transition frequencies for one- and two-photon processes, as illustrated in Fig. 1.2. DFCS enables studies of coherent pulse accumulation and multipulse interference, permitted by the relatively long-lived 5D and 7S states. The observed coherent pulse accumulation and interference effects are well modeled by our density matrix theory describing the interaction of the femtosecond comb with the atoms, as discussed in Chapter 2. We use the theory results to construct transition spectra to compare against the experimental spectra.

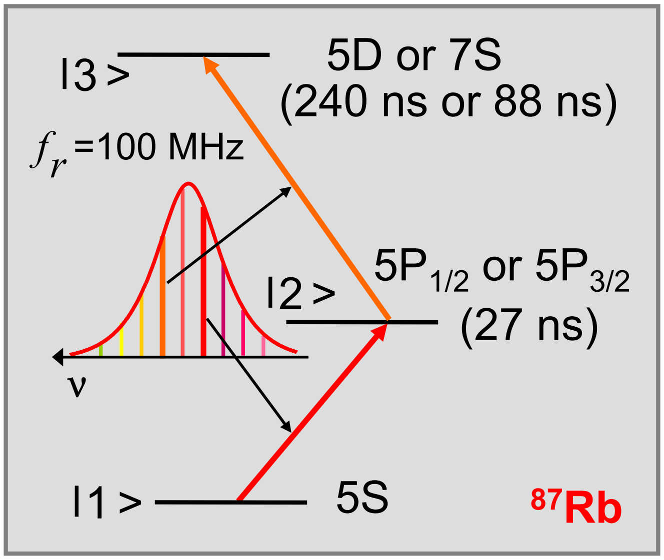

Figure 1.2: Schematic of the ^{87}Rb energy levels participating in the 5S-5D and 5S-7S two-photon transitions and 5S-5P one-photon transitions. These are the relevant levels probed using direct frequency comb spectroscopy (DFCS).

We present the details of the implementation of the femtosecond stabilization scheme and the MOT setup in Chapter 3. These are integrated together for spectroscopic studies in Chapter 4.

As in the case of precision spectroscopy performed with cw lasers, the use of the femtosecond comb as a precision probe requires a careful understanding of all systematic effects. We find that the dominant effects are the mechanical effect of the optical comb on the atomic motion, the light shift by the probe laser, and the Zeeman frequency shifts. In Chapter 4, we address the mechanical action of the probe laser by using a counterpropagating beam configuration. We observe Stark shifts generated by detunings from the intermediate states in the two-photon processes and we reduce their effect by always probing on resonance with the intermediate state of interest.

We first study the 5S-5D two-photon transitions in ^{87}Rb, leading to high-resolution spectroscopy for some of the transitions, as presented in Chapter 5. The measurement results are comparable to the highest resolution measurements made with cw lasers. By determining the previously unmeasured absolute frequency of the 5S-7S two-photon transitions in ^{87}Rb, we show that prior knowledge of atomic transition frequencies is not essential for this technique to work, and indicate that it can be applied in a broad context. When resonant enhancement is enabled by a comb component tuned near an intermediate 5P state, we observe two-photon transitions occurring between initial and final states that differ by one unit of the total angular momentum ($\Delta F = \pm 1$), which are absent for far-detuned intermediate states. This capability of accessing adjacent excited hyperfine levels from the same ground state allows for direct measurements of hyperfine splittings.

We then use DFCS to measure one-photon transitions, and choose the 5S-5P transitions as an example, as detailed in Chapter 6. The measurement of 5P states is also carried out indirectly via the 5S-5D two-photon transitions, by studying their resonant enhancement when comb components are scanned through the intermediate 5P states. We compare the 5P measurements obtained via one-photon and two-photon DFCS and clearly demonstrate the importance of population transfer in working with multilevel systems probed by multiple comb components. Incoherent processes such as optical pumping govern the population dynamics beyond the atomic decoherence time.

For the case of the indirect 5P frequency measurements via the 5S-5D two-photon transitions, the experimental data do not yield directly the lineshape. In this case, we use the theory prediction to adjust the raw data and retrieve a Lorentzian lineshape, as described in Chapter 6.

The optical coherence of a phase-stabilized pulse train provides a spectral resolving power approaching that of state-of-the-art cw lasers. At the same time, the narrow linewidth of individual comb lines permits a precise and efficient determination of the global energy-level structure, providing a direct connection among the optical, terahertz, and radio-frequency domains.

Chapter 2

Density-matrix method for coherent accumulation in a multi-level atom

We will now study coherent accumulation in a multi-level atom interacting with a train of ultrashort pulses. For the situation where the atomic relaxation times are longer than the interpulse interval τ, the atomic coherence will survive between two consecutive pulses, leading to *coherent accumulation of excitation* in the sample. Constructive/destructive interference among the coherences excited by the train of pulses will determine the final atomic populations. We will focus on the accumulative effects occurring in the sequential 5S-5P-5D two-photon transitions.

The interaction of the femtosecond comb with the atoms is modeled starting with the Liouville equation for the density matrix of all the atomic states in the laser bandwidth accessible through two-photon absorption, with radiative relaxation included via phenomenological decay terms. The density matrix equations are solved to a fourth-order perturbative expansion in the electric field. With the approximation of impulsive optical excitation during the pulse, followed by free evolution and decay, an iterative numerical procedure is used to determine the state of the atomic system after an arbitrary number of pulses.

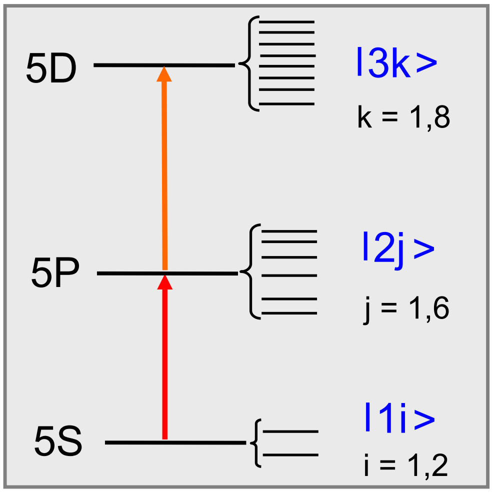

Figure 2.1: Cascade configuration for a multi-level atom.

2.1 Modeling coherent interactions

Consider an electric field $E(t)$ interacting with a multi-level atom in which all the levels are distributed in three different manifolds $|1i\rangle$, $|2j\rangle$ and $|3k\rangle$, in a cascade configuration, as presented in Fig. 2.1. Here '1' labels the ground 5S states, '2' the intermediate 5P states and '3' the excited 5D states, while i, j and k stand for the various fine and hyperfine levels of a specific state. We adopted this simplified notation for the energy levels only in the theory chapter, because it will make the following equations easier to follow.

The Hamiltonian of the system $\widehat{H}$ is given by the sum of the field-free atomic Hamiltonian $\widehat{H}_0$ and the interaction potential between the atom and the electric field in the electric-dipole approximation $\widehat{H}_{int}$. Thus, $\widehat{H} = \widehat{H}_0 + \widehat{H}_{int}$, with

$$\begin{aligned} \widehat{H}_0 &= \sum_i E_{1i}|1i\rangle\langle 1i| + \sum_j E_{2j}|2j\rangle\langle 2j| + \sum_k E_{3k}|3k\rangle\langle 3k| \qquad \text{and} \\ \widehat{H}_{int} &= -\sum_{i,j} \mu_{1i,2j}\, E(t)|1i\rangle\langle 2j| + \sum_{j,k} \mu_{2j,3k}\, E(t)|2j\rangle\langle 3k| + h.c., \end{aligned} \tag{2.1}$$

where E_{1i}, E_{2j}, E_{3k} are the energies of levels $|1i\rangle$, $|2j\rangle$ and $|3k\rangle$, respectively, and $\mu_{i,j}$ is the dipole moment of the i → j transition.

We are interested in the time evolution of the state of the system after a long sequence of pulses. This temporal evolution is described by the Bloch equations, derived from the Liouville equations upon inclusion of the relaxation terms. The starting point is therefore the Liouville equation for the density-matrix elements of the multi-level atomic system, resulting in 9 families of equations for the ground-, intermediate- and excited-state populations, the intra-ground-, intra-intermediate- and intra-excited-state coherences, as well as the 1-2, 2-3 and 1-3 coherences. For clarity, I will write out some representative Liouville equations, for the ground-state populations, ground-state coherences and the 1-2 coherences, respectively:

$$\begin{aligned}
\frac{\partial \rho_{1i,1i}}{\partial t} &= -\frac{i}{\hbar}\langle 1i|[\widehat{H},\widehat{\rho}]|1i\rangle \quad \text{ground-state population} \\
\frac{\partial \rho_{1i,1s}}{\partial t} &= -\frac{i}{\hbar}\langle 1i|[\widehat{H},\widehat{\rho}]|1s\rangle, \quad \mathbf{s} \neq \mathbf{i} \quad \text{intra-ground-state coherence} \\
\frac{\partial \rho_{1i,2j}}{\partial t} &= -\frac{i}{\hbar}\langle 1i|[\widehat{H},\widehat{\rho}]|2j\rangle \quad \text{1-2 coherence.}
\end{aligned} \tag{2.2}$$

The 6 remaining families can be written in a similar manner.

The Bloch equations are obtained from the Liouville equations after including the relaxation rates $\Gamma_{i,j}$ of the (i,j) density matrix components. Note that for our case, $\Gamma_{1i,1i} = 0$, all the population decay rates for a given state are equal, i.e. $\Gamma_{2j,2j} = \Gamma_{5P} \equiv \Gamma_2$ and $\Gamma_{3k,3k} = \Gamma_{5D} \equiv \Gamma_3$, and $\Gamma_{i,j} = \frac{1}{2}(\Gamma_{i,i} + \Gamma_{j,j})$. The subscripts indicating the states in the Γ coefficients will all be kept in the following derivation, for symmetry of the equations. As an example, I will write the Bloch equation for the 1-2 coherence:

$$\frac{\partial \rho_{1i,2j}}{\partial t} = -i\omega_{1i,2j}\,\rho_{1i,2j} - \frac{i}{\hbar}\langle 1i|[\widehat{H}_{int},\widehat{\rho}]|2j\rangle - \Gamma_{1i,2j}\,\rho_{1i,2j} \tag{2.3}$$

This was obtained by substituting the expression for the Hamiltonian $\widehat{H}$ in Eq. 2.2, with $\omega_{i,j} \equiv (E_i - E_j)/\hbar$. All the coherence equations look the same as Eq. 2.3, with only the appropriate change of indices.

Before writing expressions for the populations of levels $|1\rangle$ and $|2\rangle$, we must also consider the incoherent feeding of level $|2\rangle$ by level $|3\rangle$ and $|1\rangle$ by $|2\rangle$ present in a multi-level atomic system. Including these additional terms gives the populations as

$$\begin{aligned}
\frac{\partial\rho_{1i,1i}}{\partial t} &= -\frac{i}{\hbar}\langle 1i|[\widehat{H}_{int},\widehat{\rho}]|1i\rangle - \Gamma_{1i,1i}\,\rho_{1i,1i} + \sum_r \gamma_{1i,r}\,\rho_{r,r} \qquad (2.4)\\
\frac{\partial\rho_{2j,2j}}{\partial t} &= -\frac{i}{\hbar}\langle 2j|[\widehat{H}_{int},\widehat{\rho}]|2j\rangle - \Gamma_{2j,2j}\,\rho_{2j,2j} + \sum_r \gamma_{2j,r}\,\rho_{r,r}\\
\frac{\partial\rho_{3k,3k}}{\partial t} &= -\frac{i}{\hbar}\langle 3k|[\widehat{H}_{int},\widehat{\rho}]|3k\rangle - \Gamma_{3k,3k}\,\rho_{3k,3k}.
\end{aligned}$$

More details about deriving the incoherent feeding terms will be given in 2.1.2.

We can now integrate Eqs. 2.3 and 2.4, with the assumption of *impulsive optical excitation* during the interaction time: the pulse duration is ultrashort compared to the pulse repetition period or any relaxation time of the system, as seen from Table 2.1.

Pulse duration	$\sim$ 30 fs
Laser repetition period	10 ns
5P lifetime	27 ns [36]
5D lifetime	240 ns [36]
1-2 coherence lifetime	54 ns
1-3 coherence lifetime	480 ns
2-3 coherence lifetime	48.5 ns

Table 2.1: Relevant times for the interaction of the femtosecond laser with the ^{87}Rb atoms.

This means that the interaction potential $\widehat{H}_{int}$ changes on a very fast timescale compared to the $\Gamma_{i,j}$ relaxation rates, allowing us to neglect the temporal dependence on $\Gamma_{i,j}$ inside the integrals containing $\widehat{H}_{int}$, and yielding:

$$\begin{aligned}
\rho_{1i,1i}(t) &= e^{-\Gamma_{1i,1i}\,t}\left[\rho^0_{1i,1i} - \frac{i}{\hbar}\int_0^t dt'\langle 1i|[\widehat{H}_{int},\widehat{\rho}]|1i\rangle + \sum_r \gamma_{1i,r}\int_0^t dt' e^{\Gamma_{1i,1i}\,t'}\,\rho_{r,r}(t')\right]\\
\rho_{1i,2j}(t) &= e^{-i\omega_{1i,2j}\,t-\Gamma_{1i,2j}\,t}\left[\rho^0_{1i,2j} - \frac{i}{\hbar}\int_0^t dt' e^{i\omega_{1i,2j}\,t'}\langle 1i|[\widehat{H}_{int},\widehat{\rho}]|2j\rangle\right] \qquad (2.5)
\end{aligned}$$

for the ground-state population and 1-2 coherence, respectively.

Numerical integration of Eq. 2.5 gives the time evolution of the system with arbitrary initial conditions, but is computationally challenging for the ^{87}Rb atom, where there are ***two*** 5S initial levels, ***six*** 5P intermediate levels and ***eight*** 5D final levels, leading to a total of $16^2 = 256$ coupled Bloch equations. To avoid the long computational times, our collaborator Daniel Felinto [37,38] has developed an iterative numerical procedure that determines the state of the atomic system after any number of pulses. As previously mentioned, for laser repetition periods τ shorter than the relaxation times of the system, as is the case of ^{87}Rb, the atomic sample will accumulate excitation in the form of population and coherence.

In Daniel Felinto's iterative solution, the state of the system before the $(n+1)$-th pulse in the train is obtained from the state prior to the n-th pulse. The relation connecting ρ^{n+1} to ρ^n is easily derived from Eq. 2.5 by setting $t = \tau$. Again, making the *impulsive optical excitation* assumption means setting $t \to \infty$ in all the integrals containing $\widehat{H}_{int}$; the lower limit can be made $t \to -\infty$, since $E(t) = 0$ for $t < 0$. For the two sample elements of the density matrix appearing in Eq. 2.5 we obtain

$$\begin{aligned} \rho^{n+1}_{1i,1i} &= e^{-\Gamma_{1i,1i}\tau}\left[\rho^c_{1i,1i} + \sum_r \gamma_{1i,r}\int_0^\tau dt' e^{\Gamma_{1i,1i}t'}\,\rho_{r,r}(t')\right] \\ \rho^{n+1}_{1i,2j} &= e^{-i\omega_{1i,2j}\tau - \Gamma_{1i,2j}\tau}\left[\rho^c_{1i,2j}\right], \end{aligned} \tag{2.6}$$

where

$$\rho^c_{r,s} = \rho^n_{r,s} - \frac{i}{\hbar}\int_{-\infty}^{\infty} dt' e^{i\omega_{r,s}t'}\langle r|[\widehat{H}^n_{int}, \widehat{\rho}]|s\rangle \tag{2.7}$$

is the density matrix coherently excited by the n-th pulse ($\widehat{H}^n_{int}$), a function of the initial state prior to the n-th pulse ρ^n. Expressions similar to Eq. 2.6 are derived for the 7 remaining families of equations.

As a demonstration, Fig. 2.2 (adapted from Felinto *et al.*, reference [38]) shows the temporal evolution of the ρ_{22} and ρ_{33} populations in a *three-level* atom interacting with a train of hyperbolic-secant pulses. The total number of coupled Bloch equations for this system is $3^2 = 9$, so a direct numerical integration is not yet computationally intensive. The solid lines are a result of the direct numerical integration ($\sim$1.5 hours of computational time), while the open circles arise from successive applications of Eq. 2.6 to the atom initially in the ground state ($<$ 10 s). The transient behavior of the excited level populations is governed by their significantly different (factor of 10) lifetimes, as demonstrated by the different timescales in the two frames of the figure.

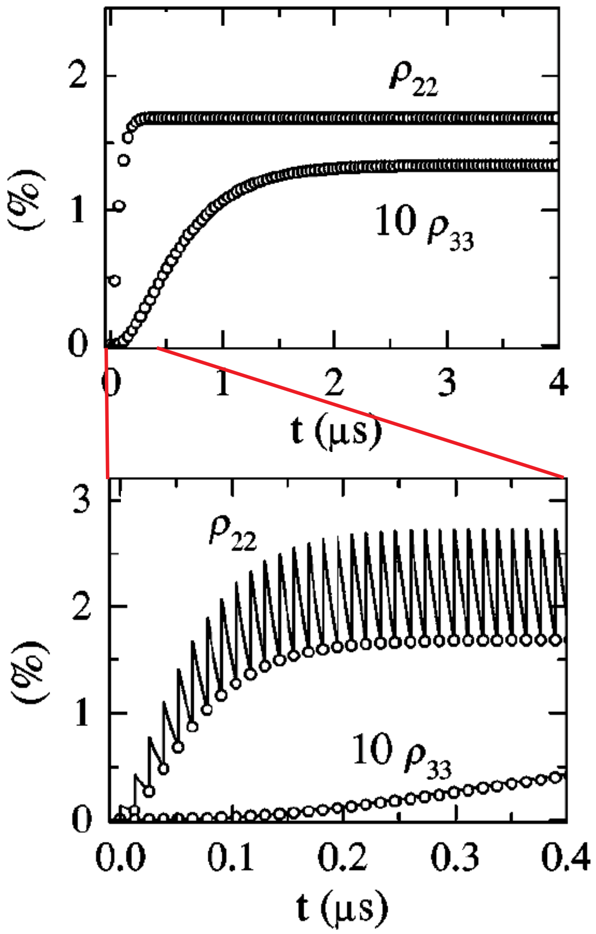

Figure 2.2: (adapted from reference [38]) Time evolution of the populations ρ_{22} and ρ_{33} for a *three-level* atom interacting with a train of hyperbolic-secant pulses. The two frames are different timescales of the same evolution, where the solid lines are a result of direct numerical integration of the Bloch equations and the open circles come from successive applications of Eq. 2.6.

After a large number of pulses, the system reaches a stationary state that repeats every τ. The shape of the direct-integration curve accounts for the very fast change in population during the pulse interaction time, followed by a slow decay in between pulses. The numerical-iteration method agrees well with the direct integration, in that it always matches the value at the minimum. This happens because, in the iteration procedure, the initial state is always taken to be the state ρ^n just before the impulsive excitation. The situation would be reversed and the two curves would match at the maximum if the initial state were the state immediately after each individual pulse.

To summarize, in the simplified treatment of coherent accumulation for a two-photon process in a multi-level atom, there are two major steps: the first is obtaining the state of the system after the interaction with a pulse in the train, for an arbitrary initial state of the atom (Eq. 2.6). The second step is the successive application of Eq. 2.6, yielding the atomic state after a sequence of pulses, or in other words, describing the time evolution of the system.

2.1.1 The coherently excited density matrix ρ^c

There are two quantities left to calculate now, the coherently excited density matrix in Eq. 2.7, associated with the impulsive excitation during the laser pulse, and the feeding terms in Eq. 2.4, arising from incoherent decay.

We will first focus on ρ^c, realizing that it is a product of two probability amplitudes in the interaction picture

$$\rho^c_{i,j} = C_i \times C_j^*, \quad C_i = \langle i|\widehat{U}_I(t)|\Psi_0\rangle, \tag{2.8}$$

with Ψ_0 the initial state of the system, which is a superposition of all the atomic states, and $\widehat{U}_I(t)$ the time propagation operator in the interaction picture, given by

$$\widehat{U}_I(t) = 1 + \left(-\frac{i}{\hbar}\right)\int_0^t dt'\widehat{H}^I_{int}(t') + \left(-\frac{i}{\hbar}\right)^2\int_0^t dt'\int_0^{t'} dt''\widehat{H}^I_{int}(t')\widehat{H}^I_{int}(t'') + \ldots \tag{2.9}$$

After inserting the relation for $\widehat{H}^I_{int}(t)$, $\widehat{H}^I_{int}(t) = e^{i\widehat{H}_0 t/\hbar}\,\widehat{H}_{int}(t)\,e^{-i\widehat{H}_0 t/\hbar}$, and specifying the electric field $E(t) = \mathcal{E}(t)e^{i\omega_c t + i\phi_0} + c.c.$ as defined in section 1.3, we obtain the following general expressions for the three groups of probability amplitudes:

$$C_{3k}(t) \;=\; \sum_s A_{3k,3s}C^0_{3s} + \sum_j A_{3k,2j}\,e^{-i\phi_0}C^0_{2j} + \sum_i A_{3k,1i}\,e^{-2i\phi_0}C^0_{1i} \tag{2.10}$$

$$\begin{aligned}
C_{2j}(t) &= \sum_k A_{2j,3k}\, e^{i\phi_0} C^0_{3k} + \sum_s A_{2k,2s} C^0_{2s} + \sum_i A_{2j,1i}\, e^{-i\phi_0} C^0_{1i} \\
C_{1i}(t) &= \sum_k A_{1i,3k}\, e^{2i\phi_0} C^0_{3k} + \sum_j A_{1i,2j}\, e^{i\phi_0} C^0_{2j} + \sum_s A_{1i,1s} C^0_{1i},
\end{aligned}$$

where $A_{i,j}$ are the Dyson coefficients corresponding to the time evolution from state i to state j. This yields the final formula for any element (i, j) of the impulsively excited density matrix ρ^c

$$\rho^c_{i,j} = e^{-iB_{i,j}\,\phi_0} \sum_{r,s} A_{i,r} A^*_{j,s}\, e^{iB_{r,s}\,\phi_0} \rho^0_{r,s}, \tag{2.11}$$

with $B_{i,j} = 2\sum_k(\delta_{3k,i} - \delta_{3k,j}) + \sum_k(\delta_{2k,i} - \delta_{2k,j})$, where the δ s are Kronecker symbols.

We are interested in developing a theory in *the weak-field regime*: from the infinite Dyson series only the terms up to the fourth order in the electric field will be kept. The fourth order is the smallest order contributing to population in the most excited level for two-photon transitions from the ground state. In this regime, making *the rotating-wave approximation* will result in expressions for the 9 groups of elements $A_{i,j}$ present in Eqs. 2.10 and 2.11. As an example, I will write out the expression for $A_{3k,3s}$:

$$\begin{aligned}
A_{3k,3s} &= \delta_{3k,3s} + \left(-\frac{iea_0}{\hbar}\right)^2 \sum_r m_{3k,2r} m_{2r,3s} \int_0^t dt' \int_0^{t'} dt'' e^{i\delta_{3k,2r}\,t'} e^{i\delta_{2r,3s}\,t''} \mathcal{E}^*(t')\mathcal{E}(t'') \\
&+ \left(-\frac{iea_0}{\hbar}\right)^4 \sum_{r,n,q} m_{3k,2r} m_{2r,1n} m_{1n,2q} m_{2q,3s} \int_0^t dt' \int_0^{t'} dt'' \int_0^{t''} dt''' \int_0^{t'''} dt'''' e^{i\delta_{3k,2r}\,t'} \\
&\times e^{i\delta_{2r,1n}\,t''} e^{i\delta_{1n,2q}\,t'''} e^{i\delta_{2q,3s}\,t''''} \mathcal{E}^*(t')\mathcal{E}^*(t'')\mathcal{E}(t''')\mathcal{E}(t'''') + \left(-\frac{iea_0}{\hbar}\right)^4 \\
&\times \sum_{r,n,q} m_{3k,2r} m_{2r,3n} m_{3n,2q} m_{2q,3s} \int_0^t dt' \int_0^{t'} dt'' \int_0^{t''} dt''' \int_0^{t'''} dt'''' e^{i\delta_{3k,2r}\,t'} e^{i\delta_{2r,3n}\,t''} \\
&\times e^{i\delta_{3n,2q}\,t'''} e^{i\delta_{2q,3s}\,t''''} \mathcal{E}^*(t')\mathcal{E}(t'')\mathcal{E}^*(t''')\mathcal{E}(t''''),
\end{aligned} \tag{2.12}$$

with $\delta_{i,j} \equiv \omega_{i,j} - \omega_c$ the detunings relative to the carrier frequency, $m_{i,j} = \mu_{i,j}/ea$ dimensionless dipole moments, e the electron charge and a the Bohr radius. The last three terms in Eq. 2.12 are second-order and fourth-order contributions to the excitation, related to the processes of absorption and stimulated emission on the lower and upper transitions. They are schematically drawn in Fig. 2.3.

This messy expression can be greatly simplified if we consider the situation where

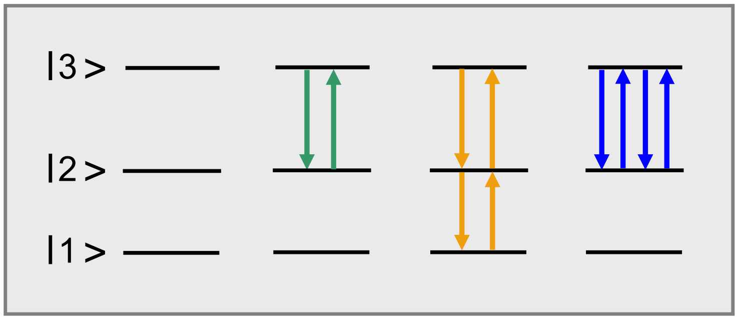

Figure 2.3: Vector diagrams for the four terms present in Eqs. 2.12 and 2.13 for the sample Dyson coefficient.

the pulse is ultrashort compared to the time variation determined by the atomic detunings, i.e. we neglect all the exponentials in Eq. 2.12, and if we limit ourselves to the reasonable case of a *real envelope function.* Under these approximations, the nested integrals take a much simpler form, via successive integration by parts, with the result

$$\begin{aligned} A_{3k,3s} &= \delta_{3k,3s} - \frac{\theta^{\,2}}{2!}\sum_{r} m_{3k,2r}m_{2r,3s} + \\ &+ \frac{\theta^{\,4}}{4!}\left(\sum_{r,n,q} m_{3k,2r}m_{2r,1n}m_{1n,2q}m_{2q,3s} + \sum_{r,n,q} m_{3k,2r}m_{2r,3n}m_{3n,2q}m_{2q,3s}\right). \end{aligned} \tag{2.13}$$

Here θ is the pulse area, defined as

$$\theta = \frac{ea}{\hbar}\int_{-\infty}^{\infty} dt\,\mathcal{E}(t) \quad \text{pulse area.} \tag{2.14}$$

2.1.2 The incoherent feeding terms

There are two very different timescales over which the populations present in the feeding-term integrals vary: first, there is a very fast change in population during the pulse interaction time, followed by a slow, incoherent decay during the interpulse interval. In this model, it is assumed for simplicity that level $|2\rangle$ is fed only by level $|3\rangle$, and $|1\rangle$ is only fed by $|2\rangle$. Note that the population in the latter level varies in time due to feeding from $|3\rangle$. However, in reality, there are two decay channels for the 5D population [36], as illustrated in Fig. 2.4: the first is the 5D-5P-5S radiative cascade and the second is the 5D-6P-5S cascade. In fact, we experimentally determine the 5D population by detecting the 420 nm blue fluorescence emitted in the 6P-5S transition. The 6P state is not included in the simulation.

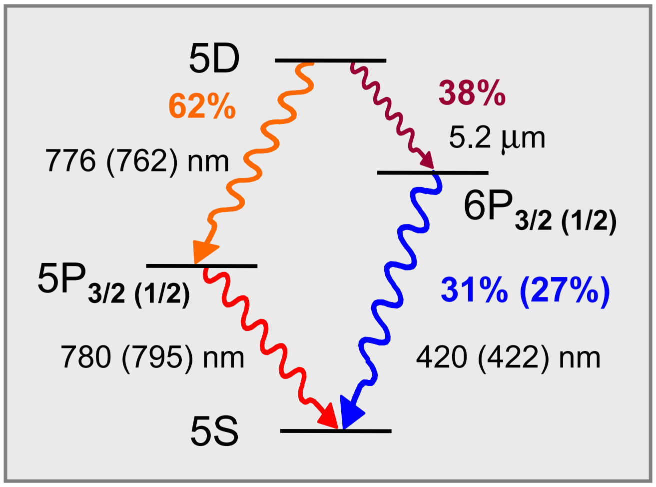

Figure 2.4: Decay paths for the 5D levels of ^{87}Rb, with the corresponding transition wavelengths and branching ratios specified. In the experiment, we detect the 6P-5S blue photons at 420 nm, which represent roughly 10% of the 5D population. The 6P levels also decay to the 6S and 4D levels, not pictured here.

For the situation where the pulse duration is ultrashort compared to the laser repetition period τ and considering only the 5P decay channel for the 5D population, we have:

$$\begin{aligned}\sum_k \gamma_{2j,3k} \int_0^\tau dt' e^{\Gamma_{2j,2j}\,t'} \rho_{3k,3k}(t') &\simeq \sum_k \gamma_{2j,3k}\, \rho^c_{3k,3k} \int_0^\tau dt' e^{\Gamma_{2j,2j}\,t'} e^{-\Gamma_{3k,3k}\,t'} \\ &= \sum_k \gamma_{2j,3k}\, \rho^c_{3k,3k} \frac{1 - e^{(\Gamma_{2j,2j}-\Gamma_{3k,3k})\tau}}{\Gamma_{3k,3k} - \Gamma_{2j,2j}}\end{aligned} \tag{2.15}$$

$$\begin{aligned}&\sum_j \gamma_{1i,2j} \int_0^\tau dt' e^{\Gamma_{1i,1i}\,t'} \rho_{2j,2j}(t') \simeq \sum_j \gamma_{1i,2j} \int_0^\tau dt' e^{\Gamma_{1i,1i}\,t'} e^{-\Gamma_{2j,2j}\,t'} \\ &\times \left[\rho^c_{2j,2j} + \sum_k \gamma_{2j,3k} \int_0^{t'} dt'' e^{\Gamma_{2j,2j}\,t''} \rho_{3k,3k}(t'') \right] \\ &= \sum_j \gamma_{1i,2j}\, \rho^c_{2j,2j} \frac{1 - e^{(\Gamma_{1i,1i}-\Gamma_{2j,2j})\tau}}{\Gamma_{2j,2j} - \Gamma_{1i,1i}} + \sum_j \sum_k \frac{\gamma_{1i,2j}\gamma_{2j,3k}}{\Gamma_{2j,2j} - \Gamma_{3k,3k}}\end{aligned}$$

$$\times\rho^c_{3k,3k}\left[\frac{1-e^{(\Gamma_{1i,1i}-\Gamma_{3k,3k})\tau}}{\Gamma_{3k,3k}-\Gamma_{1i,1i}}-\frac{1-e^{(\Gamma_{1i,1i}-\Gamma_{2j,2j})\tau}}{\Gamma_{2j,2j}-\Gamma_{1i,1i}}\right]. \tag{2.16}$$

After realizing that $\Gamma_{1i,1i}=0$ and that all the population decay rates for a given state are equal, i.e. $\Gamma_{2j,2j}=\Gamma_2$, $\Gamma_{3k,3k}=\Gamma_3$, after setting the feeding coefficients proportional to the branching ratios of the upper levels down to the lower levels $\gamma_{2j,3k}=r_{2j,3k}\Gamma_3$, $\gamma_{1i,2j}=r_{1i,2j}\Gamma_2$ and defining the following constants $D_{32}=\Gamma_3\frac{1-\exp(\Gamma_2-\Gamma_3)\tau}{\Gamma_3-\Gamma_2}$, $D_{21}=1-\exp(-\Gamma_2\tau)$ and $D_{321}=\frac{\Gamma_2\Gamma_3}{\Gamma_2-\Gamma_3}\left[\frac{1-\exp(-\Gamma_3\tau)}{\Gamma_3}-\frac{1-\exp(-\Gamma_2\tau)}{\Gamma_2}\right]$, the final expression for the populations after the n-th pulse becomes:

$$\begin{aligned}
\rho^{n+1}_{1i,1i} &= \rho^c_{1i,1i}+D_{21}\sum_j r_{1i,2j}\,\rho^c_{2j,2j}+D_{321}\sum_j r_{1i,2j}\sum_k r_{2j,3k}\,\rho^c_{3k,3k}\\
\rho^{n+1}_{2j,2j} &= e^{-\Gamma_2\tau}\left[\rho^c_{2j,2j}+D_{32}\sum_k r_{2j,3k}\,\rho^c_{3k,3k}\right]\\
\rho^{n+1}_{3k,3k} &= e^{-\Gamma_3\tau}\rho^c_{3k,3k},
\end{aligned} \tag{2.17}$$

where $\rho^c_{i,j}$ are given by Eq. 2.11.

2.2 Summary of the coherent interaction model

The relevant laser parameters for describing the interaction of the femtosecond comb with the atoms are the interpulse period τ, the carrier envelope phase evolution between successive pulses $\delta\phi$, the pulse duration and its associated area θ. The model includes the fine and hyperfine structure of the 5S, 5P and 5D states, with energy-level information provided by the literature. The Zeeman substructure is averaged over, for linear polarization. In the simulation, calculated oscillator strengths and Clebsch-Gordan coefficients are employed for all the involved transition pathways in an effort to accurately predict the relative signal strengths. This general set of coupled Bloch-type equations, evolving from one pulse to the next, leads to a global picture of coherent population accumulation and incoherent optical pumping.

For times that are short compared to the atomic decoherence time, the femtosecond pulse train drives the atomic coherence in phase such that a multi-pulse excitation is coherently built up for resonant atomic states. At longer times, however, the coherence in the optical field can no longer be transferred to the atom owing to the finite atomic coherence time. Incoherent processes such as optical pumping then govern the population transfer dynamics.

These two timescales of the system, excitation and optical pumping, can be clearly seen in Fig. 2.5 (a) which shows the time evolution for two different two-photon resonances. The two curves have the same coherent excitation timescale of a few microseconds, set by the 5S-5D coherence lifetime of $\sim$ 500 ns. The slow decay rate is different though for each transition. Figure 2.5 (b) illustrates the behavior of one of the transitions as a function of the detuning from resonance. On resonance, all the pulses in the train contribute to the excitation, since the train of pulses is in phase with the atomic frequency. Away from resonance, the decrease in population due to destructive interference is accompanied by oscillations in the excitation region, arising from the phase difference between the atomic frequency and the frequency of the closest comb line. This oscillatory behavior at the frequency difference is more obvious in Fig. 2.5 (c), where the detuning from resonance is even larger.

2.3 Coherent accumulation enables high resolution

Temporal coherent control is best manifested in the 5D coherent population accumulation and transition linewidth evolution, which reach their asymptotic limits imposed by the atomic decoherence, through the coherent interaction with the train of femtosecond pulses . The results of the model (Fig. 2.6), under the condition of a small pulse area, illustrate the effect of pulse accumulation on signal strength and spectral linewidth.

The upper graph [(Fig. 2.6 (a)] shows that the on-resonance 5D population increases as the square of the number of pulses until reaching approximately the decoherence time, $\sim$ 500 ns for the 5D states. This 5D signal scaling at short times is reinforced

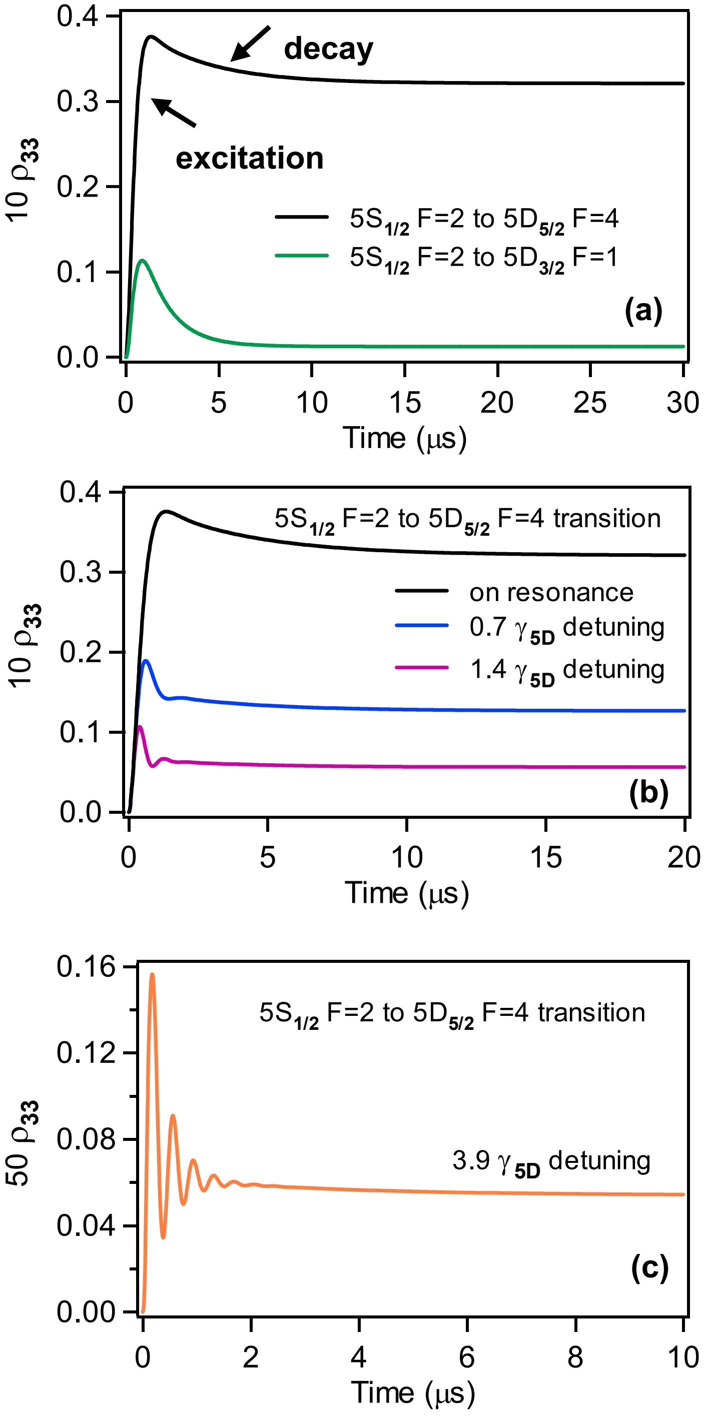

Figure 2.5: Several aspects of population dynamics at short and long timescales:
(a) Time evolution for two resonances, showing the short coherent excitation, followed by the slow incoherent decay. (b) Temporal evolution for one of the previous transitions, for different detunings from the atomic resonance, illustrating the destructive interference that results in the out-of-resonance condition. (c) Oscillation resulting from the phase difference between the atomic frequency and the train of pulses.

in the figure by a quadratic fit. The proportionality of the transition probability to the squared number of pulses N^2 is a more general result, valid in the weak excitation regime, which was theoretically demonstrated for a two-level atom [39], in agreement with earlier conclusions based on perturbation theory [40].

The rapid population increase is accompanied by the narrowing of the resolution linewidth [(Fig. 2.6 (b)], with the obtained resolution limited only by the 5D natural linewidth. After the very first pulse, the linewidth is the single-pulse bandwidth of the laser; as the pulses keep coming, the spectral components from successive pulses interfere among themselves, resulting in the linewidth decrease. Thus, the atoms are the spectrometer used to observe the frequency comb, and the atomic linewidth is the bandwidth limit of this spectrometer.

The dependence of the 5D population and linewidth versus the number of pulses is temporally analogous to the power density scaling and the spatial resolution versus the number of slits in a multi-slit experiment [39, 40]. Again, this is a general result, valid for a broad range of pulse shapes, pulse areas or detunings. The two effects of coherent pulse accumulation on signal strength and spectral linewidth have both been experimentally verified [41]. The quadratic increase of the excited state population versus the accumulated number of pulses can be further enhanced with a larger f_r, where the shorter pulse interval allows for more pulses to be 'added' during the atomic coherence lifetime.

The theoretical model we have developed is designed to predict the coherent accumulation of population in the 5D states, followed by incoherent optical pumping. Using this model we generate atomic transition spectra by tuning either f_r or f_0. We then compare them with the corresponding experimental spectra (covering the same f_r and f_0 range), as presented in Chapter 5. In addition to comparing theory and experiment, we also use the model prediction to adjust the experimental data. For the case of the indirect 5P frequency measurements via the 5S-5D two-photon transitions, described in Chapter 6, we use the theoretical prediction to modify the raw data (after the adjustment, the data fall on top of a Lorentzian).

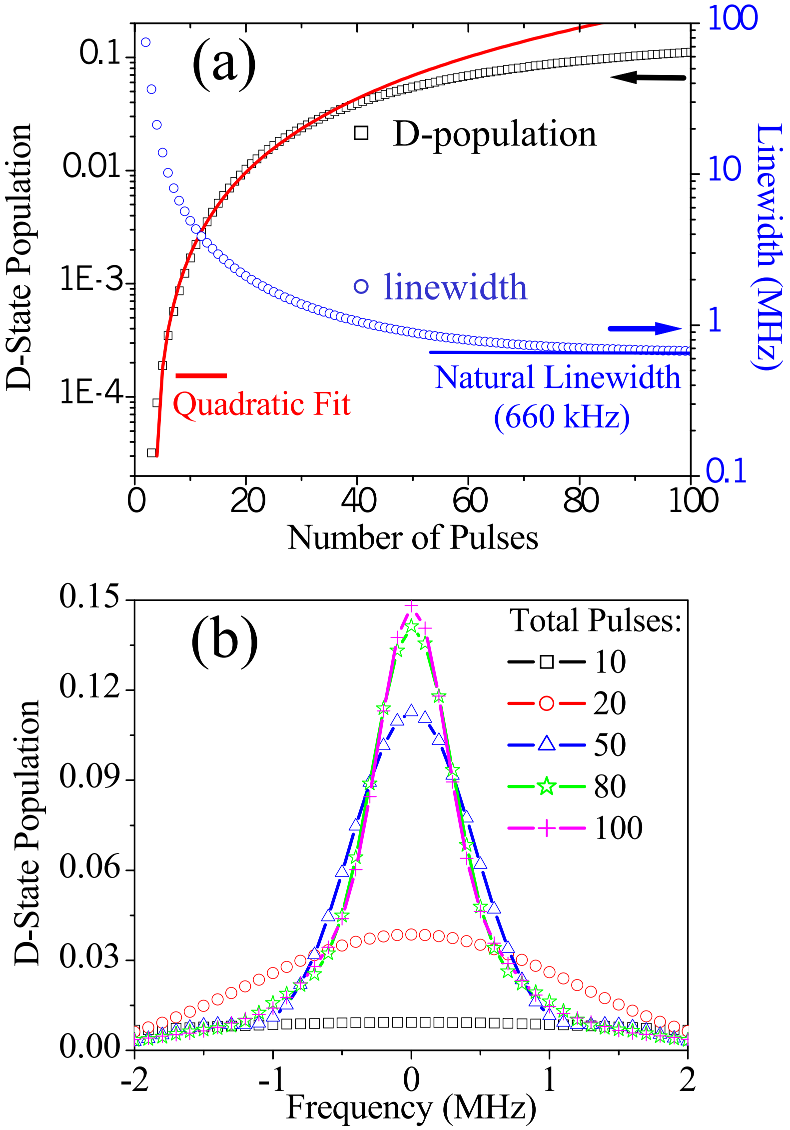

Figure 2.6: (a) Left (right) axis shows calculated 5D population (linewidth) on resonance for the closed two-photon transition versus total number of accumulated pulses. The time between pulses is ∼ 10 ns, and the system reaches its asymptotic values of signal amplitude and linewidth after ∼ 480 ns. The quadratic fit to the 5D population at short times shows that the signal scales as the square of the number of pulses until atomic decoherence limits the coherent pulse accumulation. (b) The corresponding 5D resonance lineshape versus the number of pulses. During the first 10 pulses, the comb structure is not sufficiently developed to offer appreciable signal or resolution.

Chapter 3

Experimental Apparatus: the femtosecond Ti:S setup and the MOT

This chapter discusses the two primary components of the experimental setup, the femtosecond laser and the MOT. I will first present the idea for the Ti:S laser stabilization and then describe one of the most commonly used self-referencing schemes. I will conclude by briefly discussing the stabilization of the cw lasers and the setup used for cooling and trapping in the MOT. Chapter 4 will present the integration of the femtosecond laser and the MOT.

3.1 The femtosecond Ti:S laser and its stabilization setup

Recent advances in controlling the pulse repetition period and the carrier-envelope phase of mode-locked lasers have ushered in a series of novel applications using their frequency combs [42]. In the introduction I presented some of the fundamental aspects of mode-locked lasers. In this section, I will review some of the basic concepts behind carrier-envelope phase stabilization and I will explain how the two dynamic laser parameters are optically detected and stabilized in the experiment. Stabilization of the two degrees of freedom is a necessary step for using these lasers for spectroscopic applications.

3.1.1 Stabilizing the two degrees of freedom of mode-locked lasers

For the experiment, we used a home-built titanium-doped sapphire (Ti:S) laser pumped by a 5 W single-frequency, diode-pumped, frequency-doubled Nd:YVO4 laser (Coherent Verdi) operating at 532 nm. The Ti:S laser generates a 100-MHz pulse train with pulse widths on the order of 15 fs and energies of about 5 nJ per pulse, using Kerr lens mode-locking (KLM). A diagram of our KLM laser is shown in Fig. 3.1. The configuration used is a standing-wave, folded geometry, with the cavity delimited by two flat mirrors: the laser end mirror (EM) and the partially reflective output coupler (OC). The nonlinear gain element for the laser cavity is the Ti:S crystal. The passive mode-locking mechanism employed here is the nonlinear Kerr Effect, which gives an increase in the index of refraction of the crystal as the optical intensity is increased (self-phase modulation, self-focusing, see for example [43]). The Ti:S acts like a nonlinear lens, slightly focusing the intracavity beam, but it also spreads the pulses temporally through normal dispersion (the long wavelengths travel faster than the short ones). As a consequence, a sequence of two prisms is used to compensate for the group velocity dispersion (GVD) in the crystal: the first prism spatially disperses the pulse, leading the long wavelengths to traverse more glass in the second prism than the short wavelengths. The beam is still horizontally dispersed after the second prism, though collimated. Upon reflection by the laser cavity EM, the pulse travels again through the pair of prisms, thus canceling the spatial dispersion.

As mentioned before, f_r determines the mode spacing and is inversely proportional to the cavity length L, $f_r = \frac{v_g}{L}$, while f_0 sets the absolute comb position and is proportional to the intracavity dispersion, $f_0 = \frac{\omega_c}{2\pi}(1 - \frac{v_g}{v_p})$. They are both influenced by the group velocity v_g, but there is no apparent f_0 dependence on the laser cavity length. Ideally one would like to control the two parameters independently. One adjustable parameter can be the cavity length, for f_r control; yet, an additional degree of

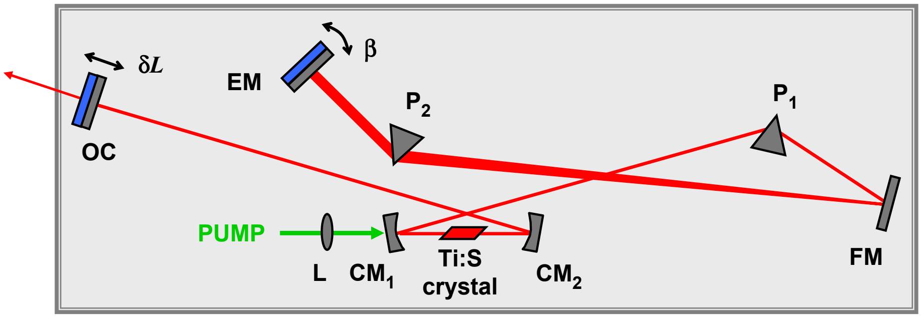

Figure 3.1: Optical layout of the KLM Ti:S laser used in the experiment; the end mirror (EM) and the output coupler (OC) are the two flat mirrors bounding the cavity, used for the f_0 and f_r stabilization, respectively. The two prisms P_1 and P_2 are used for dispersion compensation.

freedom is needed for changing v_g. The one employed in my laser was first suggested in 1999 by the Hänsch group [44] and uses small-angle rotations about the vertical axis of the laser EM. As previously stated, the different spectral components in the laser beam are horizontally spread out at the EM, leading to a linear relationship between the spatial coordinate and the wavelength. For small angle (β) changes, there is a linear path length change, i.e. phase shift, with frequency. This is effectively a group delay, linear with the angle. Under this assumption that the swivel mirror changes the group delay by a small amount $\sim \beta$, it can be shown [28] that f_0 is only controlled by β, while f_r depends on both β and L. Therefore, one can use the swivel angle β to control f_0 (this will also change f_r!), and the cavity length L to compensate for the subsequent change in f_r. Details of the experimental implementation of the v_g, and hence f_0, control will be given in 3.1.5.

3.1.2 Stabilization of the laser repetition rate

The laser repetition frequency f_r is a radio frequency (rf) ~ 100 MHz and is measured directly using a fast photodiode. To reduce the increase in phase noise that is due to the large frequency multiplication factor up into the optical region ($\sim 10^6$), a higher harmonic of the pulse repetition rate is used for stabilization. A portion of the pulse train is detected with a high-speed photodetector; the 10th harmonic of f_r at 1 GHz is filtered and amplified (to 0 dBm, suitable for the rf port of a double-balanced mixer) and then phase-locked to the 1 GHz provided by a stable microwave source. The error signal obtained by comparing against this reference frequency is integrated, filtered and amplified in a JILA-built loop filter (LF) and then used for active feedback to the laser, as shown in Fig. 3.2. Cavity length corrections are controlled with a small ($\sim$ 5 mm) tube piezoelectric transducer (PZT), on which the output coupler of the laser has been mounted. All the comb modes are moved together by this translating PZT which varies the laser cavity length.

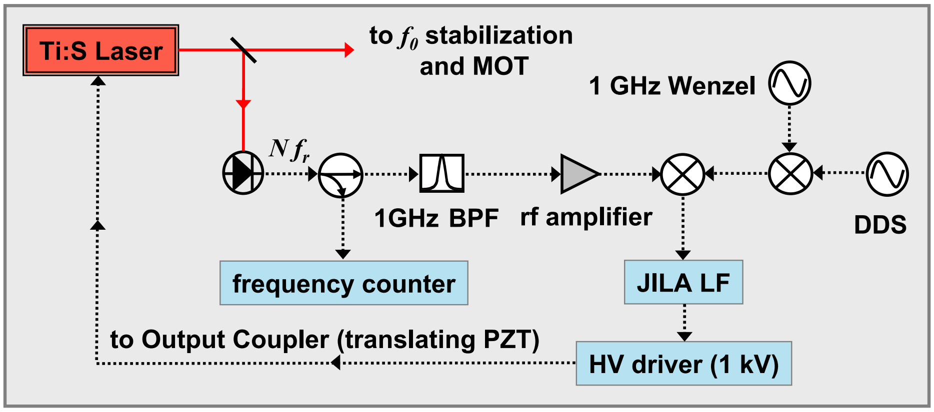

Figure 3.2: Stabilization diagram used for phase-locking of the laser repetition rate f_r; BPF stands for band-pass filter, DDS for direct digital synthesizer and LF for loop filter. More details are given in the text.

Several stable rf oscillators were tried as references for the repetition rate (I will address this issue further in Chapter 4) and in the end a custom-made Wenzel oscillator, based on a crystal oscillator that has a very good short-term frequency stability, was settled upon. The short-term stability of the rf source is very important, given the huge multiplication factor up into the optical domain. Unfortunately, the Wenzel tuning range is only 3.2 kHz around 1 GHz, corresponding to a 320 Hz tunability of the repetition rate very close to 100 MHz. One would like to have more freedom than that in choosing a suitable f_r value, so an extra direct digital synthesizer (DDS) had to be later added to the stabilization setup. Its widely tunable output ($\sim$ MHz) is mixed with the Wenzel and the repetition rate is forced to track the resulting frequency via the phase lock described above.

3.1.3 Self-referencing

In 1999 Telle and coworkers suggested several methods allowing for direct measurement and stabilization of the frequency offset of the fs comb, without using another optical standard [21]. These 'self-referencing' methods employ non-linear processes like second harmonic generation to compare the spectral extremes of the comb. In that work, it is shown that frequency-doubling of a number of modes from the infrared end of the spectrum and heterodyning them with the existing visible section of the spectrum will result in a beat frequency, equal to the offset of the fs comb from integer multiples of the repetition rate:

$$2\,\nu_N - \nu_{2N} = 2\,(Nf_r + f_0) - (2\,Nf_r + f_0) = f_0. \tag{3.1}$$

Thus, f_0 can be derived directly from the beat note, with no knowledge of the laser repetition rate. The requirement for this detection scheme to work is that the frequency comb contain on the blue side the second harmonic of the red side, i.e. that the laser optical bandwidth cover an optical octave. Along the same line of thought, the use of mode-locked lasers for absolute metrology of optical frequencies, where the frequency of every comb line is an integer multiple of the fixed comb spacing ($f_0 = 0$), was suggested in a NIST competence proposal from March 1999 [45].

Fortunately, the introduction in 2000 of special air-silica microstructure (MS) optical fibers [22], which broaden the output of the fs comb to span an entire optical octave solved the bandwidth requirement. These photonic crystal fibers have a very small core diameter (1.7 μm), providing a very tight spatial confinement that generates very high intensities ($\sim$TW/cm^2). They have been engineered to exhibit zero GVD near 800 nm, which minimizes the temporal spread of the pulses propagating in the fiber over significant distances (several cm). The main non-linear effect leading to spectral broadening in the fiber is strong four-wave-mixing among the different frequency components in the input pulse spectrum, which generates new spectral components, while maintaining the periodicity of the incoming frequency comb. The spectral bandwidth at the output of the MS fiber can extend well beyond one optical octave e.g. 400 to 1200 nm.

The first experimental implementation of the self-referencing technique using external broadening in a MS fiber, followed by doubling of the 1040 nm light and mixing with the fundamental at 520 nm, was reported by Jones and co-workers in 2000 [1]. Ultra-broadband mode-locked lasers whose direct output spans on optical octave, allowing for direct self-referencing and stabilization of the pulse train, have also been recently demonstrated [7].

3.1.4 The ν-to-2ν prism interferometer

To achieve spectral broadening, $\sim$ 120 mW of the fs laser output light ($\sim$ 500 mW) are coupled into a $\sim$ 7-cm piece of MS fiber. The output of the fiber is then sent into an ν-to-2ν interferometer for self-comparison.

The configuration chosen for the interferometer is the so-called 'prism-pair' geometry, presented in Fig. 3.3. The sequence of SF10 prisms (8-cm prism separation) spatially separates the green (e.g. 532 nm) and red (e.g. 1064 nm) components of the spectrum, which are then reflected by two mirrors located very close to each other. The green-reflecting mirror is mounted on a translation stage, to easily adjust the temporal overlap between the red and green pulses at the detector. When the interferometer is well aligned and working, the distance between the end mirrors is $\sim$ 1 mm.

The beams retrace their path through the prism pair with a slight vertical offset

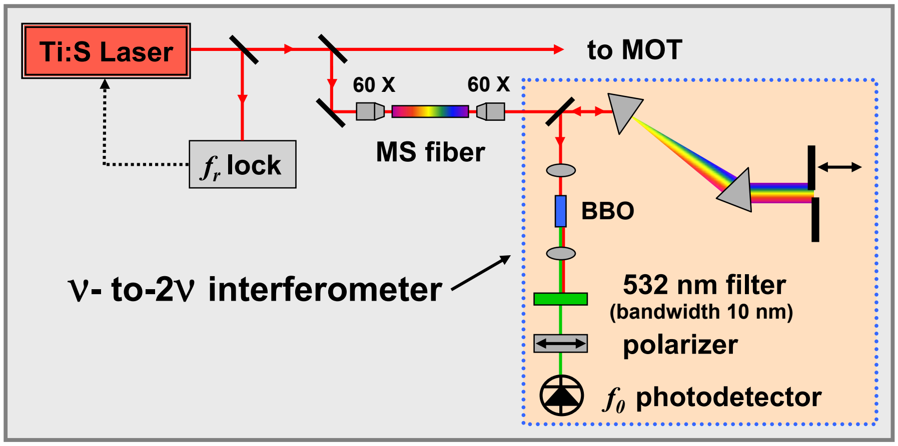

Figure 3.3: Diagram of the prism interferometer used for the detection of the comb offset frequency. The broad spectrum from the MS fiber is sent into a prism pair for spatial dispersion. The light near 532 nm is reflected by one end mirror, while the light near 1064 nm hits a second end mirror. Both beams are reflected back through the prism pair, recombined and then sent through a nonlinear BBO crystal tuned for efficient second harmonic generation at 1064 nm. The output is filtered, and the f_0 beat is detected on a PD.

in order to be picked off by a mirror positioned below the incoming beam. The pick-off mirror sends the recombined beams to a lens, which focuses them into a nonlinear crystal (1-mm BBO, type I phase-matching), angle-tuned for efficient second harmonic generation at 1064 nm.

Two types of green light are present at the output of the BBO crystal: the frequency-doubled beam obtained from the infrared part of the spectrum and the fundamental green coming out of the MS fiber; the polarization of the frequency-doubled green is rotated by 90 degrees with respect to the fundamental green. A 10-nm interference filter centered at 532 nm removes the extra, non-contributing spectral components, while a polarizer ensures that the polarizations of the two green beams are aligned along the same axis. Spatial overlap and mode-matching of the two beams are essential for a good signal-to-noise ratio (S/N) of the beat signal. A photodiode detects their difference frequency, the f_0 beat, along with the laser repetition rate. In reality, the detected beat arises from mixing of thousands of comb lines, not just the two frequencies mentioned, giving a better S/N. In the experiment, the typical S/N of the offset beat is ~ 45 dB in a 100 kHz resolution bandwidth.

The prism pair geometry is advantageous to use compared to other configurations, e.g. a Mach-Zender interferometer, because most of its elements are common-mode (the only differential path is the prism pair region), which makes it easier to align and tweak.

3.1.5 Stabilization of the laser offset frequency

The output of the ν-to-$2\,\nu$ PD is sent through two 50 MHz low-pass filters (LPF), to reduce all the unnecessary rf frequencies in the spectrum (otherwise, they would saturate the subsequent amplifiers), then a small portion of the signal is sent via a directional coupler to an rf spectrum analyzer for monitoring of the beat note. The main signal is amplified to $\sim$-5 dBm and then frequency-prescaled (divided by 64) before its phase is compared to a stable rf oscillator such as a DDS. Unlike the f_r lock which employs an analog phase detector, the stabilization circuit used for f_0 employs a digital phase detector (DPD), which provides both a frequency and a phase lock. This allows for a larger capture and locking range than the double-balanced mixer case and increases the stability of the lock. Again, the error signal derived by comparing against the reference frequency is integrated, filtered and amplified in a JILA LF (see Fig. 3.4) and then sent to the laser for frequency correction. Note that the local oscillators used for the f_r and f_0 stabilization are all referenced to the same local commercial cesium clock.

As announced earlier in section 3.1.1, f_0 control is carried out by fine-tuning the laser end mirror angle using a twister PZT. The twister PZT used to tilt the end mirror is a 0.5 inch diameter cylinder, about 0.5 inch long, that has been modified such that the outer electrical surface is split to allow for the two outer sides to have different voltages with respect to the inner surface of the PZT. When applying opposite-sign voltages to

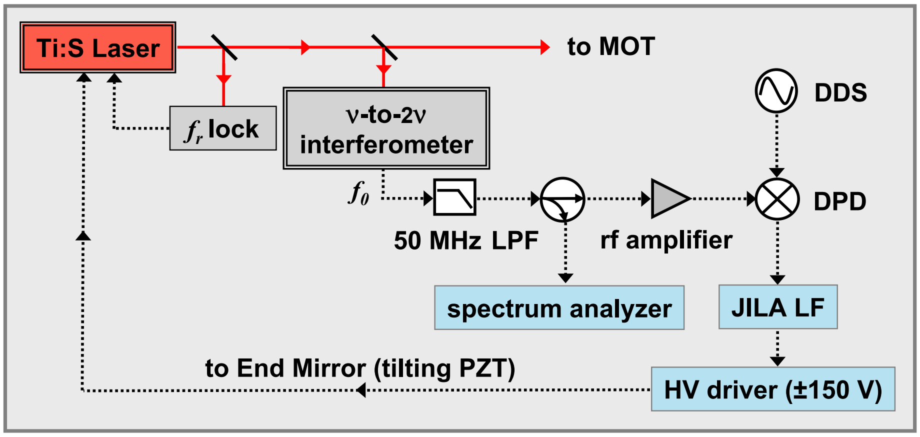

Figure 3.4: Stabilization diagram used for phase-locking of the laser offset frequency f_0; LPF stands for low-pass filter, DPD for direct phase detector, DDS for direct digital synthesizer and LF for loop filter. The details are given in the text.

the two sides, one contracts, while the other expands, with the net effect of an angle change for the end mirror mounted on the PZT. As mentioned before, this is effectively a group delay, which depends on the voltage sent to the PZT. Changing the voltage in the 0 to ± 150 V range allows for scanning of the offset frequency beat over its full range of ~ 50 MHz.

Another method of adjusting and stabilizing f_0 is employing an acousto-optic modulator (AOM) to control the pump laser power. Modulating the pump laser power actually affects several laser parameters. Systematic studies of intensity-related dynamics in mode-locked Ti:S lasers have been recently undertaken [46, 47] to understand the effects on f_r and f_0.

To summarize, f_r and f_0 stabilization and referencing to an atomic clock result in knowledge of the absolute frequencies of the $\sim 10^6$ comb lines, with an accuracy only limited by the frequency reference used. The stabilized comb can now be employed as a precision frequency ruler for any optical frequency in the visible to near-infrared range.

3.2 The MOT

The magneto-optical trap (MOT) is currently the starting point for many experiments with laser-cooled atoms. Cold atoms are used for precision measurements, atom interferometers, atomic clocks, to name just a few examples. Advances in laser cooling of alkali atoms [48] have also paved the way to producing the first Bose-Einstein condensates and degenerate Fermi gases [49–51]. In particular, vapor-cell traps [52] like the one used in this experiment, are simple and versatile tools for many experiments with cold atoms.

Our experiment was performed on a sample of laser-trapped and -cooled Rubidium 87 atoms (see Fig. 4.2 for a detailed ^{87}Rb level diagram, I=3/2). The $5S_{1/2} \rightarrow 5P_{3/2}$ cooling transitions can be easily accessed with commercially available laser diodes centered at 780 nm, making ^{87}Rb a convenient choice for laser cooling and trapping. We use two lasers to trap and cool the atoms. The cooling beams are $\sim$10 MHz red-detuned from the $5S_{1/2}$ (F=2) $\rightarrow$ $5P_{3/2}$ (F$'$=3) cycling transition. An additional laser, the so-called 'repumper', tuned to the $5S_{1/2}$ (F=1) $\rightarrow$ $5P_{3/2}$ (F$'$=2) transition, is needed to return the atoms to the cooling cycle whenever they decay to the F=1 ground level, thus preventing them from falling dark due to optical pumping.

3.2.1 Diode lasers: description and stabilization

The laser diodes used are Sharp LT024MD (specified output power of 20 mW) for the repump laser (RL) and Sanyo DL7140-201 (specified output power of 70 mW) for the trap laser (TL). They are configured in an external cavity geometry, based on a design described in reference [53, 54], with ~ 3.5 cm extended cavity length. The lasers employ a diffraction grating (1200 lines/mm) aligned in the Littrow configuration [55] to couple the first diffraction order back into the laser. One PZT controls the horizontal tilt of the grating, permitting adjustments of the laser wavelength. A change in the PZT length alters the grating angle and the external cavity length at the same time, allowing for continuous scans of typically ~ 5 GHz. Additionally, the grating is mounted on a fast disk PZT, which is servoed together with the laser diode current to stabilize the laser frequency.

Both diode lasers are locked to the specified atomic transitions using standard saturated absorption spectroscopy [53], which yields sub-Doppler hyperfine lines that are used to frequency-stabilize the laser (see Fig. 3.5). The TL is locked to the red side of the saturated absorption peak; a side lock is not ideal, since the locking set point is inevitably dependent on power broadening of the transition lines. We use acousto-optic modulators (AOMs) to create beams at various detunings and also to control the timing of the lasers in the experiment. The TL light is steered through two AOMs: the first AOM deflects a small amount of power (-1 order) into the saturated absorption spectrometer, for frequency stabilization. The second AOM acts as a shutter for the light, by directing the negative first order diffracted beam to the MOT cell. Thus, the MOT red detuning is set by the side lock along with the frequency difference of the two AOMs.

The RL is locked to the peak of the crossover transition between the $5S_{1/2}$ (F=1)$\rightarrow$ $5P_{3/2}$ (F$'$=1) and the $5S_{1/2}$ (F=1) $\rightarrow$ $5P_{3/2}$ (F$'$=2) transitions, using modulation sidebands at 4.6 MHz, written directly on the diode-laser current (the laser output current can be modulated rapidly by sending a voltage into the rf modulation input, this in turn will modulate the frequency of the laser). The signal from the RL saturated absorption spectrometer is detected with a homemade resonant photodetector (PD) and then compared in a double-balanced mixer with the local oscillator at 4.6 MHz, resulting in dispersion curves for all the features in the saturated absorption spectrum [56, 57]. The value of these dispersion curves changes sign at the peak, allowing for a lock at the zero-crossing of the error signal. Since the RL is offset peak-locked, an AOM is needed to shift the frequency into resonance with either the $5S_{1/2}$ (F=1)$\rightarrow$ $5P_{3/2}$ (F$'$=1) or the

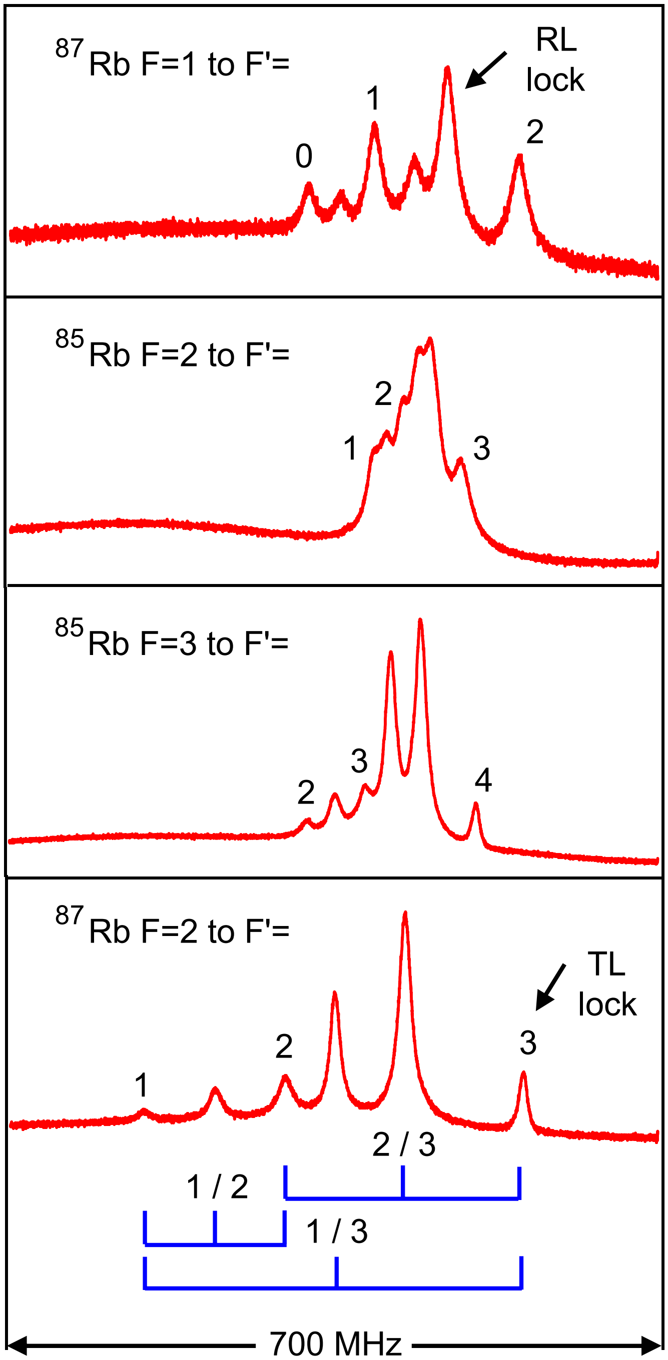

Figure 3.5: Saturated absorption spectra, showing the hyperfine structure of the $5S_{1/2} \rightarrow 5P_{3/2}$ transitions for the two Rb isotopes. The numbers labeling the hyperfine peaks correspond to F′ states in the $5P_{3/2}$ manifold. Note that the spectra contain both true Doppler-free resonances (numbered peaks) and crossover resonances. The crossover resonances occur at frequencies $(\nu_a + \nu_b)/2$ for each pair of true resonances at frequency ν_a and ν_b, as exemplified for the bottom spectrum.

$5S_{1/2}$ (F=1) → $5P_{3/2}$ (F′=2) transition. We opted for the latter and thus the positive first order deflected beam is sent to the MOT vapor cell. In order to operate the trap at zero repump detuning, the driving frequency for the RL AOM is equal to exactly half of the F′=1– F′=2 $5P_{3/2}$ hyperfine interval (78.45 MHz). This AOM is a fast and convenient switch used to turn off the RL beam whenever needed.

3.2.2 MOT details

The main TL beam is spatially filtered by a 70 μm pinhole, which reduces the high-frequency spatial modes, and collimated to roughly a 1-cm beam diameter with a beam-enlarging telescope. It is then divided into three separate, intensity-balanced beams using $\lambda/2$ plates and polarizing beamsplitter cubes. The three beams are sent to the experiment glass cell using 1-inch diameter optics, in a standard retro-reflected MOT configuration [58]. The atoms are caught in the MOT using these three pairs of orthogonal, circularly-polarized beams in the typical $\sigma^+ - \sigma^-$ arrangement, and detuned $\sim$ 10 MHz to the red of the atomic resonance. The RL beam is directed into the cell along one of the TL beams. We monitor the beams in the cell and the position of the trapped cloud with a low-cost CCD camera.

We load the MOT from the vapor produced by Rb dispensers (‘getters’) in a cylindrical glass cell. The vapor cell is continuously pumped by an ion pump and typically reaches a background pressure of 10^{-9} Torr. The source of Rb consists of three nichrome (Ni-Cr alloy) dispenser strips, connected in parallel and placed in a small side arm of the cell. They contain a Rb salt and release atoms through a chemical reaction when an electric current is passed through them and heats the nichrome. Only one dispenser is used at a time, and the operating current is usually 3.5 A.

The quadrupole magnetic field necessary to operate a MOT is provided by a pair of anti-Helmholtz coils. The two coils are wound from ‘magnet wire’, i.e. Cu wire ($\sim$ 1 mm diameter) coated with an insulating material, and are wrapped around the axis of the cylindrical cell. Each coil is 7 cm in diameter and has 33 turns. The coils are spaced 5.5 cm apart and are supplied with ~ 4.5 A, generating a magnetic field gradient of $\sim$ 10 G/cm.

Stray magnetic fields, due mainly to the Earth's field, can shift the zero-point of the MOT field. They are compensated by three pairs of orthogonal Helmholtz coils. The glass cell is surrounded by these pairs of shim coils, each run by a different current supply. In the early stages of the experiment, the beam alignment and ambient magnetic field compensation were verified by monitoring the isotropy of the molasses expansion. We were aiming for a slow and uniform expansion of the atomic cloud upon switching off the quadrupole field. At a later stage, after obtaining the two-photon signal as described in Chapter 4, we realized that we could use it to find the zero-point of the magnetic field.

Resonance fluorescence from the atoms is detected with a photodiode (PD), leading to an estimate of the atom number based on the PD current, the PD responsitivity, the solid angle of the light collected by the imaging lens, the energy of a photon and the optical scattering rate. We typically trap 5×10^6 atoms in a 0.5 mm diameter MOT with a 1/e lifetime between 3 and 5 s.

After collecting the atoms in the MOT, we transfer them to optical molasses [59] for further cooling using polarization gradients (PGC). To experimentally implement PGC, the quadrupole field gradient is turned off, the TL is further red-detuned from resonance ($\sim$ 40 MHz) and the TL beam intensity is decreased. The resulting sub-Doppler cloud temperature established by PGC is $\sim 15\ \mu$K, providing an ideal initial condition for spectroscopy.

I have presented here the basic operation details of the MOT. In Chapter 4 I will describe how the trapped atoms are probed with the frequency comb of a femtosecond laser.

Chapter 4

Characterization of the systematic effects related to direct frequency comb spectroscopy

We would like to use a phase-stabilized femtosecond laser comb directly for high-resolution spectroscopy and absolute optical frequency measurements of one- and two-photon transitions in laser-cooled ^{87}Rb atoms. We defer further discussion of the spectroscopy, however, until we have explored some of the important sources of possible systematic error [60]. In section 4.4.2, I will discuss both experimentally and theoretically the mechanical action of the probe on the atoms. I will then present the AC Stark frequency shifts induced by the femtosecond light in section 4.4.3. Finally, the last systematic error we studied, arising from Zeeman shifts, will be presented in section 4.4.4. As briefly mentioned in Chapter 3, the short-term stability of the reference used to stabilize the repetition rate also warrants attention. We will see that the main contributions to the systematics are those arising from mechanical effects and the AC Stark shifts.

4.1 Doppler-free two-photon transitions with cw and pulsed sources

Study of two-photon transitions to achieve high-resolution spectroscopy or to maximize the excitation efficiency of a desired state has been an active field of research in the past decades. Doppler-free multi-photon transitions have been theoretically studied by Cagnac *et al.* [61]. The first experimental demonstrations followed shortly, by observing two-photon absorption resonances in Na using tunable dye lasers [62–64]. The effects of Doppler broadening in the vapor were eliminated by making the atoms absorb one photon from each of the two equal-energy, counterpropagating cw beams (Fig. 4.1, top panel).

In a closely related experiment, optical beams were arranged to both (i) propagate in opposite directions as well as (ii) have unequal frequencies (Fig. 4.1, bottom panel). This configuration was used to demonstrate resonantly enhanced two-photon absorption in Na vapor [65]. The two-photon absorption cross-section was enhanced by over 7 orders of magnitude, by letting one of the photons be nearly resonant with an intermediate state. Doppler effects were greatly reduced by using counter-propagating beams, but not totally eliminated. In a different experiment, the two-photon transition rate was resonantly enhanced by using a fast atomic beam [66], where the high atomic velocities allowed for Doppler tuning of an intermediate state into exact resonance in the rest frame of the atom.

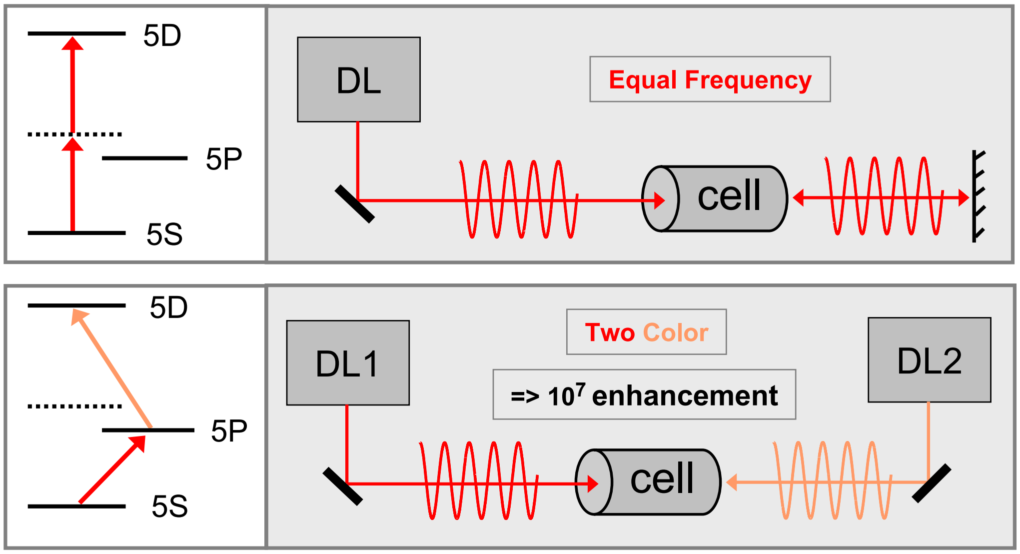

Figure 4.1: Schematic of Doppler-free two-photon spectroscopy in a cell, with equal-frequency (top) and two-color (bottom) counterpropagating beams.

Doppler-free two-photon spectroscopy has also enabled the observation of optical Ramsey fringes. In the experiments of Salour [40, 67] the atoms have interacted with two time-delayed phase-coherent laser pulses, while Baklanov *et al.* have suggested two spatially separated light standing waves [68]. Note that Bergquist *et al.* have observed Ramsey fringes in the saturated-absorption signal from a fast beam of Ne* atoms crossing three and four equally spaced spatially separated standing-wave beams [69].

With regard to employing pulsed sources, high-resolution two-photon spectroscopy using picosecond pulsed light and hence, without any appreciable intermediate-state interaction or absolute frequency reference, has been previously demonstrated [27], with a recent extension to laser-cooled samples [70]. Cold atoms confined in a MOT provide an almost-Doppler-free environment for use in spectroscopic studies. For the case of two-photon transitions, where the absorption cross sections are relatively small and thus the required intensities are rather large, the cold sample mitigates the Doppler broadening arising from the strong focusing needed.

The advent of ultrafast lasers combined with pulse-shaping techniques has led to new schemes [14, 71], where two-photon transitions which constitute the lowest-order nonlinear interaction, are used as a benchmark system. In particular, Silberberg and coworkers have shown that the two-photon absorption rate is maximized for transform-limited pulses only in the case of transitions without any resonant intermediate state. For transitions involving a nearly resonant intermediate state, an enhancement by a factor of 7 of the two-photon absorption rate in Rb vapor has been obtained by shaping the pulse [71]. Thus, the final population transfer was controlled by manipulating the coherence properties of the optical field.

4.2 Background for the technique of two-photon DFCS

We directly interrogate a sample of laser-cooled ^{87}Rb atoms with a frequency comb and induce two-photon transitions. This capability is enabled by the bandwidth

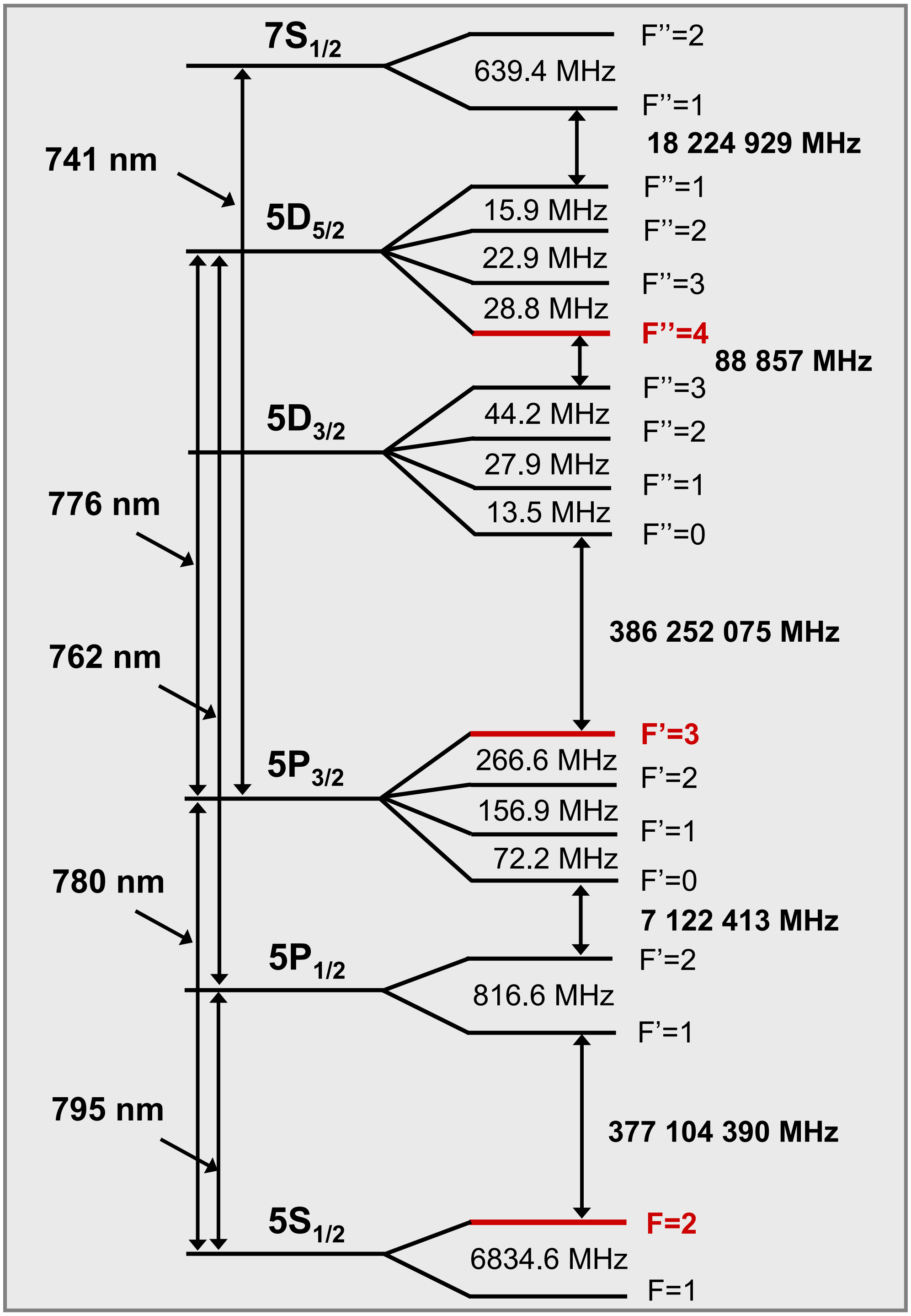

Figure 4.2: Schematic of the ^{87}Rb energy levels participating in the one- and two-photon transitions we studied, including the wavelength and energy level information. The levels highlighted in red correspond to the **closed 2-3-4** transition pathway (section 4.4). We have investigated seven two-photon transitions, as detailed in section 5.2.

associated with the femtosecond pulse, which is sufficiently broad that many fine and hyperfine atomic states (see Fig. 4.2) can be excited by tuning the relevant comb components into resonance. The two independent parameters f_r and f_0 provide freedom in choosing an appropriate frequency comb for control of resonant signal enhancement via the intermediate $5P_{1/2}$ and $5P_{3/2}$ states.

Our experimental prototype system to study DFCS is therefore a set of two-photon transitions from the ground-state $5S_{1/2}$ to the excited $5D_{3/2}$ and $5D_{5/2}$ states, enhanced by the 5P intermediate states as shown in Fig. 4.3. The dipole-allowed intermediate states, $5P_{3/2}$ and $5P_{1/2}$, are located $\sim$ 2 and 17 nm (i.e. $\sim$ 1 and 8 THz) below the energy degenerate virtual level for the two-photon transition, respectively (Fig. 4.2). The lifetime of the 5P intermediate states is 27 ns, the lifetime of the 5D states is 241 ns and the lifetime of the 7S states is 88 ns [72].

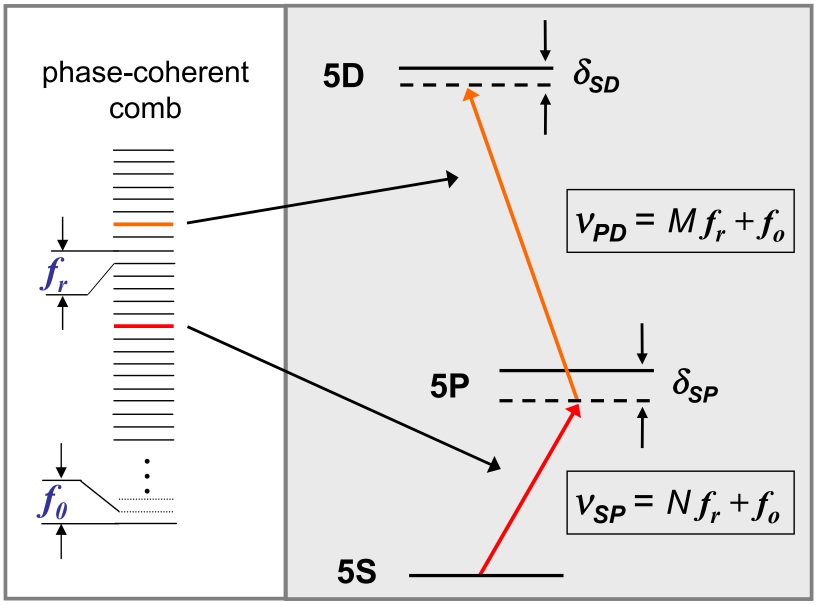

Figure 4.3: Resonantly enhanced two-photon transition with detunings δ_{SP} and δ_{SD} for the pair of comb modes that makes the dominant contribution to the transition probability.

As mentioned in Chapter 1, the optical frequency of a particular comb mode can be expressed as $\nu_N = Nf_r + f_0$, where f_r is the pulse repetition rate, f_0 is the carrier envelope offset frequency, and N is an integer on the order of 10^6. The sum frequency of the light from two comb lines labeled by N and M is given by $\nu_{2\gamma} = (N + M)f_r + 2f_0$. There are several hundred thousand comb pairs (N, M) that yield the same sum frequency and thus could contribute to the transition amplitude when $\nu_{2\gamma}$ is resonant with the two-photon transition ($\delta_{SD} \sim 0$ as shown in Fig. 4.3). However, in estimating their relative contributions, it is necessary to consider the intermediate 5P states that provide resonant enhancement.

When one of the comb lines is tuned near resonance with one of the 5S-5P transitions ($\delta_{SP} \sim 0$ as shown in Fig. 4.3), the resonant enhancement causes the corresponding pair to make the dominant contribution to the two-photon transition over all of the other pairs. This dominant contribution is reinforced by destructive quantum interference between comb pairs symmetrically detuned on either side of the P state, resulting in a $\sim 180°$ phase difference [71]. For the non-resonant configuration of comb modes detuned $\pm kf_r/2$ ($k \geq 1$, odd integer) away from the P state, with all pairs satisfying the two-photon resonance, the transition amplitudes associated with (+k) and (-k) modes will again destructively interfere. However, there will be a net non-resonant contribution due mainly to the existence of multiple P states that break the symmetry of the comb distribution. This destructive interference can be made constructive by flipping the spectral phase about the P state [71].

The two-photon transition spectrum is obtained by scanning f_r or f_0; their precisely measured values, along with (N, M), determine all relevant atomic energy levels in absolute terms.

4.3 Experimental method

The experiment is performed with an optical frequency comb (emitted from a 20-fs, 100-MHz repetition rate, mode-locked Ti:sapphire laser) centered at 778 nm with

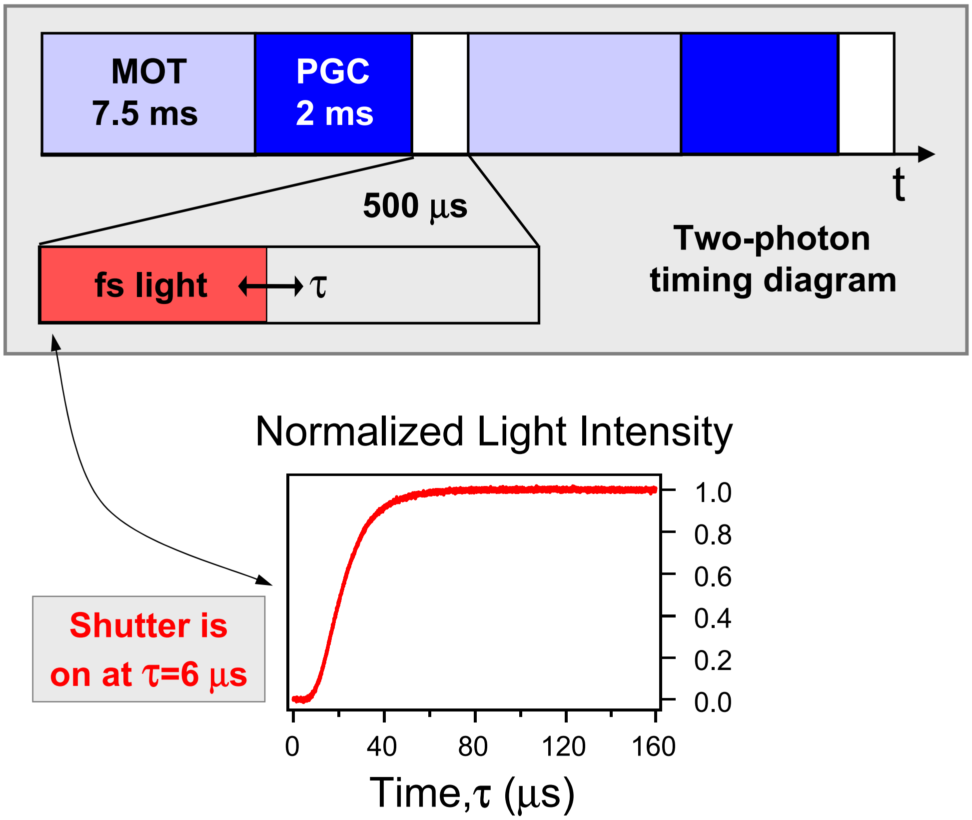

Figure 4.4: Timing scheme for the 100 Hz experiment cycle. The atoms are first loaded in the MOT for 7.5 ms and then, at the end of the loading time, the trapping quadrupole magnetic field is extinguished (not shown). Additional cooling of the atoms is done with polarization gradients (PGC) for 2 ms. All MOT-related fields are turned off at the end of the PGC stage. At this point, the femtosecond laser is switched on using the liquid crystal shutter (30-μs response time). The 500-μs zoom window shows the variable probe window (τ) used for the two-photon measurements. Signals are averaged over hundreds of 10 ms experiment cycles.

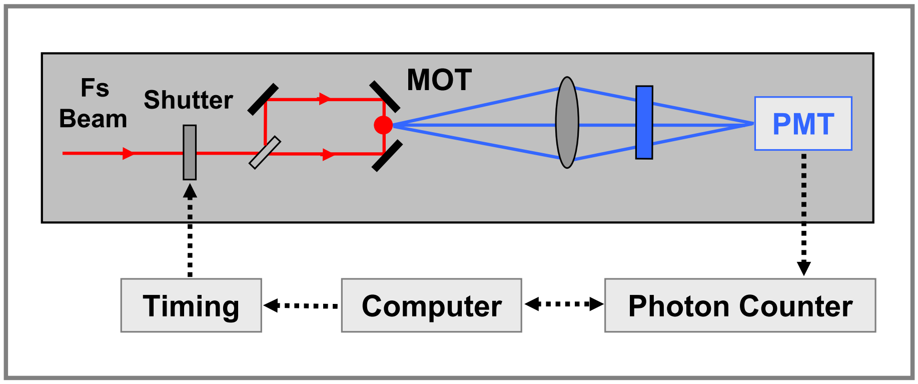

Figure 4.5: Shown here is the optical configuration for the counterpropagating beams, implemented in all our two-photon studies, including those described in Chapters 5 and 6. The 420-nm blue fluorescence detected by the PMT is sent to a photon counter and then read into the computer.

a full width at half maximum bandwidth of ~ 55 nm (~ 26 THz). There is ~ 200 nW of power in each of the comb lines resonant with the 5S-5P and 5P-5D transitions. The light is typically focused to a beam waist of 130 μm, giving an on-axis intensity of ~ 0.8 mW/cm^2 in each comb line. For time-resolved studies, the sample is exposed to light by a liquid crystal with a 30-μs response time.

As described in Chapter 3, the atomic source is a cloud of ^{87}Rb trapped and cooled in a vapor-cell MOT. As shown in Fig. 4.4, the typical loading cycle used for the MOT is 100 Hz and the sequence of the experiment is as follows: the atoms are loaded in the MOT for 7.5 ms, then the quadrupole magnetic field for the trap is switched off, the atoms are further cooled with polarization gradients (PGC) for 2 ms, then all the MOT beams are extinguished, the femtosecond comb beam is switched on for 500 μs using the shutter, and finally, the 420 nm fluorescence is detected.

The cw MOT repumping laser controls the initial populations of the two ground-state hyperfine levels. During the actual probing period, the femtosecond comb itself acts as a repumper, allowing one to maintain a stable population in the initial ground state.

The excited 5D state population is determined from the 5D-6P-5S radiative cascade: the atoms relax to the 6P state and then decay down to the ground state, emitting photons at 420 nm. These blue photons are detected with a photomultiplier tube (PMT) centered (Fig. 4.5) at 420 nm and are counted and subsequently time-binned with a multi-channel photon counter, with a typical integration time of 10 μs. In general, signals are averaged over hundreds of 10-ms experiment cycles.

One of the main problems in acquiring reproducible data is that the femtosecond laser is located on one optical table, and the Rb apparatus on a different optical table $\sim$10 meters away. This creates serious beam-pointing instabilities. We have implemented a beam-steering servo based on a quadrant photodiode and a tip/tilt mirror to actively control the beam pointing.

4.4 Main systematic effects

As in the case of precision spectroscopy performed with cw lasers, the use of the femtosecond comb as a precision probe requires a careful understanding of all systematic effects. Indeed the dominant effects are the mechanical effect of the optical comb on the atomic motion, the light shift by the probe laser, and the Zeeman frequency shifts. The short-term stability of the rf source used to reference f_r is also important, as discussed in the next section.

We have performed all studies of the systematics involved on one sample transition, namely the $5S_{1/2}$ (F=2)→ $5P_{3/2}$ (F′=3)→ $5D_{5/2}$ (F″=4) closed two-photon transition, which gives the best signal-to-noise ratio. A closed transition is defined to be a transition which decays back to the hyperfine level from which it was excited. I have highlighted in Fig. 4.2, in red, the states involved in the only closed two-photon transition occurring in ^{87}Rb among the levels shown. This closed transition occurs when the atoms start in the F=2 state, are then excited to the F′=3 state, and then to the F″=4 state and finally decay back to the F=2 state (through either the 5P or the 6P channel).

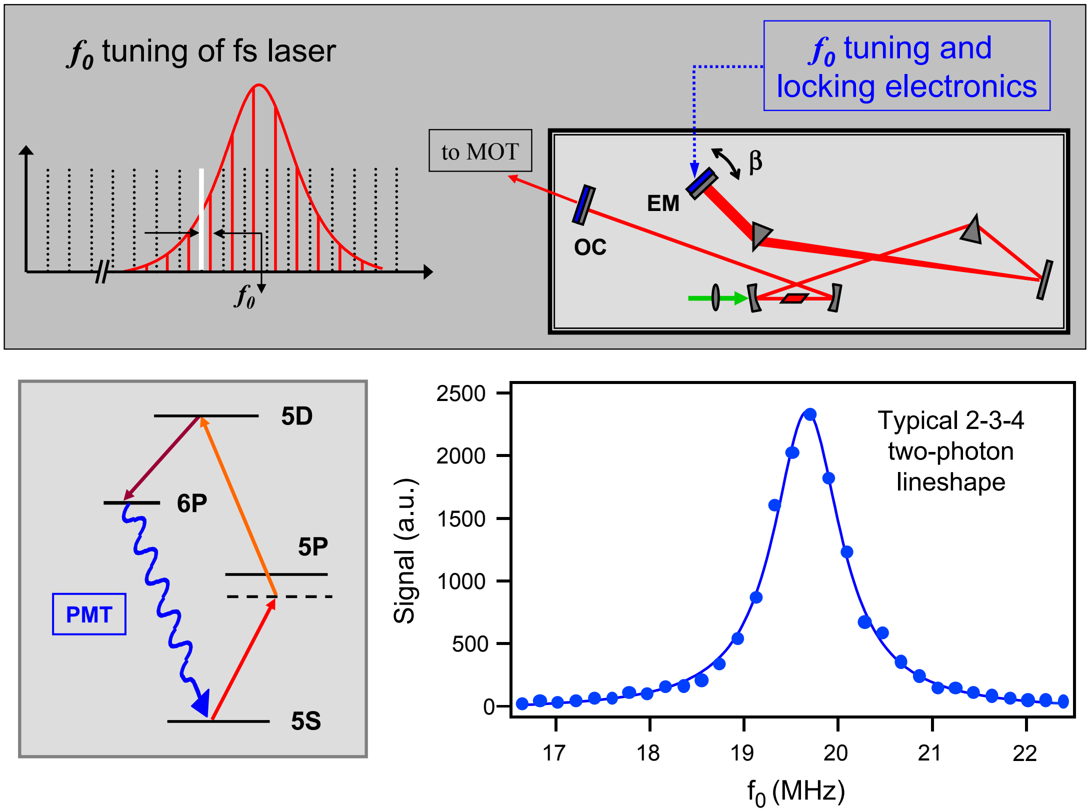

Figure 4.6: The top panel shows the experimental setup for scanning f_0 and the lower panel presents a typical $5S_{1/2}$ (F=2)→ $5P_{3/2}$ (F′=3)→ $5D_{5/2}$ (F″=4) (‘2-3-4’) closed two-photon lineshape obtained from such a frequency scan. The decay channel used for detecting the population of the 5D excited state is also shown.

In contrast, note for example that the transitions F=2 to F$'$=1 or 2 are not closed, since they have a decay channel to the F=1 ground hyperfine level and thus, the atoms do not all return to the initial F=2 state. In summary, the 2-3-4 is a closed transition because for each of the two steps 5S-5P and 5P-5D, the electric dipole selection rule ($\Delta F = 0, \pm 1$) prevents the excited atoms from falling into the F=1 ground state.

As a convention, any two-photon process starting in F=2 that accesses the F$'$=3 state will be referred to as having a closed first step. We will study all of the two-photon transitions that have a closed first step in Chapter 5.

For all of the systematic studies, we will scan the closed two-photon transition repeatedly, taking note of how the line center and linewidth are affected by the changes we implement. We will use an f_0 scan, meaning f_r is locked while f_0 is swept (Fig. 4.6). As a reminder, controlling f_0 causes a rigid spectral shift of the optical comb, where the frequency of all the lines is changed without modifying the comb spacing.

4.4.1 Stability of the reference for the pulse repetition rate

As detailed in Chapter 3, both the repetition rate and the carrier-envelope phase of the fs laser are locked to radio-frequency oscillators with ultra-low phase noise.

At fast time scales, the femtosecond laser repetition frequency has less phase noise, in other words it is more stable, than the best rf sources available. Therefore, it may be that we are writing fast noise onto the laser if we lock it too tightly to an external standard such as frequency synthesizer. Thus, after frequency multiplication up into the optical domain, customary rf sources are not useful as a means to stabilize the laser in the short term. As a reminder, we are using a custom-made crystal oscillator (Wenzel) that has very good short-term stability (fractional instability of 5×10^{-13} for an averaging time of 1 s). At long times though, the Wenzel drifts, which is a potential inconvenience when doing a long data run. For all the important measurements we count the repetition rate as we acquire data. The radio frequency counter and the local oscillator used for the f_0 stabilization are both referenced to the same local commercial cesium clock. A slow servo control of the repetition rate is helpful in reducing the laser frequency noise and drift resulting from lab vibrations and thermal drift of the laser cavity.

We are able to lock the repetition rate to a number of different sources, including two synthesizers referenced to a NIST hydrogen maser signal (fractional instability of 3×10^{-13} at 1 s), which were used as rf sources for the f_r stabilization. The maser signal was transferred to JILA through a single-mode fiber using amplitude modulation of a cw laser [73]. Figure 4.7 has the resulting two-photon lineshape for the three standards used. We observed that the two-photon linewidth for the case of the NIST synthesizers was consistently broader than the Wenzel-referenced situation. We attribute this to the short-term noise of the synthesizers being worse than the Wenzel, and possibly to fast phase noise in the optical fiber used for signal transfer.

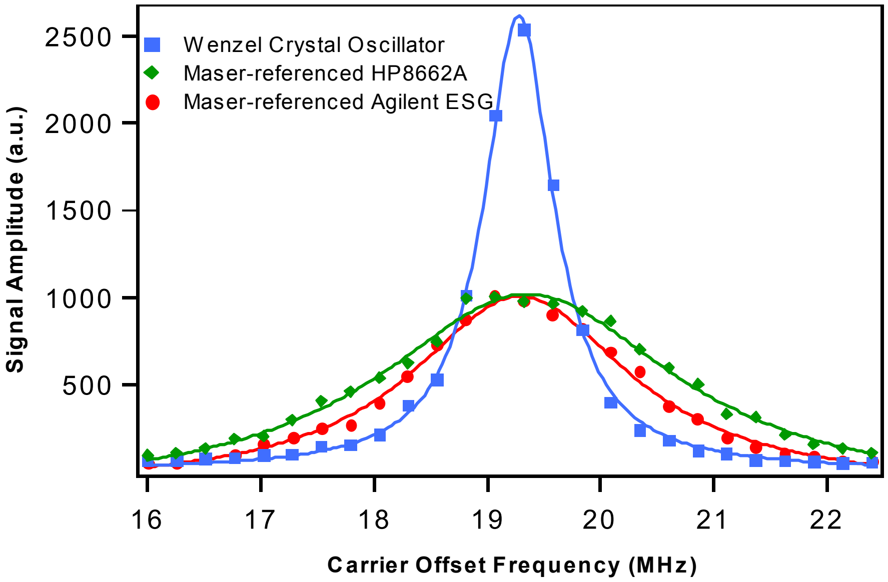

Figure 4.7: Comparison among two-photon lineshapes obtained with different rf references for the f_r lock, showing the importance of having a reference with good short-term stability.

At a later time, we phase-locked one comb line near 1064 nm (282 THz) to a Nd:YAG laser that was stabilized to molecular iodine. Although the short-term stability of the I_2-stabilized Nd:YAG is an order of magnitude better than that of the Wenzel oscillator, we did not observe any improvement in the two-photon resonance linewidth. We suspect that we are limited by the bandwidth of the PZT used for the f_r lock. This is a technical limitation, and in principle it can be overcome by improving the actuator bandwidth or by using pump-power control. Also, note that the I_2 system has a fast linewidth of ~ 5 kHz (i.e. fractional instability of 1.8×10^{-11}), which at longer timescales falls down as the square root of the averaging time.

4.4.2 Mechanical action of the probe

I will now discuss an important systematic effect, arising from the mechanical action of the femtosecond probe on the atoms. Although the sub-Doppler temperature established by polarization-gradient cooling provides an ideal initial condition for spectroscopy, it cannot be expected to survive the momentum transferred by the light from the comb. At best, the mean-square momentum will increase, leading to Doppler broadening. Worse, the momentum acquired may lead to systematic shifts in the resonance line positions. Thus, we seek to understand momentum transfer from the comb and to mitigate its effects insofar as possible.

We expect that the momentum transfer is dominated by the interaction of the comb mode closest to resonance with the 5S-5P transition, given that the radiative decay rate of the 5P-5S transition is an order of magnitude greater than that of 5D-5P, and the population largely resides in the 5S state.

For ease of modeling, we use a single-beam (traveling wave) configuration and choose a comb structure such that the closed $5S_{1/2}$ (F = 2) $\rightarrow$ $5P_{3/2}$ (F$'$ = 3) $\rightarrow$ $5D_{5/2}$ (F$''$ = 4) transition is dominant (see Fig. 4.8). The temporal signal evolution is shown in Fig. 4.9 for the initial detunings of $\delta_{SP} = 0$ (red curve), $\delta_{SP} = 1$ MHz (green curve),

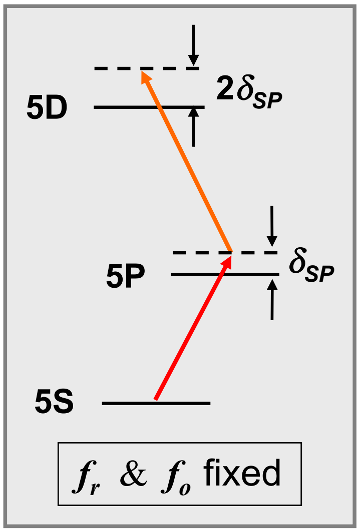

Figure 4.8: Schematic of the detunings from the intermediate and excited states relevant for the radiation pressure studies. f_r and f_0 are kept constant for these experiments, and the temporal signal evolution is monitored for different blue detunings.

and $\delta_{SP} = 2$ MHz (blue curve).

In the fully resonant case (red curve), the delayed signal peak at 30 μs reflects the switching time of our liquid crystal shutter. The subsequent decay arises as the accumulated momentum transfer gradually blue-shifts the atoms out of two-photon resonance.

Although the 5S-5P transition controls the mechanical action, the two-photon resonance condition plays a more decisive role in the observed signal decay due to the 10-times-narrower D-state linewidth. When $\delta_{SP} = 1$ MHz (green curve), the atoms, initially with $\delta_{SD} = 2$ MHz, will only reach the peak of the two-photon resonance after they have reached the velocity at which the Doppler shift compensates the initial detuning. Beyond this velocity, the signal contribution decreases. Similarly, when $\delta_{SP} = 2$ MHz (blue curve), the signal peaks still later.

The next section shows that all three experimental results agree well with our theory based on a simple two-level dissipative light force model. The peak position is

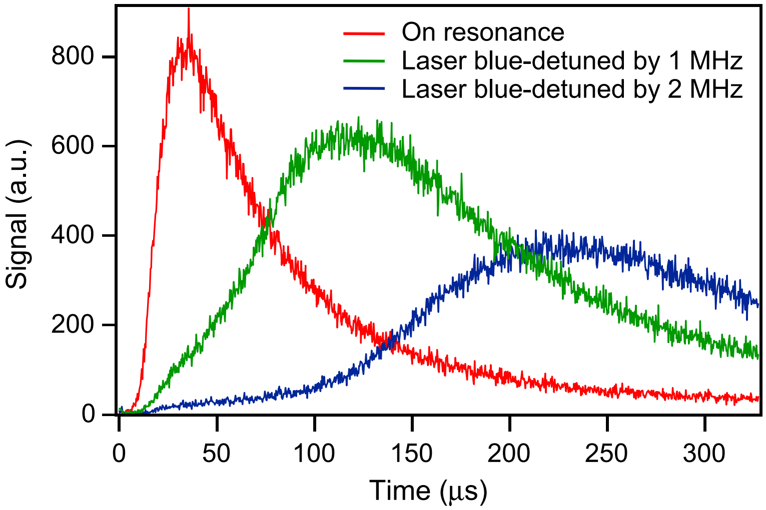

Figure 4.9: Momentum transferred by the optical frequency comb (in a single probe beam configuration) to the cold ^{87}Rb atoms, observed via the time-dependent fluorescence signal from the 5D states. The optical comb has fixed values of f_r and f_0 to achieve the desired detunings (with respect to atoms initially at rest) of $\delta_{SP} = 0$, $\delta_{SD} = 0$ (red curve); $\delta_{SP} = 1$ MHz, $\delta_{SD} = 2$ MHz (green curve); and $\delta_{SP} = 2$ MHz, $\delta_{SD} = 4$ MHz (blue curve), respectively, for the dominant pair of comb modes.

determined by the scattering rate, photon recoil, and the initial detunings. The width and shape of the peak are associated with the stochastic nature of radiation pressure, the intensity variation over the radial beam profile, and the finite laser linewidth.

4.4.2.1 Momentum transfer model

To understand the momentum transferred by the light from the frequency comb to the atoms we used single-beam (traveling wave) excitation for the experiment.

In this case, the net force on the atoms is

$$F = \hbar k \, \frac{\Gamma}{2} \frac{s}{1 + s + [2\,(\delta + \omega_D)/\Gamma\,]^2}\,, \tag{4.1}$$

where s is the saturation parameter i.e. the ratio of the light intensity I to the saturation intensity I_s. For the case of linear polarization in ^{87}Rb $I_s = 2.5$ mW/cm^2. The detuning of the laser from resonance is $\delta = \omega_l - \omega_a$, where ω_l is the laser frequency and ω_a is the atomic resonance frequency. The Doppler shift seen by the moving atoms is $\omega_D = -\mathbf{k}\cdot\mathbf{v}$.

We can see from this equation that for a maximum scattering rate, i.e. at the peak of the resonance, the Doppler-shifted laser frequency in the moving atoms' reference frame should match the atomic resonance frequency. In other words, for a given initial laser detuning from resonance, the atoms will accelerate until they reach a threshold velocity, at which point the peak of the resonance is attained (the threshold velocity occurs when the Doppler shift has compensated the chosen detuning).

For a constant intensity the above equation is easily separated and integrated, giving:

$$\int_{v_0}^{v} dv \left(1 + s + \left[\frac{4\pi}{\Gamma}\left(\delta - \frac{v}{\lambda}\right)\right]^2\right) = v_r \, \frac{\Gamma}{2} \, s \, t \tag{4.2}$$

with $v_r = \frac{\hbar k}{m}$ the recoil velocity of the atom. The right-hand side of this equation becomes upon integration a cubic function of v, from which we can obtain an expression for $v(t)$ by comparing against the left-hand side. In reality, though, the intensity depends on both the beam radial coordinate and time. The time dependence of the intensity is determined by our liquid crystal shutter response and has been well characterized. Taking it into account, along with the correct scattering rate, photon recoil and initial detunings gives a relatively good agreement with the experimental data, as far as the peak position is concerned, as presented in Fig. 4.10.

The width and shape of the peaks do not agree with the experiment yet. For a more realistic model, we have to consider and include the intensity variation with the beam radial coordinate; for a Gaussian spatial profile of the laser beam the intensity is given by

$$I(r) = I_0 \, \exp\left[-2\,\frac{r^2}{w_0^2}\right], \tag{4.3}$$

where I_0 is the on-axis intensity (~ 0.8 mW/cm^2) and w_0 is the beam waist ($\sim 130\mu$m).

It is easy to show that $\sim 90\%$ of the signal originates from within a radius of 100 μm. Actually, most of the signal comes from a radius of about 50 μm, as seen in Fig. 4.11.

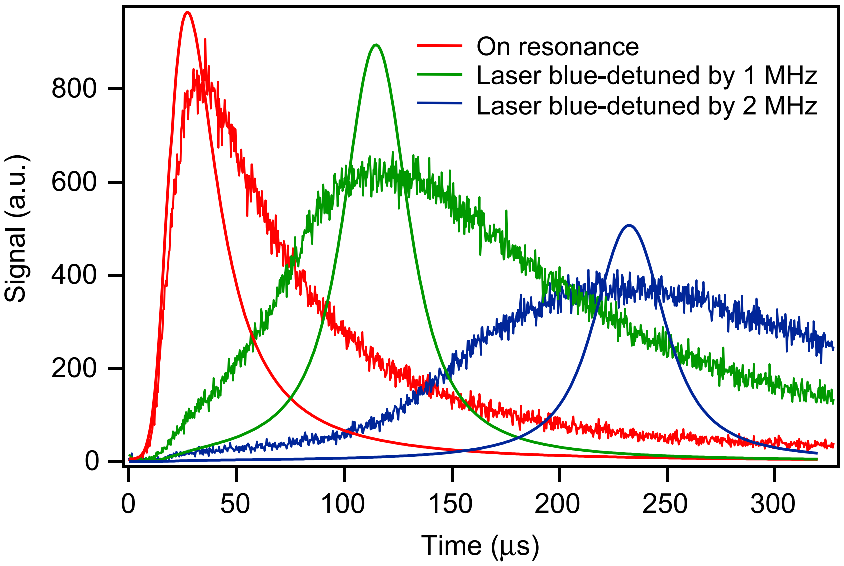

Figure 4.10: Momentum transferred by the frequency comb to the atoms. A comparison between the experiment and the simplified theoretical model, which assumes a uniform probing laser intensity.

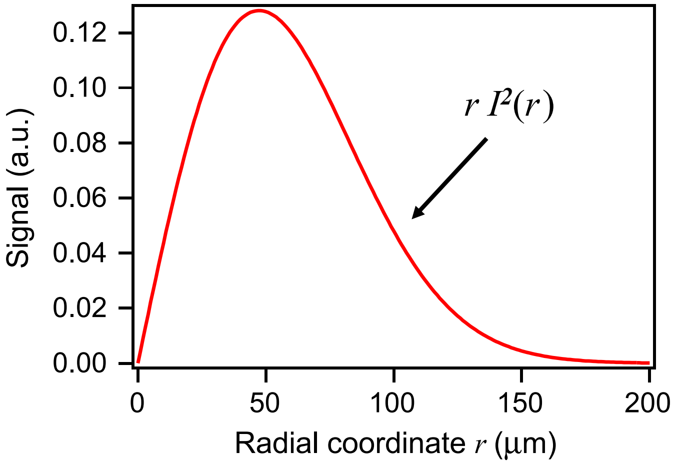

Figure 4.11: Two-photon signal vs. radial coordinate r for a Gaussian probe beam profile.

Including the r dependence, as well as a dependence on the laser linewidth ($\sim$ 330 kHz) gives a reasonable agreement between data and theory (solid lines in Fig. 4.12), as illustrated in Fig. 4.12. The dependence on the laser linewidth is introduced in the simulation via a random change of detuning for each iteration, governed by a Gaussian distribution centered at zero with a variance equal to the linewidth.

It is evident that the force exerted on an atom by the optical comb is well modeled by the radiation pressure due to a single comb mode tuned close to the 5S-5P resonance.

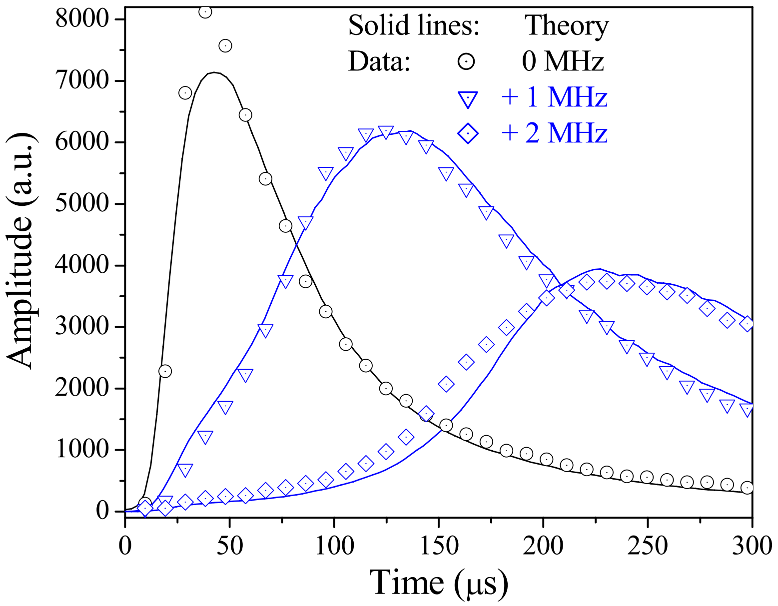

Figure 4.12: Momentum transferred by the frequency comb to the atoms. A comparison between the experiment and the more complete theoretical model, which includes integration over the radial probe beam profile and takes into account the laser linewidth.

As a first step in mitigating the effect of light-induced momentum transfer, we use intensity-balanced counterpropagating beams generated by splitting the pulse with a beamsplitter. We have arranged the setup to establish this counterpropagating beam geometry so as to have the focused beams spatially overlapped at the MOT. Once the setup is well aligned, the beams reflected from the beamsplitter back toward the laser cavity can disrupt the mode-locking process. Therefore, we employ an optical isolator to prevent feedback to the laser. As mentioned earlier, the spatial positioning of the interrogating beams is maintained with feedback control to an actuator on a mirror.

We have made no significant efforts to have the pulses overlap temporally inside

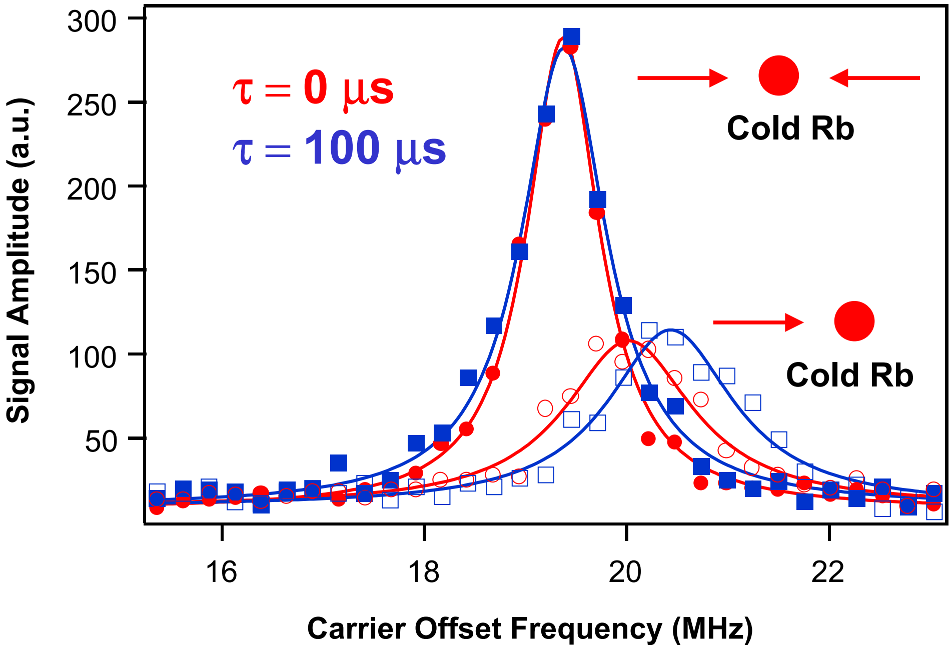

Figure 4.13: Shown here is the narrowing of the lineshape due to the counterpropagating-beam arrangement which counteracts the mechanical action of the probe. In addition, in the two-beam case, the line center shift is significantly reduced and the signal is enhanced by a factor of three compared to the single-beam case.

the atomic cloud (the pulse spatial extent is about 10 μm and the beam diameter at the MOT is about 300 μm). Nonetheless, the pulses do interact with the same group of atoms within the atomic coherence time, leading to signal enhancement by a factor of $\sim$ 3 compared to the single-beam case. We would expect a factor of 4, resulting from the same quadratic signal scaling presented in section 2.3. We suspect that the difference between our actual and expected enhancement is the result of both a slight intensity imbalance between the beams and the presence of a small angle between the fs and the coplanar (‘east-west’) MOT beam.

In addition to increasing the signal size when using a counterpropagating-beam configuration, the line center shift versus time is significantly reduced for this case compared to the single-beam case, as clearly shown in Fig. 4.13.

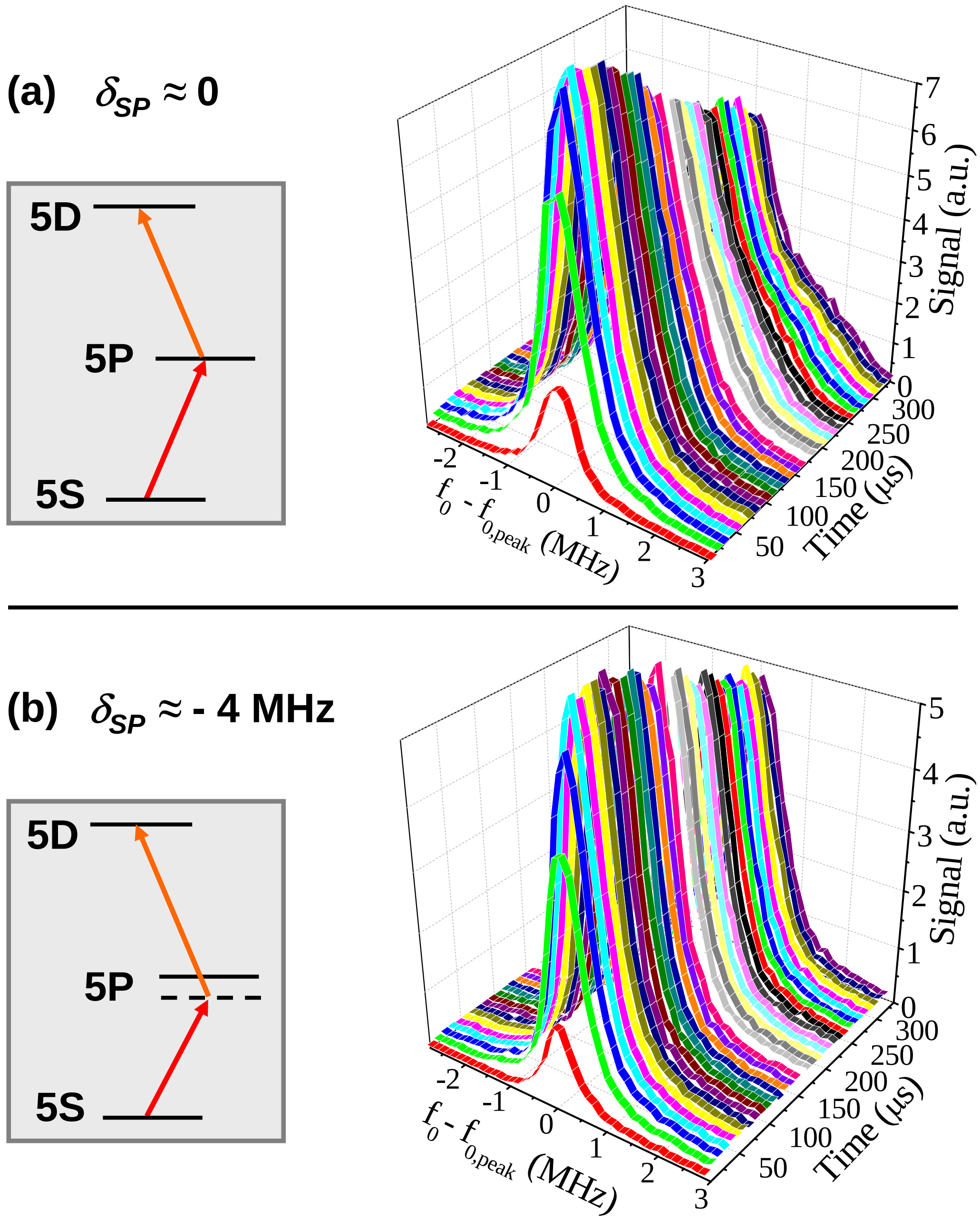

Figure 4.14: Time evolution of the 5D fluorescence signal lineshape showing the mechanical action of the optical comb for the case of two balanced counterpropagating probe beams. f_r is fixed while f_0 is scanned over the 5D resonance profile for two cases of P-state detuning, (a) $\delta_{SP} \approx 0$ and (b) $\delta_{SP} = -4$ MHz. For (a) there is a clear asymmetry in the two-photon lineshape at longer probing times, as detailed in Fig. 4.15. In contrast, for (b), the lineshape remains symmetric even after 300 μs of probing.

We continue to study the momentum transfer associated with the $5S_{1/2}$ (F = 2) → $5P_{3/2}$ (F′ = 3) → $5D_{5/2}$ (F″ = 4) transition, fixing f_r and scanning f_0. Figure 4.14, (a) and (b), show time evolutions of the detected signal as f_0 is swept, for two different detuning conditions: $\delta_{SP} = 0$ in Fig. 4.14(a) and $\delta_{SP} = -4$ MHz in Fig. 4.14(b), when f_0 is tuned to the two-photon resonance peak. As f_0 is scanned to recover the resonance lineshape, the value of δ_{SP} changes.

It is clear that the directed momentum transfer seen in Fig. 4.12 is greatly suppressed, and the heating is more evident. For the case of $\delta_{SP} \approx 0$, the lineshape profile centered at 300 μs (Fig. 4.15, black circles) shows a marked asymmetry. This feature is easily understood, because the comb lines are tuned blue relative to both the 5S-5P and 5S-5D resonances, although the detuning of the 5S-5P transition is less dramatic because its linewidth is an order of magnitude larger. Thus, Doppler heating accompanies the probe of the blue side of the two-photon resonance.

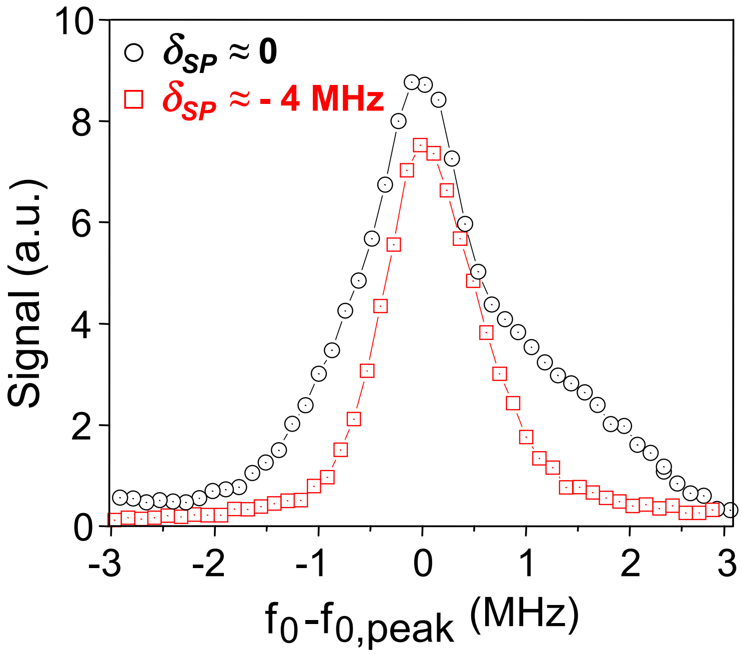

Figure 4.15: A detailed comparison of the lineshape under two detuning conditions after an interaction time of 300 μs.

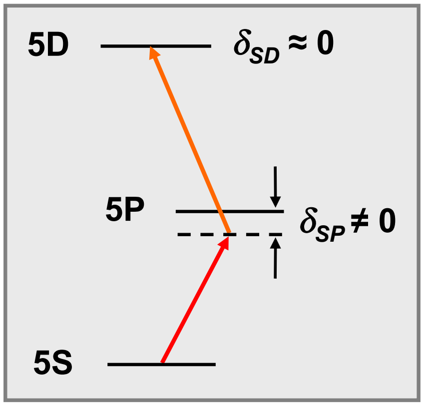

Figure 4.16: Schematic of the detunings from the intermediate and excited states relevant for the Stark-shifted data. f_r and f_0 are chosen such that the 5D state is always on resonance, while the detuning from the intermediate 5P state of interest is varied.

For the case of $\delta_{SP} \approx -4$ MHz, the intermediate-state detuning is always red as the two-photon resonance is probed. The red-detuned comb mode helps to maintain a symmetric absorption lineshape even after 300 μs, as confirmed by the corresponding profile (Fig. 4.15, red squares). Thus, a judicious choice of comb structure can help to mitigate the heating of the sample caused by the probing beam. From Fig. 4.14, (a) and (b), we also observe quite different signal decay rates versus observation time.

4.4.3 AC Stark shift and power broadening

Another systematic source of error is the light-induced AC-Stark shift on various atomic states to be measured. To assess this effect in the presence of many comb modes, we again take advantage of the flexibility in control of f_r and f_0 to vary δ_{SP} while keeping δ_{SD} nearly zero for the closed transition (see Fig. 4.16). In this near-resonance stepwise transition case, a non-vanishing value of δ_{SP} causes a shift in the measured two-photon transition frequency. Atomic energy shifts occurring in a resonantly enhanced two-photon process were first observed by Liao and Bjorkholm in Na vapor [74].

To clearly distinguish the AC Stark shift from mechanical actions, we gradually

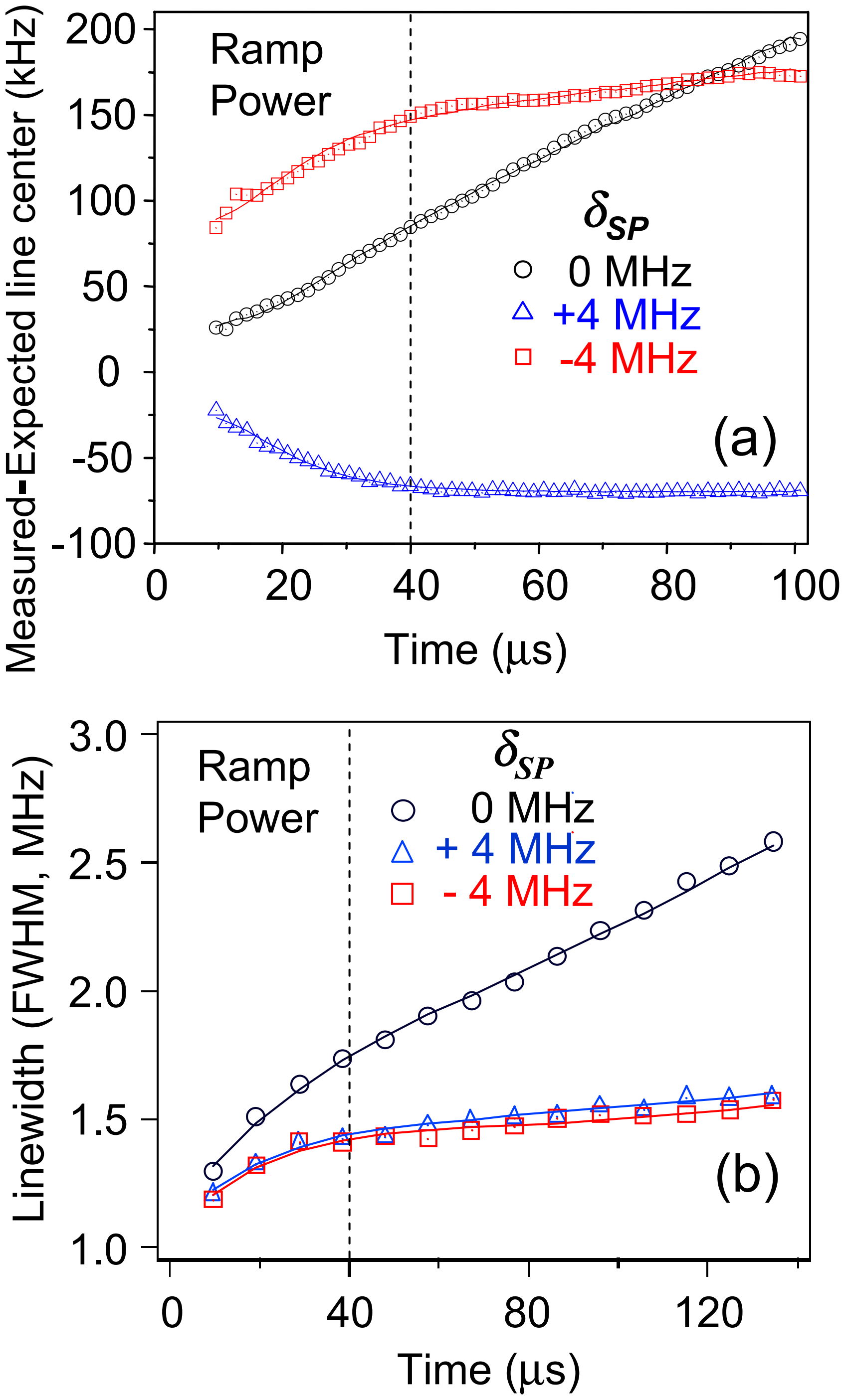

Figure 4.17: Measurement of (a) the line center frequency and (b) linewidth for the closed two-photon transition, revealing frequency shifts from both the AC Stark effect and mechanical action. Extrapolating to zero interrogation time and zero power yields the corrected atomic transition frequencies (a) and the natural transition linewidths (b).

increased the power of the pulses as the laser shutter opened. For both $\delta_{SP} = +4$ MHz (blue triangles) and $\delta_{SP} = -4$ MHz (red squares) cases, the AC Stark shifts are present as soon as the laser is turned on and the transition frequency shift follows the time evolution of the peak power of the pulse train [Fig. 4.17(a)]. When $\delta_{SP} = 0$ MHz (black circles), the measured AC Stark shift is close to zero when the shutter just opens. The frequency shift measured at later times is attributed to the accumulated photon momentum transfer, which is reduced in the detuned cases. The asymmetry in frequency shift between the red and blue detunings is caused by the presence of other 5P hyperfine states that also perturb the 5S-5D transition.

Although the laser spectrum spans roughly 26 THz, the obtained spectroscopic resolution approaches the atomic natural linewidth. This level of resolution is a result of the use of ultracold atoms and careful control of the phase-stabilized comb parameters, stray magnetic fields, light-induced shifts, and photon-momentum transfer. We typically measure two-photon linewidths on the order of 1 MHz [Fig. 4.17(b)], which is roughly consistent with the convolution of the natural linewidth of 660 kHz and the laser technical linewidth of 300 kHz. (Note that the laser linewidth is 600 kHz for a two-photon transition.) The measured transition linewidth is slightly smaller for red detuning ($\delta_{SP} = -4$ MHz) than blue detuning (at the same δ_{SP} value) with the same probe power.

4.4.4 Nulling stray magnetic fields

A direct consequence of the previous two sections is that for all the spectroscopy experiment, the line-center values are extrapolated to zero interrogation time to suppress shifts associated with photon-momentum transfer and the transitions are probed on optimal resonance (i.e., zero detuning for both the intermediate state and the final state) to minimize the AC Stark shifts.

Additionally, stray magnetic fields are minimized by applying bias-coil compensation in three orthogonal directions. To null the residual magnetic fields we make use of the two-photon signal itself: Zeeman-shifted spectra are obtained with right and left circularly polarized femtosecond comb light along each direction and the zero-frequency shift point is determined within ± 20 kHz, as presented in Fig. 4.18.

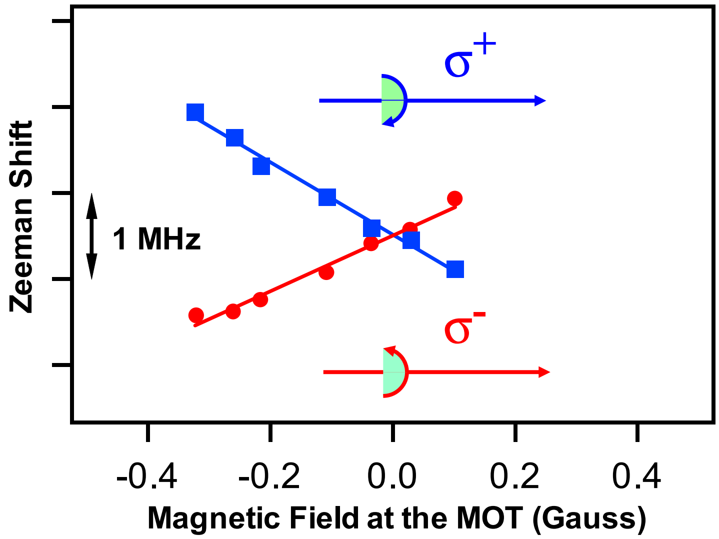

Figure 4.18: The two-photon fluorescence signal is used to cancel the residual magnetic fields: Zeeman-shifted spectra are obtained with right and left circularly polarized femtosecond comb light and the zero-frequency shift point is determined.

4.5 Conclusion

Because the use of the femtosecond comb is novel as a direct spectroscopic probe, in this chapter we carefully characterized several prominent systematic effects. Indeed, the dominant effects are the mechanical action of the optical comb on the atomic motion, the light shift induced by the probe laser, and the Zeeman frequency shifts. Now that we have isolated the biggest contributions to the systematic line center shift and linewidth we can actually do precision spectroscopy! In fact, the bandwidth associated with the femtosecond pulse is sufficiently broad so that many fine and hyperfine atomic states can be excited by tuning the relevant comb components into resonance.

Chapter 5

Two-photon absolute frequency measurements

One desirable objective in atomic spectroscopy is the ability to obtain a global energy level picture of the atomic transitions. In fact, the stabilized comb has tremendous possibilities for mapping numerous transitions in a straightforward way. In this chapter, I will show that it is possible to obtain all of the allowed single- and two-photon transitions within the laser bandwidth by a quick scan of f_r (~ 26 Hz). This scanning method is efficient and eliminates the need for broadly tunable and absolutely referenced cw lasers. This is one of the main advantages of using a frequency comb directly for spectroscopy.

Previously, in Chapter 4, we scanned f_0 and kept f_r locked in order to characterize the primary contributions to systematic effects on both the line center and the linewidth. When these results are integrated into the the setup we have a system which can perform precision mesurements. In this chapter, I focus on some representative 5S-5D transitions for precision spectroscopy. Indeed, the measurement results approach the accuracy of those obtained in the best cw measurements to date.

Also, if we consider that we have locked the Ti:S comb to a commercial cesium clock and thus have generated an absolutely referenced set of optical frequencies, we can use these frequencies for identification of previously unmeasured transitions. As an example, we determine the previously unmeasured absolute frequency of the 5S-7S two-photon resonances. We thus demonstrate that prior knowledge of atomic transition frequencies is not essential for this technique to work, and indicate that it can be applied in a broad context.

5.1 Scanning f_r gives a full spectrum

In general, sweeping f_r has the advantage of yielding all the transitions within the laser bandwidth in only a ~ 26 Hz scan. This is due to the fact that the ratio of one-photon optical transition frequencies (participating in stepwise two-photon transitions) to f_r is $\sim 3.8 \times 10^6$, so that for a change in f_r of ~ 26 Hz the resonant enhancement is repeated by the next neighboring comb component.

However, the optical frequency for the two-photon transitions is ~ 770 THz, an f_r harmonic on the order of 7.7×10^6. Therefore, the two-photon resonance condition is satisfied every time f_r is changed by ~ 13 Hz, corresponding to a change in the comb frequency by $f_r\ /2$ for the mode orders around 3.85×10^6.

As an aside, I will discuss the two primary differences between scanning f_r and scanning f_0: (i) simply stated, f_r has the advantage of being multiplied by N, whereas f_0 does not and (ii) scanning f_r can easily tune over 100 MHz in the optical region, whereas scanning f_0 in the current configuration produces a 80 MHz sweep at the maximum. The trouble with scanning f_0 is that the beat can reside anywhere between 0 MHz and $f_r/2$ (there is of course a conjugate beat in the $f_r/2$ to f_r window) but, in order for us to lock f_0, we are restricted to the 7-47 MHz range. Thus, to obtain broader tunability in the current experimental configuration, we scan f_0 up to 47 MHz, then change the sign within the servo to acquire lock on the conjugate beat and finally, we proceed to scan this conjugate beat up to -47 MHz. This gives a total tuning of 80 MHz. (Note that we can adapt the current setup, for example by including acousto-optic modulators in the ν-to-2ν interferometer, to obtain continuous tuning without having to change the servo sign.)

Figure 5.1 presents the two-photon transition spectrum obtained by scanning

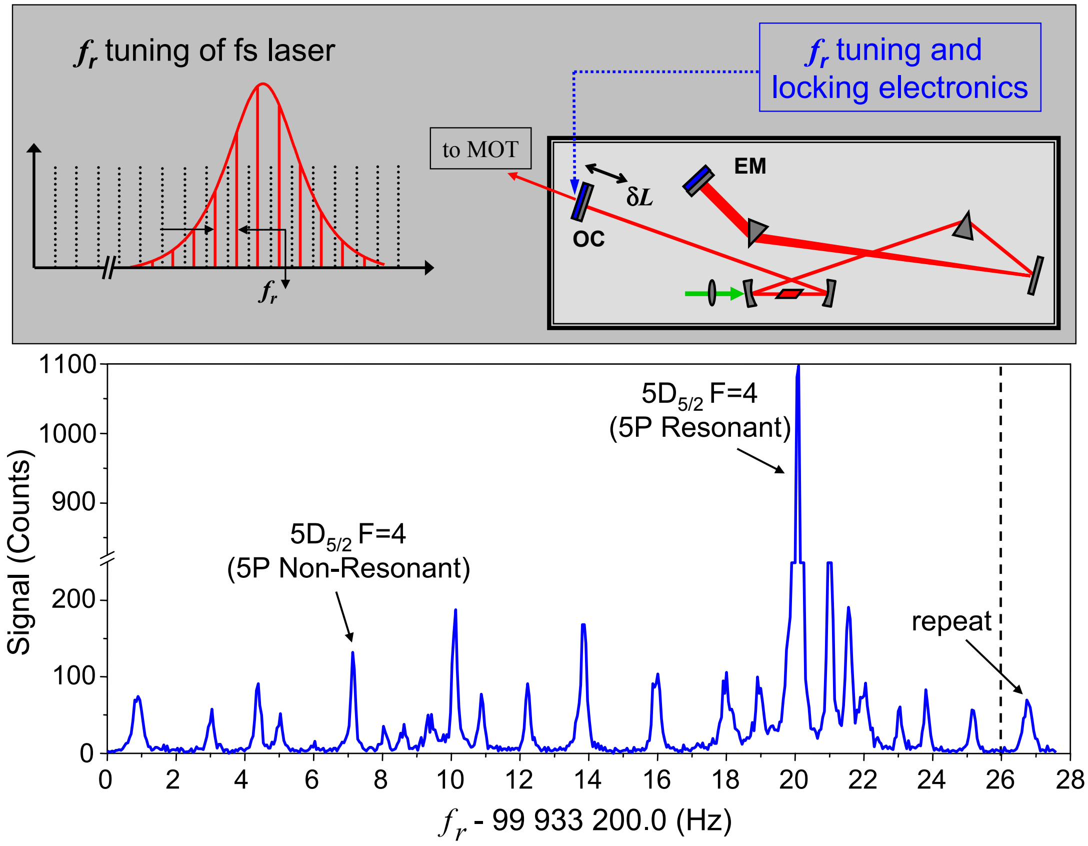

Figure 5.1: The top panel shows the experimental setup for scanning the laser repetition frequency f_r and the lower one presents the two-photon spectrum obtained from such a scan. All possible 5S-5D transitions are observed; this includes the non-resonant and resonantly enhanced transitions.

f_r for a fixed value of f_0. It shows the 14 transitions (there are 39 possible pathways for the case of linearly polarized light) that I identified for the $5S_{1/2} \rightarrow 5D_{3/2}$ and $5S_{1/2} \rightarrow 5D_{5/2}$ two-photon resonances. The data clearly show that the larger, one-photon resonantly enhanced peaks repeat after a change of f_r by ~ 26 Hz, as expected from the simple calculation above. As mentioned in section 4.2, for the resonantly enhanced peaks, the pair of comb modes that is actually tuned onto the 5S-5P and 5P-5D resonances makes the dominant contribution to the two-photon transition rate.

In Fig. 5.2, we also present the theoretical spectrum corresponding to the set of parameters used in the experiment. The two insets show signal magnitude on a logarithmic scale to enhance the visibility of the smaller peaks. The peak corresponding to non-resonant excitation of the $5S_{1/2}$ $(F = 2) \rightarrow 5P_{3/2}$ $(F'=3) \rightarrow 5D_{5/2}$ $(F''=4)$ transition, made possible by the collective action of many comb modes, is larger than that theoretically predicted because the comb spectral phase is not flat and the comb spectrum is not symmetric around the P state; thus, the destructive interference mentioned earlier in section 4.2 is reduced. Furthermore, as the detuning from the P state becomes greater than a few THz, the effect of phase mismatching between comb pairs over the spatial dimension of the MOT can be non-negligible.

There are a couple of interesting spectral features that we notice when looking at Fig. 5.2. The two resonance peaks observed in the experimental spectrum, which are not present in the theory model, are due to the $5S_{1/2} \rightarrow 7S_{1/2}$ two-photon transitions. Their observation prompted us to consider both their theoretical modeling and experimental investigation. However, it is more complicated to include these transitions in the model than to include the 5S-5D two-photon transitions, primarily because their frequency has never been measured before. In fact, this led us to actually experimentally measure their absolute frequencies, as presented in section 5.3. I had not initially intended to study them, though this shows again one of the powerful features of our direct frequency comb technique, the fact that we can observe all the transitions within the fs laser bandwidth.

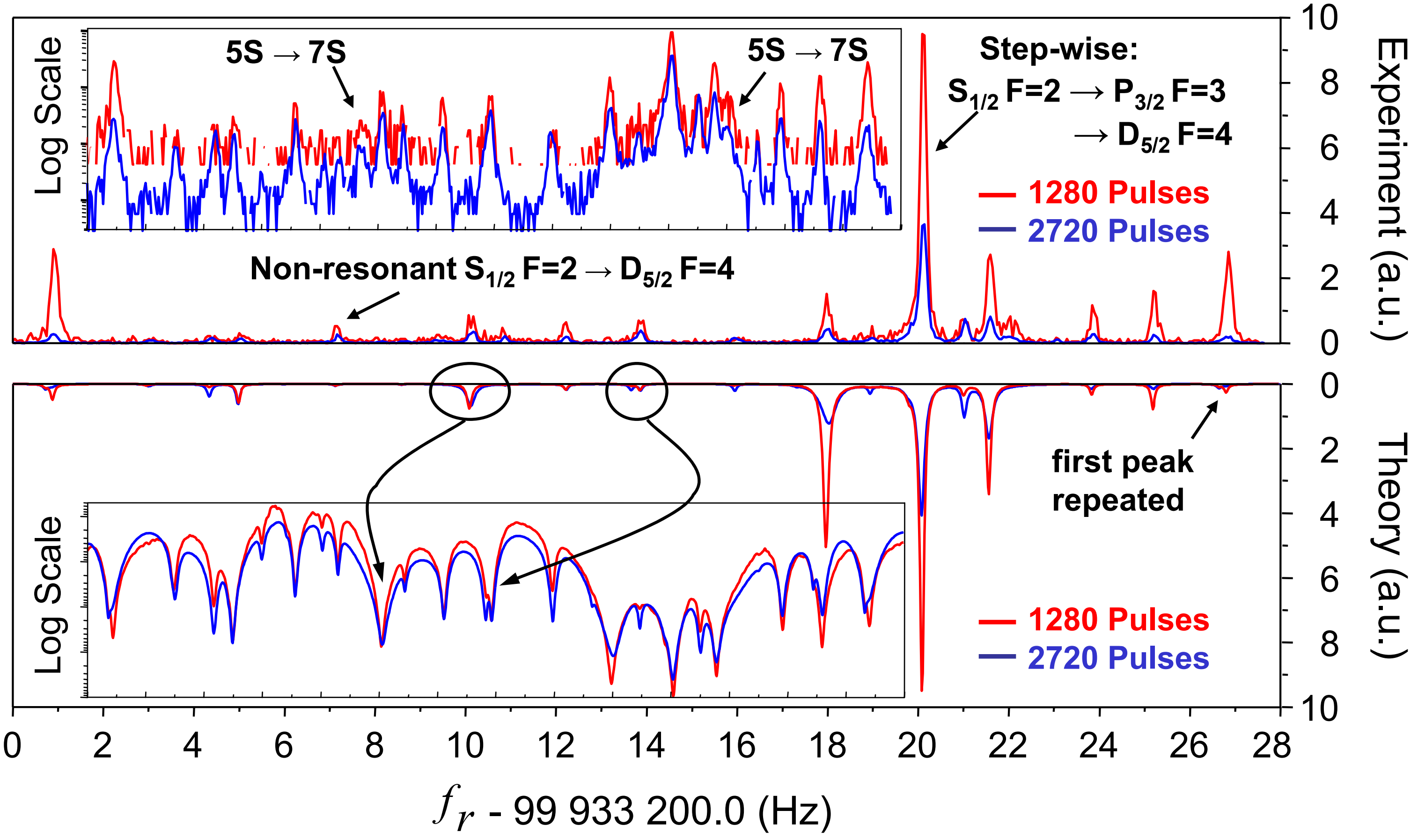

Figure 5.2: Experimental (top) and simulated (bottom) two-photon spectra obtained with a frequency scan of f_r. Shifting f_r by 26 Hz shifts the comb spectrum by 100 MHz, or f_r, approximately repeating the original comb structure. The changes in relative peak sizes from the spectrum obtained after 1280 pulses (in red) to that after 2720 pulses (in blue) illustrate population transfer dynamics by optical pumping as well as heating effects. Two resonances in the data due to the 5S → 7S transitions are not included in our model.

For this f_r scan, the initial ground-state population is in F=2. At longer times (blue curves), all the transitions starting on F=2 are decreasing in amplitude compared to shorter time scales (red curves) due to ground-state population redistribution and heating. Most of the F=1 peaks remain unchanged or become larger. Our density matrix simulation accounts for the time dependence of the shutter response and optical pumping dynamics, but does not include any heating effects. The signal size shown in Fig. 5.2 has been normalized against the square of the probe power. Not surprisingly, both theory and experiment reveal that the most dominant transition pathway is the closed $5S_{1/2}$ (F=2)→ $5P_{3/2}$ (F$'$=3) → $5D_{5/2}$ (F$''$=4) transition.

The relative size of the features in Fig. 5.2 after any fixed number of pulses reflects intermediate-state resonant enhancement as well as population transfer. Thus, the spectrum contains all of the fine and hyperfine structure pertinent to the 5D states.

5.2 Absolute frequency measurements

After accounting for the systematics discussed in Chapter 4, we have analyzed spectra similar to the ones shown in Fig. 5.2 to construct a table of absolute transition frequencies from 5S to 5D (see Table 5.1). We isolated the five two-photon transitions which start in F=2, and go through $5P_{3/2}$ F$'$=3, i.e. two-photon transitions which have the 5S-5P step as a closed transition. This closed first step may help with the optical pumping, giving better signal-to-noise ratios to determine their absolute frequency.

These representative transition frequencies are determined directly from the comb structure and are given in the table, along with comparisons to available published values [75]. The measurement accuracy is currently a few kHz to a few tens of kHz for the 5D states and on the order of 100 kHz for the 5P states, comparable to the highest resolution measurements made with cw lasers. All the measurement errors reported here are statistical errors (one standard deviation of the mean).

Measured transition	Measured frequency (kHz)	Literature value (kHz)
$5S_{1/2}$ F=2→ $5D_{5/2}$ F″=2	770 569 184 527.9 (49.3)	770 569 184 510.4 (16.0)
$5S_{1/2}$ F=2→ $5D_{5/2}$ F″=3	770 569 161 560.5 (11.1)	770 569 161 555.6 (16.0)
$5S_{1/2}$ F=2→ $5D_{5/2}$ F″=4	770 569 132 748.8 (16.8)	770 569 132 732.6 (16.0)
$5S_{1/2}$ F=2→ $5D_{3/2}$ F″=3	770 480 275 633.7 (12.7)	770 480 275 607.6 (10.0)
$5S_{1/2}$ F=2→ $5D_{3/2}$ F″=2	770 480 231 393.9 (38.1)	770 480 231 385.2 (10.0)
$5S_{1/2}$ F=2→ $7S_{1/2}$ F″=2	788 794 768 921.4 (44.5)	788 794 768 878.0 (40.0)
$5S_{1/2}$ F=1→ $7S_{1/2}$ F″=1	788 800 964 199.3 (121.9)	788 800 964 042.0 (40.0)

Table 5.1: ^{87}Rb level structure from direct frequency comb spectroscopy. All the values are obtained by extrapolating the line center to zero probing time and power. The first six transitions presented here are resonantly enhanced by the $5P_{3/2}$ F′=3 state and thus have a closed first step. The final seventh transition passes through the $5P_{3/2}$ F′=1 intermediate level.

We will now move on to discuss the measurement of the two extra resonances that appeared in the spectra shown in Fig. 5.2.

5.3 5S-7S absolute frequency measurements

After observing the two resonances, we reviewed the literature and discovered that in fact no one had measured these transitions with high precision. Without *a priori* information of the 7S energy levels, we have determined their absolute transition frequencies [76]. We have used the transition wavelength reported in the online NIST atomic database, which was of course covered by the fs laser spectrum, so we were able to determine the resonance frequencies. A single optical comb thus provides atomic structural information in the optical, terahertz, and radio-frequency spectral domains.

I will discuss in some detail now the 5S-7S two-photon frequency measurements. They were performed in a similar manner to the 5S-5D measurements, with the important change that we used a Pockels cell with a 8-ns rise time instead of the liquid crystal shutter ($\sim 30\ \mu$s response time). As a consequence, we did not have to account for the shutter turn-on when obtaining the final frequency values, which made it easier to extrapolate to zero power. The experiment cycle and general method remained the same, especially since the 7S levels also decay through the 6P levels, which means that we were able to use the same PMT. As seen from the general frequency diagram in section 4.2, the wavelengths for the second step of the resonantly enhanced 5S-7S transitions are 741 nm for transitions via $5P_{3/2}$ and 728 nm for transitions via $5P_{1/2}$. The energy degenerate two-photon transition is at 760 nm. This makes it more difficult to cover them in our spectrum, optimized for 778 nm. This fact is especially true about 728 nm wavelength. Shifting the spectrum to smaller wavelengths is definitely doable, the problem is having a sufficient signal-to-noise ratio for the f_0 beat to properly maintain phase-lock of the Ti:S. The degradation in the signal-to-noise ratio of the f_0 beat occurs because the microstructure fiber is optimized for its zero GVD point near 800 nm. Thus, I usually center the fs spectrum at 770 nm for these measurements and I try to use only transitions enhanced by a $5P_{3/2}$ intermediate level.

Shown in Fig. 5.3(a) is a typical $7S_{1/2}$ F''=2 Lorentzian lineshape, generated by stepping the offset frequency f_0 for a fixed value of the repetition rate f_r and recording the subsequent blue fluorescence corresponding to the 7S population. For each data point, to obtain a better signal-to-noise ratio, the 80 ns-binned counts arising from the fluorescence are integrated over 2.4 μs. Alternatively, this lineshape is retrieved by sweeping f_r with f_0 fixed at some convenient value.

Once the lineshape has been acquired, what remains is to identify the correct mode number N associated with each transition. If the optical frequency is already known to within $f_r/2$, this is a straightforward task. For the case of the 5S-7S two-photon transitions, where the resonance frequencies are not known *a priori* ($\nu_{opt} = (N_1 + N_2)f_r + 2f_0$), we scan the resonances for two different values of f_r and unambiguously deduce the sum of the two associated integers $(N_1 + N_2)$ [77, 78]. In our case, the two repetition rates used are separated by 600 kHz to eliminate possible uncertainties arising from estimations of the f_0 value corresponding to the peak of the resonance.

After identifying the comb numbers associated with the transition and reducing

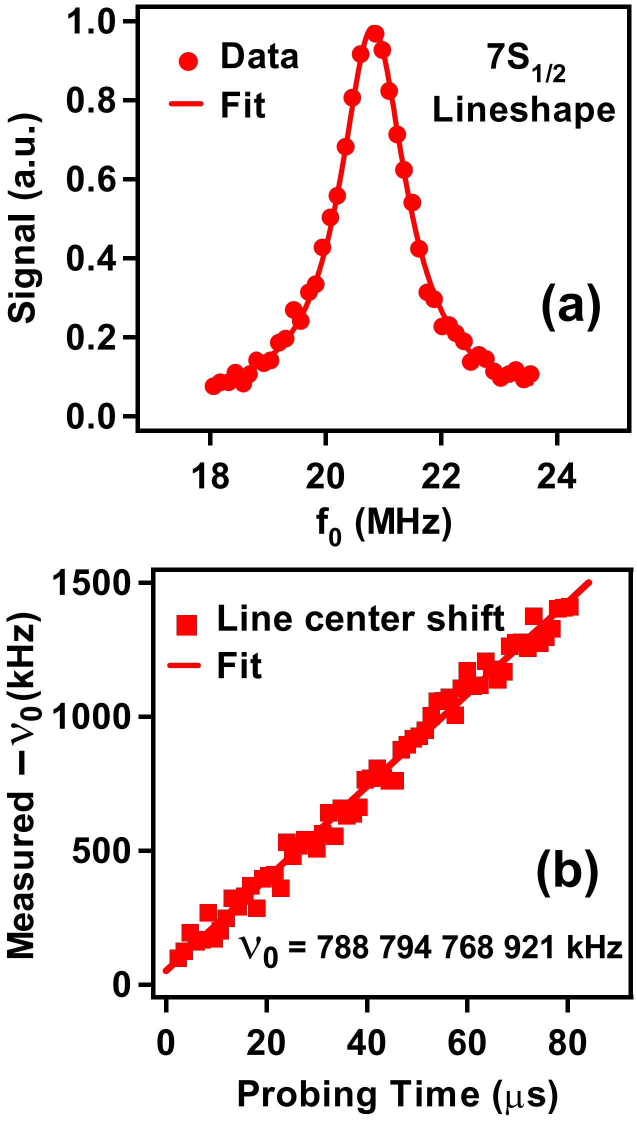

Figure 5.3: (a) Typical $5S_{1/2}$ F=2→ $7S_{1/2}$ F$''$=2 two-photon Lorentzian lineshape obtained from a scan of the offset frequency f_0 for a fixed value of the repetition rate f_r . For each data point, the 80 ns-binned counts arising from the fluorescence are integrated over 2.4 s. (b) Frequency shift of the transition line center vs. probing time resulting from the momentum transferred by the femtosecond laser to the cold ^{87}Rb atoms. Extrapolation to zero interrogation time gives absolute atomic transition frequencies, as well as roughly the natural linewidth, free of radiation pressure effects.

the systematic error arising from AC Stark shift (by probing on optimal resonance i.e., zero detuning for both the intermediate state and the final state), the remaining error from radiation pressure is suppressed by extrapolating to zero interrogation time, as shown in Fig. 5.3(b). We determine for the $5S_{1/2}$ F=2 → $7S_{1/2}$ F''=2 and the $5S_{1/2}$ F=1 → $7S_{1/2}$ F''=1 two-photon transitions in ^{87}Rb the absolute optical frequencies of 788 794 768 921(44) kHz and 788 800 964 199 (122) kHz, respectively (see Table 5.1). The excited state hyperfine interval of 639 404 (130) kHz agrees very well with a previous differential measurement performed with a picosecond pulsed laser [70]. The transition spectra reported in [70], as well as a continuous-wave (cw) laser-based scan [79], indicated that the F=2 → F''=2 and the F=1 → F''=1, i.e. ΔF=0 transitions, were the only allowed 5S-7S transitions in ^{87}Rb. However, we observe additional lines, as the resonant intermediate 5P state also enables the F=2 → F''=1 and F=1 → F''=2, i.e., ΔF=±1, two-photon transitions. Similar ΔF=±1 S-S transitions have been previously observed in Na in a two-step excitation experiment employing two tunable cw dye lasers, which enabled a direct measurement of the excited state hyperfine splitting [80].

We recently learned that conventional, cw laser-based measurements of the 5S-7S transitions in Rb were reported by Chui *et al.* [81]. Our measurements agree with their results, within one standard deviation of the mean for the reported values, as can be seen from Table 5.1. Thus, we have demonstrated that by using DFCS, the absolute value of the $5S_{1/2} \rightarrow 7S_{1/2}$ two-photon transitions in ^{87}Rb is conclusively determined, with no *a priori* knowledge about their optical frequency.

In the next chapter I will discuss single-photon frequency measurements that we recently made. As described there, one indirect way to determine the absolute frequencies of the 5S-5P transition is to scan the 5P state by using a set of f_r and f_0 pairs that have a range of detunings from the 5P state and are all two-photon resonant. I will show that detailed dynamics of population transfer driven by a sequence of pulses have to be taken into account for the measurement of the 5P states via resonantly enhanced two-photon transitions.

Chapter 6

One-photon absolute frequency measurements

Direct Frequency Comb Spectroscopy (DFCS) can be equally well applied to measure single-photon transitions. However, since we have the ability to dynamically access two-photon transitions (as shown in Chapter 4), we can measure the energy of a given state in two ways. We can either investigate an atomic state as part of a one-photon process or as a two-photon process. We have chosen the 5S-5P transitions in ^{87}Rb to demonstrate this ability. The measurement of 5P states has been carried out directly and also indirectly, via the 5S-5D two-photon transitions by studying their resonant enhancement when comb components are scanned through the intermediate 5P states. We compare the 5P measurements obtained via one-photon and two-photon DFCS and clearly demonstrate the importance of population transfer in working with multilevel systems probed by multiple comb components.

Also, again with the technique of DFCS, we have the advantage of being able to determine absolute atomic transition frequencies anywhere within the comb bandwidth, for one-photon processes.

6.1 Detection and timing scheme for the direct 5P measurements

For the one-photon studies we have investigated both the D_1 and D_2 transitions in ^{87}Rb, namely transitions from the ground state to the 5P$_{1/2}$ excited state at 795 nm and to the 5P$_{3/2}$ state at 780 nm (see general diagram, in section 4.2).

The three main timing sequences of the magneto-optical trap (MOT), the polarization gradient cooling (PGC), and the probing cycle are similar to those shown in section 4.3. However, here during the probing cycle, we implement a switching scheme for the photomultiplier tube (PMT) and the fs laser.

The main challenge with the direct 5P measurements is to collect the fluorescence emitted by the atoms, while avoiding gathering the light from the fs probe, since they have nearly the same wavelength. In addition, because we use acousto-optic modulators for fast switching of the MOT lasers, there is always some residual light that may affect the measurements. Care was taken to ensure that these lasers did not influence the signal.

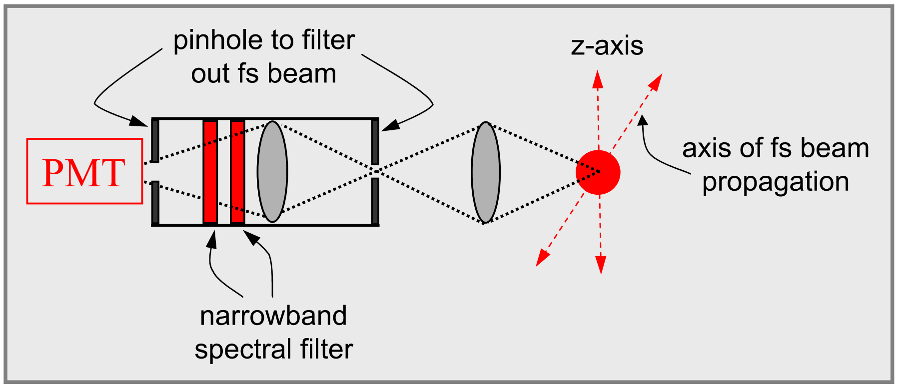

Figure 6.1: Detection assembly for the direct one-photon measurements. Background counts are minimized by using spatial and spectral filters. As before, the PMT signal is sent to a photon counter and the resulting counts are read into a computer.

We directly detect the fluorescence from the two 5P states with a near-infrared PMT coupled with a 3-nm bandwidth interference filter centered at the appropriate wavelength for the transition, as presented in the detection assembly in Fig. 6.1. We use narrow band interference filters reduce the number of comb components that are received by the PMT and thus minimize detection noise. Background counts are further minimized by spatial filtering with two pinholes, the first very small (1 mm), through which the MOT is imaged [Fig. 6.1]. Photon collection during the probe laser-on period is disabled by switching off the PMT.

The loading cycle used for the MOT is 100 Hz, and the sequence of the experiment is similar to the two-photon experiments [Fig. 6.2]: the atoms are loaded in the MOT for 7.8 ms, then the quadrupole magnetic field for the trap is switched off, the atoms are cooled with polarization gradients for 2 ms, then all the MOT beams are extinguished and the femtosecond comb beam is switched on for 200 μs using the Pockels cell (8-ns rise time)

As illustrated in the one-photon timing diagram in Fig. 6.2, during the 200 μs probe window, we have a sequence of short cycles with the probe laser on (200 ns) followed by the PMT on (400 ns) to detect photons from the fast-decaying 5P states. A 2.6 μs interval (PMT switch-off time) is required before initiating the next laser cycle. Both the two-photon and the single-photon signals are averaged over hundreds of 10 ms experiment cycles.

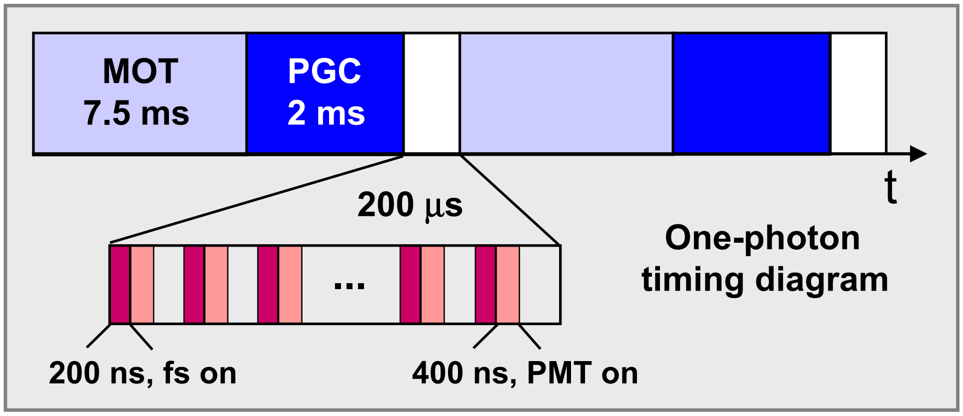

Figure 6.2: Timing scheme for the 100 Hz experiment cycle, where the 200-μs zoom window shows the sequences for the direct one-photon measurements. We switch the PMT off during the laser-on period, to minimize detection noise.

For the indirect 5P measurements, we use results from the theoretical model describing the fs comb interaction with the atoms. As discussed in Chapter 2, the theory accounts for detailed dynamics of population transfer among the atomic states involved in transitions within the comb bandwidth. A numerical scheme is employed to obtain the state of the atomic system after an arbitrary number of pulses [37, 60]. This model is applied to accurately predict the coherent population accumulation in the relatively long-lived 5D, followed by incoherent optical pumping. Especially important for the indirect 5P measurements is the incoherent optical pumping to the ground state hyperfine levels, which depends critically on the 5P state detunings and will be discussed in detail below.

We will now compare one-photon and two-photon DFCS measurements for the 5P state energy levels. The one-photon DFCS employs radiative detection directly from the 5P states (Fig. 6.3, left panel), while the two-photon DFCS studies the 5P states indirectly, via resonant enhancement of the 5S-5D two-photon transitions as a function of the detuning from the intermediate 5P states (Fig. 6.3, right panel).

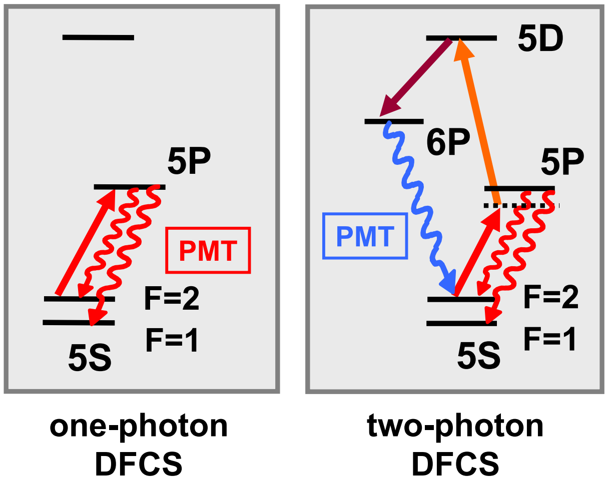

Figure 6.3: Schematic of one- and two-photon DFCS, used for measuring single-photon transition frequencies. The two-photon DFCS here differs from the two-photon process described in Chapter 5 in that the 5D state is kept strictly in resonance. The 5P lineshape is obtained by scanning the detuning.

6.2 $5P_{3/2}$ frequency measurements

First, we measure the $5S_{1/2}$ F=2 → $5P_{3/2}$ F′=3 D_2 transition with one-photon DFCS, with the resulting transition line shown in Fig. 6.4(a) [76]. Frequency scans are carried out similarly to those of the 5S-5D lines, that is, by stepping f_0 continuously while keeping f_r fixed. The absolute optical frequency measured for this transition is 384 228 115 271 (87) kHz, in agreement with a previous measurement done here at JILA [82], which resulted in an absolute frequency value of 384 228 115 203 (7) kHz. Once again, all the measurement errors reported in this chapter, and actually in this thesis, are statistical errors (one standard deviation of the mean).

For the two-photon DFCS, we use a set of different pairs of f_r and f_0 specifically chosen to have varying detunings from the 5P state for each data point shown in Fig. 6.4(b), while at the same time satisfying strictly the 5S-5D two-photon resonance ($\delta_{SD} = 0$). In this case, we monitor once again the 420 nm fluorescence from the 5D states. Such a set of f_r and f_0 is given as an example in Table 6.1. We immediately see that f_r must be known within 10 mHz. To obtain this level of accuracy, we always reference the f_r frequency counter to the cesium clock in our lab. As mentioned earlier, this is necessary because the f_r excursions get multiplied by $\sim 8 \times 10^6$. In contrast, f_0 must only be stable within 100 Hz.

The lineshape in Fig. 6.4(b) is retrieved by detecting the 420 nm signal as a function of 5P state detuning and the optical frequency measured by this two-photon DFCS is 384 228 115 309 (63) kHz, in agreement with the result obtained from one-photon DFCS within the standard deviation. Although the two methods for measuring this 5P state, direct and indirect, agree well, the indirect one is more cumbersome for two main reasons. Firstly, f_r must be changed by such a large amount as to require the output coupler to be placed on a translation stage and thus, the laser box to be opened for each detuning value. Secondly, this required hand-tuning adds significant

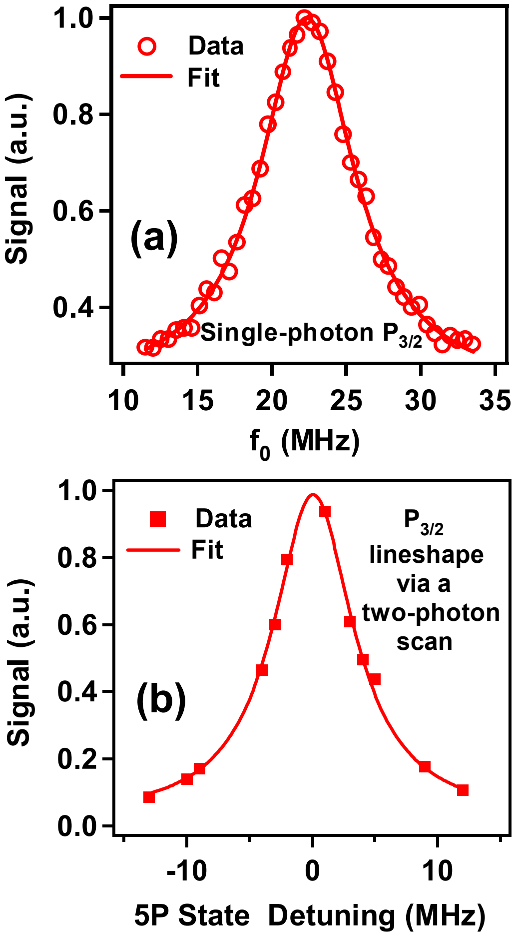

Figure 6.4: (a) Lineshape of the $5S_{1/2}$ F=2→ $5P_{3/2}$ F′=3 transition obtained from a scan of f_0 for a fixed value of f_r, by one-photon DFCS. (b) Same lineshape as in (a), retrieved using its resonant enhancement of the $5S_{1/2}$ F=2→ $5P_{3/2}$ F′=3→ $5D_{5/2}$ F″=4 closed two-photon transition, as a function of the detuning from the intermediate state.

time for retrieving a lineshape, so it is important that the data be taken under the same conditions and thus, it all has to be acquired on the same day. The direct method, though requiring an extra (switched) PMT, allows for a fast and smooth scan of the 5P states.

It is also important to mention that for this scan we take advantage of the $5S_{1/2}$ F=2 → $5P_{3/2}$ F′=3 → $5D_{5/2}$ F″=4 being the only 5S-5D closed transition. As shown in the theory plots in Fig. 6.5, this closed transition ensures that most of

5P detuning (MHz)	f_r (MHz)	f_0 (MHz)
-13	99.89260605	-16.4737
-10	99.92066423	-22.4503
-9	99.93474869	-16.2599
-4	99.92482030	-9.9189
-3	99.93890785	-11.1280
-2	99.91518350	-21.3653
+1	99.94325356	-24.2433
+3	99.86747878	-22.2673
+4	99.88155032	-24.0872
+5	99.89562280	-14.1944
+9	99.84803930	-11.4370
+12	99.84303590	-24.3973

Table 6.1: Example of a set of f_r and f_0 pairs used for the indirect scanning of the intermediate $5P_{3/2}$ F′=3 state. All the detunings are given with respect to this P state. The values for f_r and f_0 are chosen to ensure that the F″=4 state is always resonant for this indirect scan.

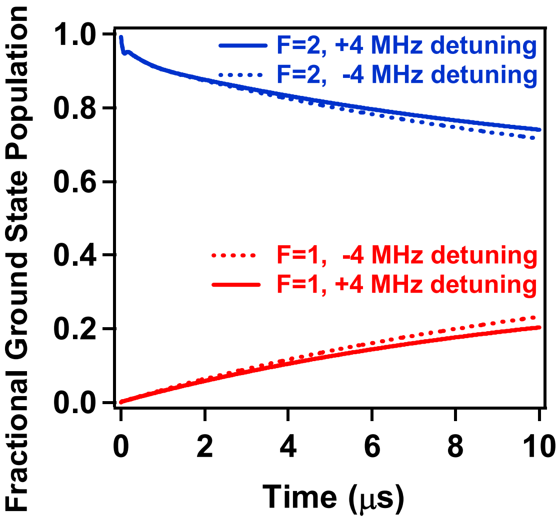

Figure 6.5: Theoretical plot of the time evolution of the ground state populations for two (symmetric) detuning values in Fig. 6.4(b), showing that (i) most of the atoms remain in the initial F=2 ground level for this closed two-photon transition and (ii) the ground state populations are largely insensitive to the sign of the detuning.

the atoms initially starting out in the F=2 ground-state hyperfine level remain in that level, while ∼20% of the atoms fall into the dark F=1 ground state due to optical pumping and hence do not contribute to the signal. In addition, the probe laser power is sufficiently reduced for the two-photon DFCS experiments to further decrease optical pumping effects.

6.3 $5P_{1/2}$ frequency measurements

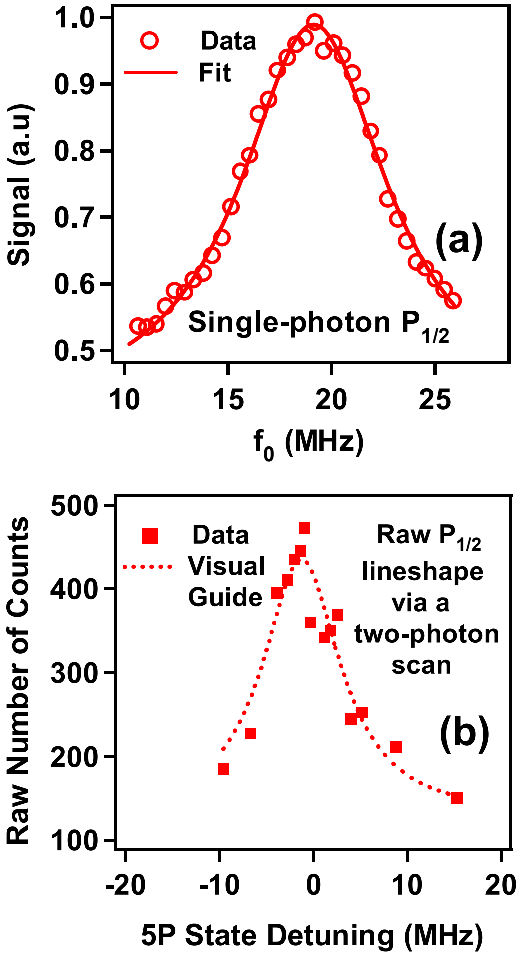

Figure 6.6: (a) Lineshape of the $5S_{1/2}$ F=2 → $5P_{1/2}$ F′=2 transition obtained from a scan of f_0 for a fixed value of f_r, by one-photon DFCS. (b) Raw counts for the same lineshape as in (a) by two-photon DFCS, along with a visual guide for the data.

Next, we employ DFCS to study another single-photon transition in the D_1 manifold, $5S_{1/2}$ F=2 → $5P_{1/2}$ F′=2, as shown in Fig. 6.6(a). Again, f_0 is scanned while f_r is stabilized to a convenient value. The absolute optical frequency for this transition is determined to be 377 105 206 563 (184) kHz, in agreement with a previous wavelength-based measurement [83], which gave an absolute frequency value of 377 105 206 705 (400) kHz for this transition.

For the corresponding two-photon DFCS experiment we map the $5S_{1/2}$ F=2 → $5P_{1/2}$ F′=2 → $5D_{3/2}$ F″=3 two-photon transition in the same manner employed for Fig. 6.4(b). Figure 6.6(b) shows the raw data yielded by the (f_r, f_0) pair selections, along with a visual guide for the data. The apparent linewidth is significantly broader than that associated with the 5P state.

Unlike the previous two-photon DFCS measurement reported in Fig. 6.4, the pairs of f_r and f_0 used to obtain each point in Fig. 6.6(b) lead to substantially different detunings of the other 5P states and subsequently, varying optical pumping to the F=1 ground state. Indeed, the theory model applied to the actual experiment conditions predicts significantly different ground state population transfer dynamics. As shown in Fig. 6.7, the asymptotic values of the F=2 ground-state population are not the same for symmetric detunings from the intermediate state.

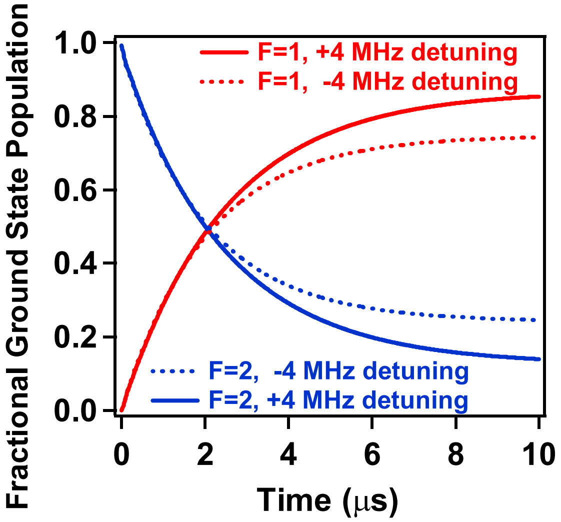

Figure 6.7: Theoretical plot of the time evolution of the ground state populations for two (symmetric) detuning values in 6.6(b), showing a significant difference in the population transfer between the ground state levels due to optical pumping caused by varying detunings from the other 5P states.

Figure 6.8(b) presents the Lorentzian lineshape resulting from the normalization of the raw data shown in Fig. 6.8(a) with respect to the theoretical value of (1 - $\rho_{F=1}$), where $\rho_{F=1}$ is the fractional ground state population in F=1, as shown in Fig. 6.7. After we implement this normalization, the optical frequency for the transition measured by the two-photon DFCS is 377 105 206 939 (179) kHz, which is within the error bars of the corresponding one-photon DFCS result.

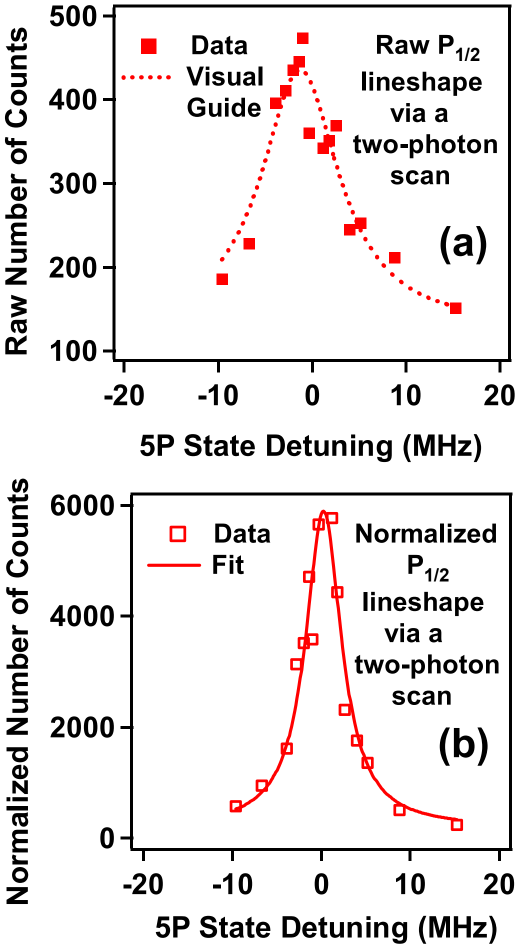

Figure 6.8: Raw data (a) and normalized lineshape (b) obtained by using results from the theory simulation in Fig. 6.8 accounting for optical pumping.

We note that for all measurements reported in this chapter, the statistical errors (one standard deviation of the mean) associated with $5P_{3/2}$ are significantly smaller than those associated with $5P_{1/2}$. This is due to the stronger transition strength and less severe optical pumping effects for $5P_{3/2}$ $F'=3$ (part of a closed transition), leading to larger signal-to-noise ratios.

Direct frequency comb measurements of one-photon transitions in atoms other than ^{87}Rb have been recently reported. In Leo Hollberg's group at NIST, they probed Cs in an atomic beam with DFCS, but using a Ti:S laser with a 1 GHz repetition rate [84]. Employing a 1-GHz fs laser has several advantages over a lower f_r laser, as stated in Chapter 7.

In conclusion, a phase-stabilized femtosecond comb has been used as an effective tool to perform direct spectroscopy of one-photon transitions in cold ^{87}Rb atoms. We have demonstrated that DFCS can be successfully applied to one-photon studies, by measuring $5S_{1/2} \rightarrow 5P_{1/2,3/2}$ transitions both directly and indirectly, via their resonant enhancement of the 5S-5D two-photon transitions. Additionally, we have shown the importance of including the dynamic population changes arising from pulse-accumulated population transfer in this indirect one-photon measurement.

Chapter 7

Summary and outlook

In this thesis, we have joined together the study of cold atoms, which are well established as an ideal sample for spectroscopy with the field of ultrafast lasers, which have recently emerged as a powerful tool for frequency metrology.

We have used a wide-bandwidth, phase-stabilized femtosecond laser as a novel and efficient tool to perform Direct Frequency Comb Spectroscopy (DFCS) of one-photon and two-photon transitions in laser-cooled ^{87}Rb atoms. To begin with, we have studied the dominant sources of systematic shifts and tried to reduce their effects as much as possible. We have then measured the absolute atomic frequency for several $5S_{1/2} \rightarrow 5D_{3/2,5/2}$ two-photon transitions in ^{87}Rb. The two-photon spectroscopy is carried out efficiently despite the low laser power, because we take advantage of intermediate 5P states that are near-resonant with a comb line. We have demonstrated that the absolute optical frequency of the previously unmeasured $5S_{1/2} \rightarrow 7S_{1/2}$ resonances can be determined unambiguously from the comb structure used in the experiment. Lastly, we have shown that DFCS can be successfully applied to one-photon processes as well, by measuring $5S_{1/2} \rightarrow 5P_{1/2,3/2}$ transitions both directly and indirectly, through their resonant enhancement of the 5S-5D two-photon transitions. Detailed dynamics of population transfer driven by a sequence of pulses were uncovered and taken into account for the indirect measurement of the 5P states. Although the current experiments involve one- and two-photon transitions, the advantages of DFCS should also apply to multi-photon excitations. In general, DFCS permits global, high-resolution spectroscopy of all the atomic transitions within the comb bandwidth.

After we successfully implemented DFCS for the study of several one- and two-photon transitions, there is still room left for improvements. Firstly, the resolution of DFCS can be enhanced by locking the femtosecond laser to a cavity, which has been shown capable to reduce the linewidth to below 100 Hz [85], rather than the current 300 kHz. Secondly, a larger signal can be obtained by using a laser with a higher repetition rate; for example, a 1-GHz laser with the same average power and spectral width could increase the signal up to a 100-fold. This is a result of the quadratic increase of the excited state population versus the accumulated number of pulses, where the higher f_r and hence the shorter pulse interval allow for more pulses to be 'added' during the atomic coherence lifetime. Additionally, the power is distributed among fewer comb lines for this $f_r \sim 1$ GHz case, and the decreased congestion of lines would reduce optical pumping effects. Achieving simultaneous one- and two-photon resonance conditions should still be possible. Using a 1-GHz laser provides more latitude in identifying the mode number of the comb component that is resonant with each optical transition. The larger mode spacing makes this identification easier, because it only requires knowledge of the optical frequencies with a precision of a few hundred MHz. One practical consequence of these results is a method to control both degrees of freedom of the femtosecond comb directly by an optical transition in cold atoms.

Another interesting application of the demonstrated pulse accumulation effect is using ultrafast pulse trains for laser cooling of atoms (e.g. hydrogen, deuterium, antihydrogen) that require coherent ultraviolet light not easily accessible by conventional laser sources [86]. Toward this goal, an extension of frequency comb metrology to the deep-ultraviolet spectral region (where cw lasers are not readily available) was recently achieved using an amplified train of phase-controlled pulses from a femtosecond laser [78]. The peak power of these pulses allowed for efficient harmonic upconversion and thus, the 4th harmonic of the femtosecond laser was used for two-photon spectroscopy in krypton. Even more recently, phase-coherent frequency combs in the vacuum-ultraviolet spectral region were demonstrated in our lab, without active amplification of the standard femtosecond laser [87]. Its output was stabilized to a completely passive optical cavity, with a gas jet at the intracavity focus, generating a phase-controlled frequency comb in the extreme ultraviolet region which preserves the original repetition frequency. This technique, in combination with DFCS, opens the door to more accurate atomic optical clocks that operate on resonances with ultrahigh, vacuum-ultraviolet or extreme-ultraviolet, frequencies. These clocks would have a very high stability, proportional to their transition frequency.

For general coherent control experiments, pulse accumulation (when enabled by long coherence times) can complement spectral amplitude and phase manipulations, leading to improved efficiency in population control with the added spectral resolution and longer experimental timescales due to maintaining phase coherence for many consecutive laser pulses. The precise and phase-coherent pulse accumulation may prove particularly useful in efficiently populating atomic Rydberg states for quantum information processing. Multiple ultrafast lasers with optical spectra independently tailored for different spectroscopic features could be phase coherently stitched together [9,88] to further extend the utility of this approach.

Bibliography

[1] D. J. Jones, S. A. Diddams, J. K. Ranka, A. Stentz, R. S. Windeler, J. L. Hall, and S. T. Cundiff, "Carrier-envelope phase control of femtosecond mode-locked lasers and direct optical frequency synthesis," Science **288**, 635–639 (2000).

[2] A. Apolonski, A. Poppe, G. Tempea, C. Spielmann, T. Udem, R. Holzwarth, T. W. Hänsch, and F. Krausz, "Controlling the Phase Evolution of Few-Cycle Light Pulses," Phys. Rev. Lett. **85**, 740–743 (2000).

[3] H. S. Margolis, G. P. Barwood, G. Huang, H. A. Klein, S. N. Lea, K. Szymaniec, and P. Gill, "Hertz-Level Measurement of the Optical Clock Frequency in a Single $^{88}\mathrm{Sr}^+$ Ion," Science **306**, 1355–1358 (2004).

[4] S. A. Diddams, T. Udem, J. C. Bergquist, E. A. Curtis, R. E. Drullinger, L. Hollberg, W. M. Itano, W. D. Lee, C. W. Oates, K. R. Vogel, and D. J. Wineland, "An optical clock based on a single trapped $^{199}\mathrm{Hg}^+$ ion," Science **293**, 825–828 (2001).

[5] J. Ye, L.-S. Ma, and J. L. Hall, "Molecular iodine clock," Phys. Rev. Lett. **87**, 270 801 (2001).

[6] J. D. Jost, J. L. Hall, and J. Ye, "Continuously tunable, precise, single frequency optical signal generator," Opt. Exp. **10**, 515–520 (2002).

[7] T. M. Fortier, D. J. Jones, and S. T. Cundiff, "Phase stabilization of an octave-spanning Ti:sapphire laser," Opt. Lett. **28**, 2198–2200 (2003).

[8] A. Baltuska, T. Fuji, and T. Kobayashi, "Controlling the Carrier-Envelope Phase of Ultrashort Light Pulses with Optical Parametric Amplifiers," Phys. Rev. Lett. **88**, 133 901 (2002).

[9] R. K. Shelton, L.-S. Ma, H. C. Kapteyn, M. M. Murnane, J. L. Hall, and J. Ye, "Phase-coherent optical pulse synthesis from separate femtosecond lasers," Science **293**, 1286–1289 (2001).

[10] A. Baltuska, T. Udem, M. Uiberacker, M. Hentschel, E. Goulielmakis, C. Gohle, R. Holzwarth, V. S. Yakovlev, A. Scrinzi, T. W. Hänsch, and F. Krausz, "Attosecond control of electronic processes by intense light fields," Nature **421**, 611–615 (2003).

[11] T. C. Weinacht, J. Ahn, and P. H. Bucksbaum, "Controlling the shape of a quantum wavefunction," Nature **397**, 233–235 (1999).

[12] T. M. Fortier, P. A. Roos, D. J. Jones, S. T. Cundiff, R. D. R. Bhat, and J. E. Sipe, "Carrier-Envelope Phase-Controlled Quantum Interference of Injected Photocurrents in Semiconductors," Phys. Rev. Lett. **92**, 147 403 (2004).

[13] E. O. Potma, D. J. Jones, J.-X. Cheng, X. S. Xie, and J. Ye, "High-sensitivity coherent anti-Stokes Raman scattering microscopy with two tightly synchronized picosecond lasers," Opt. Lett. **27**, 1168–1170 (2002).

[14] D. Meshulach and Y. Silberberg, "Coherent quantum control of two-photon transitions by a femtosecond laser pulse," Nature **396**, 239–242 (1998).

[15] T. Udem, J. Reichert, R. Holzwarth, and T. W. Hänsch, "Accurate measurement of large optical frequency differences with a mode-locked laser," Opt. Lett. **24**, 881–883 (1999).

[16] M. T. Asaki, C.-P. Huang, D. Garvey, J. Zhou, H. C. Kapteyn, and M. M. Murnane, "Generation of 11-Fs pulses from a self-mode-locked Ti-Sapphire laser," Opt. Lett. **18**, 977–979 (1993).

[17] C. Salomon, D. Hils, and J. L. Hall, "Laser stabilization at the millihertz level," J. Opt. Soc. Am. B **5**, 1576–1587 (1988).

[18] T. Udem, J. Reichert, R. Holzwarth, and T. Hänsch, "Absolute optical frequency measurement of the cesium D_1 line with a mode-locked laser," Phys. Rev. Lett. **82**, 3568–3571 (1999).

[19] S. A. Diddams, D. J. Jones, L.-S. Ma, S. T. Cundiff, and J. L. Hall, "Optical frequency measurement across a 104-THz gap with a femtosecond laser frequency comb," Opt. Lett. **25**, 186–188 (2000).

[20] S. A. Diddams, D. J. Jones, J. Ye, S. T. Cundiff, J. L. Hall, J. K. Ranka, R. S. Windeler, R. Holzwarth, T. Udem, and T. W. Hänsch, "Direct link between microwave and optical frequencies with a 300 THz femtosecond laser comb," Phys. Rev. Lett. **84**, 5102–5105 (2000).

[21] H. R. Telle, G. Steinmeyer, A. Dunlop, J. Stenger, D. Sutter, and U. Keller, "Carrier-envelope offset phase control: A novel concept for absolute optical frequency control and ultrashort pulse generation," Appl. Phys. B **69**, 327–332 (1999).

[22] J. K. Ranka, R. S. Windeler, and A. J. Stentz, "Visible continuum generation in air-silica microstructure optical fibers with anomalous dispersion at 800 nm," Opt. Lett. **25**, 25–27 (2000).

[23] S. T. Cundiff and J. Ye, "*Colloquium*: Femtosecond optical frequency combs," Rev. Mod. Phys. **75**, 325–342 (2003).

[24] T. W. Hänsch, Tunable Lasers and Applications, section "Spectroscopic Applications of Tunable Lasers", A. Mooradian, T. Jaeger and P. Stokseth, Editors (Springer-Verlag, Berlin, 1976).

[25] R. Teets, J. Eckstein, and T. W. Hänsch, "Coherent two-photon excitation by multiple light pulses," Phys. Rev. Lett. **38**, 760–764 (1977).

[26] A. I. Ferguson, J. N. Eckstein, and T. W. Hänsch, "A subpicosecond dye laser directly pumped by a mode-locked argon laser," J. Appl. Phys. **49**, 5389–5391 (1978).

[27] J. N. Eckstein, A. I. Ferguson, and T. W. Hänsch, "High-resolution two-photon spectroscopy with picosecond light pulses," Phys. Rev. Lett. **40**, 847–850 (1978).

[28] S. T. Cundiff, J. Ye, and J. L. Hall, "Optical frequency synthesis based on mode-locked lasers," Rev. Sci. Instr. **72**, 3749–3771 (2001).

[29] K. M. Evenson, J. S. Wells, F. R. Petersen, B. L. Danielson, and G. W. Day, "Accurate frequencies of molecular transitions used in laser stabilization: the 3.39-μm transition in CH_4 and the 9.33- and 10.18-μm transitions in CO_2," Appl. Phys. Lett. **22**, 192–195 (1973).

[30] K. M. Evenson, J. S. Wells, F. R. Petersen, B. L. Danielson, G. W. Day, R. L. Barger, and J. L. Hall, "Speed of Light from Direct Frequency and Wavelength Measurements of the Methane-Stabilized Laser," Phys. Rev. Lett. **29**, 1346–1349 (1972).

[31] D. A. Jennings, C. R. Pollock, F. R. Petersen, R. E. Drullinger, K. M. Evenson, J. S. Wells, J. L. Hall, and H. P. Layer, "Direct frequency measurement of the I_2 stabilized He-Ne 473-THz (633-nm) laser," Opt. Lett. **8**, 136–138 (1983).

[32] H. Schnatz, B. Lipphardt, J. Helmcke, F. Riehle, and G. Zinner, "First phase-coherent frequency measurement of visible radiation," Phys. Rev. Lett. **76**, 18–21 (1996).

[33] J. E. Bernard, A. A. Madej, L. Marmet, B. G. Whitford, K. J. Siemsen, and S. Cundy, "Cs-Based Frequency Measurement of a Single, Trapped Ion Transition in the Visible Region of the Spectrum," Phys. Rev. Lett. **82**, 3228–3231 (1999).

[34] C. Schwob, L. Jozefowski, B. de Beauvoir, L. Hilico, F. Nez, L. Julien, F. Biraben, O. Acef, and A. Clairon, "Optical frequency measurement of the 2S-12D transitions in hydrogen and deuterium: Rydberg constant and lamb shift determinations," Phys. Rev. Lett. **82**, 4960–4963 (1999).

[35] T. H. Yoon, A. Marian, J. L. Hall, and J. Ye, "Phase-coherent multilevel two-photon transitions in cold Rb atoms: Ultrahigh-resolution spectroscopy via frequency-stabilized femtosecond laser," Phys. Rev. A **63**, 011 402(R) (2000).

[36] O. S. Heavens, "Radiative transition probabilities of the lower excited states of the alkali metals," J. Opt. Soc. Am. **51**, 1058–1061 (1961).

[37] D. Felinto, C. A. C. Bosco, L. H. Acioli, and S. S. Vianna, "Coherent accumulation in two-level atoms excited by a train of ultrashort pulses," Opt. Commun. **215**, 69–73 (2003).

[38] D. Felinto, L. H. Acioli, and S. S. Vianna, “Accumulative effects in the coherence of three-level atoms excited by femtosecond-laser frequency combs,” Phys. Rev. A **70**, 043 403 (2004).

[39] N. V. Vitanov and P. L. Knight, “Coherent excitation of a two-state system by a train of short pulses,” Phys. Rev. A **52**, 2245–2261 (1995).

[40] M. M. Salour, “Quantum interference effects in two-photon spectroscopy,” Rev. Mod. Phys. **50**, 667–681 (1978).

[41] M. Stowe, “Private communication,” .

[42] Femtosecond Optical Frequency Comb Technology: Principle, Operation and Application, J. Ye and S. T. Cundiff, Editors (Springer, New York, 2005).

[43] T. M. Fortier, “Phase Stabilized Modelocked Lasers: from optical frequency metrology to waveform synthesis of ultrashort pulses,” Ph. D Thesis, JILA and University of Colorado (2004).

[44] J. Reichert, R. Holzwarth, T. Udem, and T. Hänsch, “Measuring the frequency of light with mode-locked lasers,” Opt. Commun. **172**, 59–68 (1999).

[45] S. Cundiff, L. Hollberg, and J. Hall, “Creating and Applying Optical Frequency Synthesizers using Mode-Locked Lasers,” FY2000 Competence Proposal (March 1999).

[46] K. W. Holman, R. J. Jones, A. Marian, S. T. Cundiff, and J. Ye, “Intensity-related dynamics of femtosecond frequency combs,” Opt. Lett. **28**, 851–853 (2003).

[47] K. W. Holman, R. J. Jones, A. Marian, S. T. Cundiff, and J. Ye, “Detailed Studies and Control of Intensity-Related Dynamics of Femtosecond Frequency Combs from Mode-Locked Ti:Sapphire Lasers,” IEEE J. Sel. Top. Quantum Electron. **9**, 1018–1024 (2003).

[48] H. J. Metcalf and P. van der Straten, Laser Cooling and Trapping (Springer-Verlag, New York, 1999).

[49] J. R. Ensher, “The First Experiments with Bose-Einstein Condensation of ^{87}Rb ,” Ph. D. Thesis, JILA and University of Colorado (1998).

[50] B. DeMarco, “Quantum Behavior of an Atomic Fermi Gas,” Ph. D. Thesis, JILA and University of Colorado (2001).

[51] H. J. Lewandowski, “Coherences and correlations in an ultracold Bose gas,” Ph. D. Thesis, JILA and University of Colorado (2002).

[52] C. Monroe, W. Swann, H. Robinson, and C. Wieman, “Very cold trapped atoms in a vapor cell,” Phys. Rev. Lett. **65**, 1571–1574 (1990).

[53] K. B. MacAdam, A. Steinbach, and C. Wieman, “A narrow-band tunable diode laser system with grating feedback, and a saturated absorption spectrometer for Cs and Rb,” Am. J. Phys. **60**, 1098–1111 (1992).

[54] C. E. Wieman and L. Hollberg, “Using diode lasers for atomic physics,” Rev. Sci. Instr. **62**, 1–20 (1991).

[55] L. Ricci, M. Weidemüller, T. Esslinger, A. Hemmerich, C. Zimmermann, V. Vuletic, W. König, and T. Hänsch, “A compact grating-stabilized diode laser system for atomic physics,” Opt. Commun. **117**, 541–549 (1995).

[56] G. C. Bjorklund, “Frequency-modulation spectroscopy: a new method for measuring weak absorptions and dispersions,” Opt. Lett. **5**, 15–17 (1980).

[57] J. L. Hall, L. Hollberg, T. Baer, and H. G. Robinson, “Optical heterodyne saturation spectroscopy,” Appl. Phys. Lett. **39**, 680–682 (1981).

[58] E. L. Raab, M. Prentiss, A. Cable, S. Chu, and D. E. Pritchard, “Trapping of neutral Sodium atoms with radiation pressure,” Phys. Rev. Lett. **59**, 2631–2634 (1987).

[59] P. D. Lett, R. N. Watts, C. I. Westbrook, W. D. Philips, P. L. Gould, and H. J. Metcalf, “Observation of atoms laser cooled below the Doppler limit,” Phys. Rev. Lett. **61**, 169–172 (1988).

[60] A. Marian, M. C. Stowe, J. R. Lawall, D. Felinto, and J. Ye, “United time-frequency spectroscopy for dynamics and global structure,” Science **306**, 2063–2068 (2004).

[61] B. Cagnac, G. Grynberg, and F. Biraben, “Spectroscopie d’Absorption Multiphotonique sans Effet Doppler,” Journal de Physique **34**, 845–858 (1973).

[62] D. Pritchard, J. Apt, and T. W. Ducas, “Fine Structure of Na $4d^2D$ Using High-Resolution Two-Photon Spectroscopy,” Phys. Rev. Lett. **32**, 641–642 (1974).

[63] F. Biraben, B. Cagnac, and G. Grynberg, “Experimental Evidence of Two-Photon Transition without Doppler Broadening,” Phys. Rev. Lett. **32**, 643–645 (1974).

[64] M. D. Levenson and N. Bloembergen, “Observation of Two-Photon Absorption without Doppler Broadening on the $3S - 5S$ Transition in Sodium Vapor,” Phys. Rev. Lett. **32**, 645–648 (1974).

[65] J. E. Bjorkholm and P. F. Liao, “Resonant enhancement of two-photon absorption in Sodium vapor,” Phys. Rev. Lett. **33**, 128–131 (1974).

[66] O. Poulsen and N. I. Winstrup, “Resonant two-photon spectroscopy in a fast accelerated atomic beam,” Phys. Rev. Lett. **47**, 1522–1525 (1981).

[67] M. M. Salour and C. Cohen-Tannoudji, “Observation of Ramsey’s Interference Fringes in the Profile of Doppler-Free Two-Photon Resonances,” Phys. Rev. Lett. **38**, 757–760 (1977).

[68] Y. V. Baklanov, V. P. Chebotayev, and B. Y. Dubetsky, “The resonance of two-photon absorption in separated optical fields,” Appl. Phys. **11**, 201–202 (1976).

[69] J. C. Bergquist, S. A. Lee, and J. L. Hall, “Saturated absorption with spatially separated laser fields: Observation of optical “Ramsey” fringes,” Phys. Rev. Lett. **38**, 159–162 (1977).

[70] M. J. Snadden, A. S. Bell, E. Riis, and A. I. Ferguson, “Two-photon spectroscopy of laser-cooled Rb using a mode-locked laser,” Opt. Commun. **125**, 70–76 (1996).

[71] N. Dudovich, B. Dayan, S. M. Gallagher Faeder, and Y. Silberberg, “Transform-Limited Pulses Are Not Optimal for Resonant Multiphoton Transitions,” Phys. Rev. Lett. **86**, 47–50 (2001).

[72] E. Gomez, S. Aubin, L. A. Orozco, and G. D. Sprouse, “Lifetime and hyperfine splitting measurements on the $7s$ and $6p$ levels in rubidium,” J. Opt. Soc. Am. B **21**, 2058–2067 (2004).

[73] J. Ye, J.-L. Peng, R. J. Jones, K. W. Holman, J. L. Hall, D. J. Jones, S. A. Diddams, J. Kitching, S. Bize, J. C. Bergquist, L. W. Hollberg, L. Robertsson, and L.-S. Ma, “Delivery of high-stability optical and microwave frequency standards over an optical fiber network,” J. Opt. Soc. Am. B **20**, 1459–1467 (2003).

[74] P. F. Liao and J. E. Bjorkholm, “Direct observation of atomic energy level shifts in two-photon absorption,” Phys. Rev. Lett. **34**, 1–4 (1975).

[75] F. Nez, F. Biraben, R. Felder, and Y. Millerioux, “Optical frequency determination of the hyperfine components of the $5S_{1/2}-$ $5D_{3/2}$ two-photon transitions in rubidium,” Opt. Commun. **102**, 432–438 (1993).

[76] A. Marian, M. C. Stowe, D. Felinto, and J. Ye, “Direct frequency comb measurements of absolute optical frequencies and population transfer dynamics,” Phys. Rev. Lett. **95**, in press (2005).

[77] R. Holzwarth, A. Y. Nevsky, M. Zimmermann, T. Udem, T. W. Hänsch, J. von Zanthier, H. Walther, J. C. Knight, W. J. Wadsworth, P. S. J. Russell, M. N. Skvortsov, and S. N. Bagayev, “Absolute frequency measurement of iodine lines with a femtosecond optical synthesizer,” Appl. Phys. B **73**, 269–271 (2001).

[78] S. Witte, R. T. Zinkstok, W. Ubachs, W. Hogervorst, and K. S. E. Eikema, “Deep-Ultraviolet Quantum Interference Metrology with Ultrashort Laser Pulses,” Science **307**, 400–403 (2005).

[79] M.-S. Ko and Y.-W. Liu, “Observation of rubidium $5S_{1/2} \rightarrow 7S_{1/2}$ two-photon transitions with a diode laser,” Opt. Lett. **29**, 1799–1801 (2004).

[80] H. T. Duong, S. Liberman, J. Pinard, and J.-L. Vialle, “Measurement of the Hyperfine Structure of the $5\ ^2S_{1/2}$ State of ^{23}Na by Two-Step Excitation Using Two cw Dye Lasers,” Phys. Rev. Lett. **33**, 339–341 (1974).

[81] H.-C. Chui, M.-S. Ko, Y.-W. Liu, J.-T. Shy, J.-L. Peng, and H. Ahn, “Absolute frequency measurement of rubidium $5S7S$ two-photon transitions with a femtosecond laser comb,” Opt. Lett. **30**, 842–844 (2005).

[82] J. Ye, S. Swartz, P. Jungner, and J. L. Hall, “Hyperfine structure and absolute frequency of the ^{87}Rb $5P_{3/2}$ state,” Opt. Lett. **21**, 1280–1282 (1996).

[83] G. P. Barwood, P. Gill, and W. R. C. Rowley, “Frequency Measurements on Optically Narrowed Rb-Stabilised Laser Diodes at 780 nm and 795 nm,” Appl. Phys. B **53**, 142–147 (1991).

[84] V. Gerginov, C. E. Tanner, S. A. Diddams, A. Bartels, and L. Hollberg, “High-resolution spectroscopy with a femtosecond laser frequency comb,” Opt. Lett. **30**, in press (2005).

[85] R. J. Jones, I. Thomann, and J. Ye, “Precision stabilization of femtosecond lasers to high-finesse optical cavities,” Phys. Rev. A **69**, 051 803(R) (2004).

[86] D. Kielpinski, “Laser cooling and trapping with ultrafast pulses,” http://arxiv.org/abs/quant-ph/0306099 (2003).

[87] R. J. Jones, K. D. Moll, M. J. Thorpe, and J. Ye, “Phase-Coherent Frequency Combs in the Vacuum Ultraviolet via High-Harmonic Generation inside a Femtosecond Enhancement Cavity,” Phys. Rev. Lett. **94**, 193 201 (2005).

[88] K. W. Holman, D. J. Jones, J. Ye, and E. P. Ippen, “Orthogonal control of the frequency comb dynamics of a mode-locked laser diode,” Opt. Lett. **28**, 2405–2407 (2003).